Planetology
Future Explorations

Edited by Bryan Palaszewski

Planetology - Future Explorations

Edited by Bryan Palaszewski

IntechOpen

Supporting open minds since 2005

Notice
Statements and opinions expressed in the chapters are these of the individual contributors and not necessarily those of the editors or publisher. No responsibility is accepted for the accuracy of information contained in the published chapters. The publisher assumes no responsibility for any damage or injury to persons or property arising out of the use of any materials, instructions, methods or ideas contained in the book.

We are IntechOpen,
the world's leading publisher of
Open Access books
Built by scientists, for scientists

4,600+
Open access books available

120,000+
International authors and editors

135M+
Downloads

151
Countries delivered to

Our authors are among the
Top 1%
most cited scientists

12.2%
Contributors from top 500 universities

CLARIVATE ANALYTICS
BOOK CITATION INDEX
INDEXED

WEB OF SCIENCE™

Selection of our books indexed in the Book Citation Index
in Web of Science™ Core Collection (BKCI)

Interested in publishing with us?
Contact book.department@intechopen.com

Numbers displayed above are based on latest data collected.
For more information visit www.intechopen.com

Meet the editor

Bryan Palaszewski has worked at the NASA Glenn Research Center at Lewis Field since 1989 and is currently directing research on high performance propellants and atmospheric entry.
He is currently conducting analyses for the NASA Office of the Chief Technologist investigating nanometer-scale propellant additives for metallized gelled fuels for many space mission applications. Recently, he led work related to human Mars entry, descent, and landing (EDL) where supersonic retro-propulsion (rocket deceleration) is planned for the final descent to the planet's surface. He is also investigating the mining of outer planet atmospheres and the challenges and benefits for future ambitious space missions. For six years, he led many studies of advanced space systems for orbital and interplanetary travel at the Jet Propulsion Laboratory, Pasadena, CA. He was also the lead propulsion subsystem engineer on the Ocean Topography Experiment (TOPEX) for three years, as well as being involved in other flight projects such as the Galileo Mission to Jupiter and the Cassini Mission to Saturn.
He holds a Master of Science Degree in Mechanical Engineering from the Massachusetts Institute of Technology and a Bachelors Degree in Mechanical Engineering from the City College of New York. He has received the AIAA Sustained Service Award in 2004, and was chair of the AIAA Nuclear and Future Flight Propulsion Technical committee for three years beginning in 1997 and was also chair of this committee for the second time from 2008 to 2011.

Contents

Preface

This book is part of a long journey of discovery and exploration. As a propulsion engineer at the Jet Propulsion Laboratory and now NASA Glenn Research Center, I have tried to understand the many ways of transporting scientific instruments, cargo, and people around the solar system. The issues of system engineering and the gathering together of the many components of a space vehicle is always a daunting undertaking. Teams of people working in close coordination make these space vehicles a reality and their missions a success. We have explored many corners of the Universe, but our journey seems to be only just beginning. Engineers and scientists have dreamed of humans living and thriving throughout the solar system. This book is a celebration of those dreams.

The book is divided in three sections: Introduction, Planetary Explorations, and Computational Musings. The Introduction consists of a chapter introducing the readers to the book's main subject. The following section, Planetary Explorations, includes Technologies for Deviation of Asteroids and Cleaning of Earth Orbit by Space Debris; Solar System Exploration Augmented by In-Situ Resource Utilization: Processes, Vehicles, and Moon Bases for Saturn Exploration; Space Access for Future Interplanetary Missions; and Impact Models of Gravitational and Electrostatic Forces, Potential Energies, Atomic Clocks, Gravitational Anomalies, and Redshift. Computing Assisted Geometric Search for Human Design and Origins is included in the last section of this book.

The chapters are inspired by the wide range of critical issues facing the space flight and astronomical communities. Asteroids remain a potential in-space resource and a threat to humanity. The Saturn In-Situ Resource Utilization chapter was inspired in part by the writings of Krafft Ehricke, a space visionary who led numerous studies of human exploration of the entire solar system. Gravity waves have been detected on a more regular basis, perhaps leading to a better understanding of the massive forces unleashed by the coalescence of black holes. An inkling of panspermia is suggested in the last paper, where the search for the evidence of simple life forms is discussed.

Bryan Palaszewski
NASA John H. Glenn Research Center,
Cleveland, Ohio, USA

Section 1

Introduction

Introductory Chapter: Planetology

Bryan Palaszewski

1. Introduction

Over the last 80 years, dreamers, engineers, mission planners, and scientists have sought, defined, and created many methods of exploring the solar system [1]. Robotic missions to nearly every type of solar system object have been conducted. The data from these missions has opened new vistas on the riches of the planets and the asteroids. Water and other materials that can help humans survive in space are near ubiquitous. Human lunar missions have returned hundreds of kilograms of rocky and dusty samples; that regolith has given us hope that humanity will one day colonize the Moon, Mars, and the moons of other planets.

Many space agencies around the world have shared their information and created collaborations for the betterment of all. The agencies of NASA, ESA, and others have begun to discuss and plan a Moon Village; such a village will allow the development of lunar resources and create great wealth for all humanity. India and the United States has created instruments that have verified the presence of lunar polar water ice [2]. China has demonstrated effective communications for lunar far-side rover operations. Thus, many nations are creating new lunar data and capabilities. Pooling all of this knowledge will lead to new breakthrough in understanding the lunar environment.

Interplanetary dreams are part of humanity's future. Extended exploration missions and the initial colonization of the Moon will lead to a better understanding of the limits of the human body. While our minds can create new brilliant ideas and concepts for supporting life, the human body is frail and must be protected from the ravages of microgravity, radiation, and loneliness. Exposure to microgravity weakens the cardiovascular system and human muscles, so artificial gravity may be required for long-duration space flights [3]. Radiation can destroy the human DNA; protective methods of living underground on the Moon and Mars give hope to solving such issues. Once these impediments are better understood, humanity can begin to flourish throughout the planets.

Asteroids, while small in comparison to moons, offer many natural resources. Metals, water, and frozen gases may be mined there. The asteroids occupy many spaces throughout the solar system, so they may be caches for resources almost anywhere we travel. While rich in minerals, near-Earth asteroids also pose a threat to life on Earth. Asteroid defense studies and experiments have paved the way to manipulate these rocky and metallic objects, deflecting them from any potential Earth impacts.

In the outer planets, Jupiter, Saturn, Uranus, and Neptune can provide gases and other materials from which starship construction can begin. Nuclear fuels, such as deuterium and helium 3, can be wrested from the hydrogen and helium atmospheres of these giant planets [4]. Fission and fusion propulsion systems can be fueled from these atmospheric constituents. Past design studies have discussed robotic interstellar missions that begin with such atmospheric mining. It's important to point out that for a large interstellar mission to Alpha Centauri,

our nearest stellar neighbor, traveling at one-tenth the speed of light, the total energy required to accomplish that mission will be between 1 and 100 times the total world's energy output. This energy challenge is very readily met by using the resources of the outer planets.

The energy for Earth launch will be a great focus of attention. New concepts in reusability are reducing launch costs. Large-scale projects can be accomplished with hundreds of small components lofted by reusable rockets. Such an assembly process may be beneficial for robotic missions. During a lunar planning study, assembling a large lunar cargo mission of 250 MT would take more than 25 launches of 10 MT payloads to orbit. If the payload flights were once a month, it would require over 2 years to assemble the complete vehicle in low Earth orbit. Given this lengthy assembly process, there are many opportunities for propellant boil-off, missed or failed rendezvous and docking attempts, and other delaying issues. Human space flights may require a faster method. Alternatively, extremely large rocket boosters can lift fully assembled multi-hundred ton interplanetary vehicles into orbit in one piece. The benefits of both ideas will likely be exploited to the fullest.

Humanity must also acknowledge that sustainability is crucial to survival. New techniques in regolith-based construction are under development now. Solar energy focused on sintered regolith can allow building block assembly of small and large structures. Using biomimicry and bio-inspired processes will come to the fore. Humanity's waste products will be reformed into building materials. Many teams around the world are inspired by space flight and are addressing the sustainability issue. Conversion methods for human-made waste products have been envisioned as creating radiation shields, purified water supplies, and rocket propellants. Numerous other applications and product will no doubt be formulated.

Krafft Ehricke, a noted space flight engineer and visionary, maintained that humanity has a destiny in the heavens. Ehricke was the first project manager for the world's first high energy oxygen/hydrogen rocket stage, the Centaur. While leading that project, he also directed a team of engineers and scientists to develop human interplanetary mission concepts. These concepts ranged from human space travel to all of the planets from Mercury to Saturn [5]. While these missions have not yet come to fruition, these ideas have inspired new research in human and robotic space travel. Over many decades, numerous teams have furthered his team's research in interplanetary travel. Robots blaze the trails to planets, reveal incredible secrets, and give us pause to reflect on the wonders of the far reaches of the solar system.

While we strive to understand our solar system, we also have the influences of the rest of the galaxy to explore. Gravity waves, galactic cosmic rays, and the Sun's interactions with the rest of the Milky Way will teach us how the rest of the universe works. Humanity has a boundless imagination and we hope of the fullest understanding of all we see and touch. The measurement of gravity waves from the collision of two black holes many times the mass of our Sun bodes well for new directions in science and technology. Perhaps among the 200 billion other stars in our galaxy, other intelligent life exists, awaiting our emergence from the solar heliopause bubble.

Exploring the solar system is an endless process. There are so many facets to examine, and new theories and models of the natural solar system processes are created every year. Thousands of new research project personnel examine the Apollo lunar samples, the data from our interplanetary robotic emissaries, model the future of humans in space, and create new theories about life in the universe. Perhaps, the hopeful human lunar missions will once again ignite the imagination and allow the first steps to Mars and then to the stars.

Author details

Bryan Palaszewski
Leader of Advanced Fuels, NASA Glenn Research Center, Cleveland, Ohio, USA

*Address all correspondence to: bryan.a.palaszewski@nasa.gov

IntechOpen

References

[1] Portree DSF. Humans to mars: Fifty years of mission planning, 1950-2000. NASA/SP-2001-4521. 2001

[2] Haney M, Inocente D, Katz N, Petrov GI, et al. Moon village reference masterplan and habitat design. In: International Conference on Environmental Systems. Skidmore: Owings & Merrill LLP; 2019

[3] Huff JL, Patel ZS, Simonsen LC. Mitigation strategies for space radiation health risks. JSC-E-DAA-TN72128. 2019

[4] Palaszewski B. Atmospheric mining in the outer solar system, moon base propulsion: Outer planet resource processing, moon base propulsion, and vehicle design issues. AIAA 2019-4031. 2019

[5] Palaszewski B. Solar system exploration augmented by in-situ resource utilization: Historical perspectives and future possibilities. AIAA 2014-0498. 2014

Section 2

Planetary Exploration

Technologies for Deviation of Asteroids and Cleaning of Earth Orbit by Space Debris

Constantin Sandu, Cristian-Teodor Olariu
and Radu-Constantin Sandu

Abstract

The present chapter presents the advanced design and technology of special equipment (SECSL) which uses concentrated solar light for deviation of asteroids and cleaning the space of debris. The elliptical orbit of any cosmic body as presented in Einstein's general theory of relativity is rotating around the ellipse center. The trajectory of a cosmic body is permanently affected by the gravity of other moving cosmic bodies. In the case of asteroids (relatively small masses), orbit changes can lead to a collision with the Earth. At this very moment, our civilization has no efficient and reliable mean to destroy or divert a cosmic body heading toward the Earth. This new idea represents a "light canon" which uses concentrated solar light for deviation or vaporization of dangerous asteroids. The equipment is composed out of two parabolic mirrors (one large and one small) with the same focal point and coincident axes. The mirrors reflect the sunlight between them hence the term "concentrated solar light." Next, a similar idea to the SECSL equipment is presented but applied to space debris caused mostly by humans and a new way of disintegrating satellites, spent rocket boosters, thrust chambers, etc. in the Earth's atmosphere during reentry.

Keywords: parabolic mirror, concentrated solar light, equipment, asteroid, satellite, disintegration, cosmic body, deorbit, reentry, space debris, atmosphere

1. Introduction

Today, there is no reliable nor efficient system which can destroy or deflect asteroids or comets on a collision trajectory with the Earth. At this very moment, we cannot comprehend what could happen if an asteroid impacts the Earth. On April 13, 2029, we might experience just that because asteroid Apophis will pass below the orbit of low earth orbit (LEO) satellites and its exact trajectory cannot be predicted.

Albert Einstein, in his general theory of relativity, says that the elliptical orbit of any cosmic body is rotating around the ellipse center (i.e., the perihelion of the orbit is moving continuously). The elliptical orbit or trajectory of any cosmic body (i.e., asteroids, comets, etc.) can be permanently altered by the gravity of other asteroids and planets. Due to this reason, asteroids can be involved in collisions that cause sudden trajectory changes. The trajectory change could one day be toward the

Earth, because asteroids have relatively small masses; thus a change in its trajectory is significant.

According to estimates, there are over 150 million asteroids in our solar system, most of them are grouped in what is called an asteroid belt (see **Figure 1**) and have trajectories passing close to the Earth (see **Figure 2**). NASA's revised estimate of the number of near-Earth asteroids provided by Wide-field Infrared Survey Explorer (WISE) during the NEOWISE project had the number of larger than 100-m objects which are considered medium- to large-sized asteroids at 500. Near-Earth asteroids smaller than 100 m were not studied, and at a later time, near-Earth comets will be analyzed.
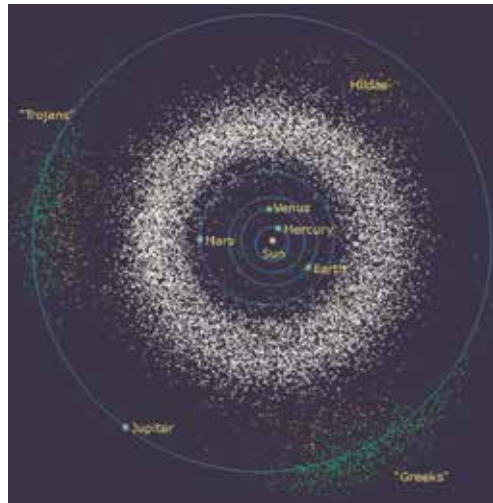
Figure 1.
Asteroid belt.
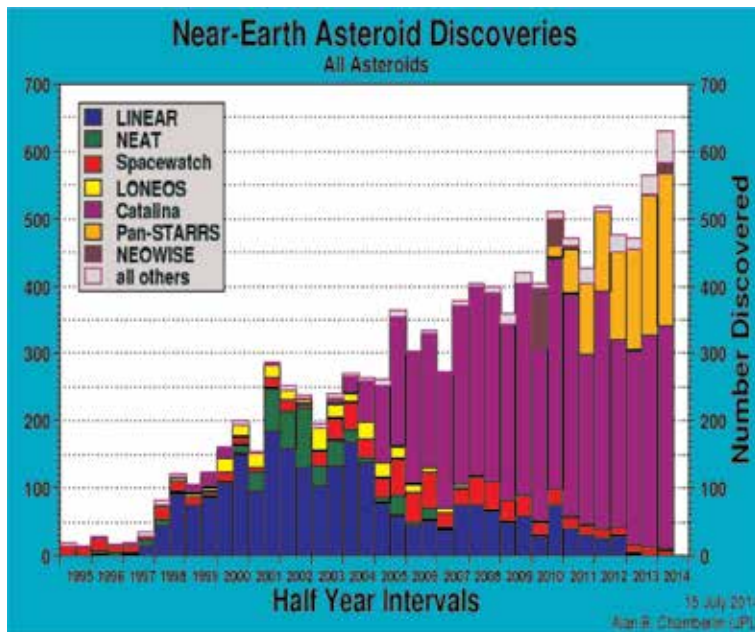
Figure 2.
Near-Earth discovered steroids.

For asteroids larger than 1000 m, the revised number is down to 981 from a prior estimate of about 1000. Out of the 981 large-sized asteroids, NASA managed to estimate with great precision the size of each individual.

The number of asteroids that disintegrate into the atmosphere is surprisingly very high (see **Figure 3**) which demonstrates that the problem with asteroid impact is very alarming.

Two proposed solutions for the Earth's protection against asteroids are synthesized in [1]. The first protection method is presented in **Figure 4**, and it relies on capturing small celestial objects. The second method is presented in **Figure 5**, and it relies on a satellite carrying a nuclear-powered laser which deflects asteroids through local vaporization (laser ablation).

Other solutions propose asteroid gravity tractor, kinetic impact, nuclear explosive devices, etc. It is quite clear that these solutions are not completely satisfactory.
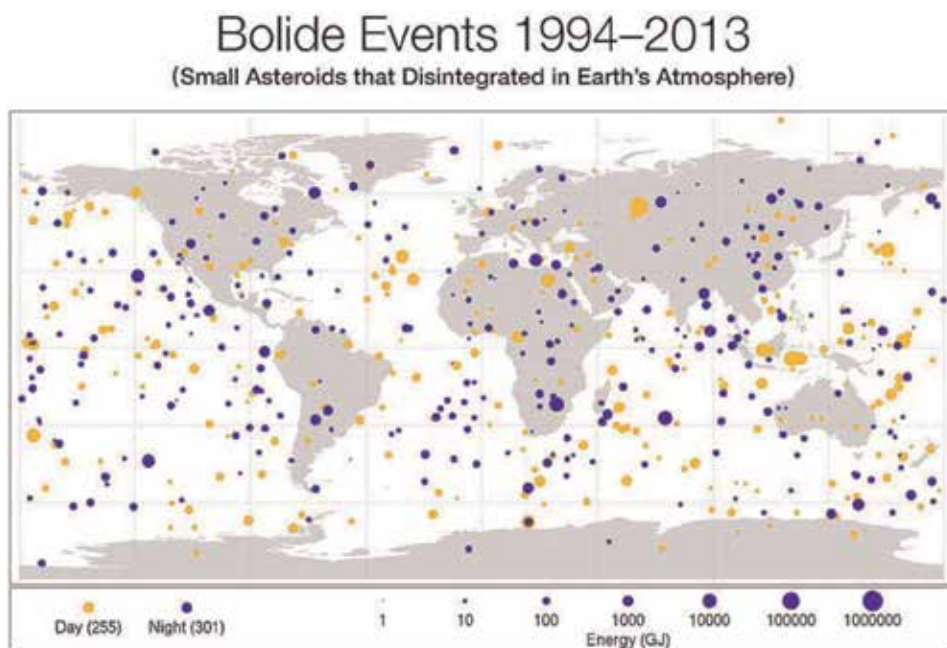
Figure 3.
Number of asteroids that have been disintegrated in the Earth's atmosphere during 1994–2013.
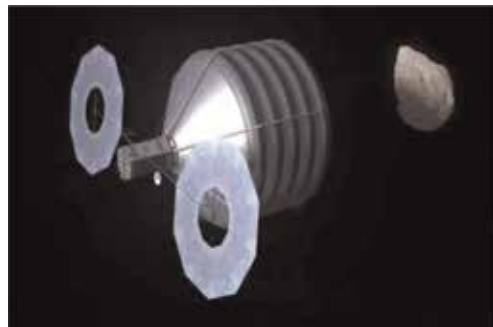
Figure 4.
Asteroid capture system.

Figure 5.
Asteroid deflection using laser rays.

Asteroids can be very large objects, most of them are rotating conglomerates formed through accumulation of debris after colliding with other asteroids.

Measurements of rotation rates of large asteroids located in the asteroids belt yielded no upper limit. No asteroid with a diameter larger than 100 m has a rotation period smaller than 2.2 h. However, a solid object formed through accumulation of debris after collisions between asteroids should be able to rotate much faster. Due to these issues, the Earth's protection against asteroids has no satisfactory solution just yet.

Also in the near-Earth region, there are not only asteroids and comets, there's also man-made debris as a result of space exploration missions manned and unmanned. Man-made space debris already represents a great threat to the safety of space exploration and exploitation. Most of the space debris is concentrated in the near-Earth space region in the low earth orbit (LEO) and geostationary earth orbit (GEO) (see **Figures 6** and 7). Space debris are composed of nonfunctional rocket boosters, spent rocket upper stages, paint flakes, chunks of slag from solid rocket motors, old science experiment equipment, nonfunctional satellites, various fragments which are the result of collisions, satellite components destroyed by missiles, and materials detached from the International Space Station (ISS) [4].

Just like asteroids, space debris can be classified by their dimensions:

- Category I: size <1 cm—can cause significant damage to vulnerable parts of the satellite.

- Category II: size 1 to 10 cm—can cause serious damage to or destroy a satellite; there is no effective shielding against this category of debris.

- Category III: size >10 cm—can destroy a satellite by collision; it can be tracked, and the satellite can perform evasive maneuvers to avoid collision.

Figure 6.
Space debris in the LEO region [2].
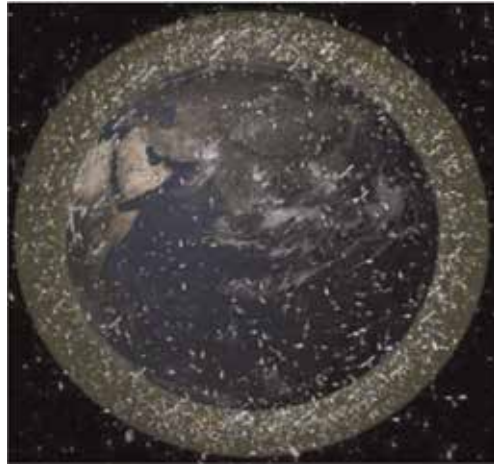
Figure 7.
Space debris in the GEO region [3].

Today, the growth of space activities is exponential, but this growth has generated an important problem: the need for rapid disintegration of space debris after reentry in the Earth's atmosphere. Space debris as stated earlier represents nonfunctional man-made objects or fragments of such objects. Only 6% of catalogued objects are functional, the rest of them are space debris [3]. At the end of their operational life, satellites reenter the Earth's atmosphere being disintegrated through burning initiated by the friction with air. This is happening for the final rocket stages which become space debris after the propellant has been depleted. In many cases the space debris fallen on the ground had large dimensions (helium tanks, thrust chambers, propellant tank, pressure sphere) [5].

The lifetime of a man-made object is very long; for example, satellites of the Satellite Pour l'Observation de la Terre or Satellite for Observation of Earth (SPOT) family placed on a Sun-synchronous orbit can orbit for about 200 years at 822 km altitude representing a high risk for other satellites [6]. Regulations were issued for direct deorbiting of satellites after finishing their operational life, but these regulations do not solve the need for rapid burning of satellites in the atmosphere; thus big chunks of unburned metal could fall on the ground [7].

The European Space Agency (ESA) came with a proposal to solve this problem under the name of "Design for Demise," according to which space equipment design must take into account the on-ground safety requirements [8].

The "Design for Demise" proposes that separation of satellite into components due to the centrifugal forces should be done during the reentry procedure. Although this is a good idea, it still does not respond to the need of rapid burning in the atmosphere, and again big chunks of unburned metal could fall on the ground.

For each of the upper-mentioned problems, there is a potential solution in the form of a system or a new way of designing space equipment. In the next chapter, each system will be presented in detail.

2. Special equipment which uses concentrated solar light for earth protection against asteroids: "light gun"

The special equipment which uses concentrated solar light for Earth protection against asteroids proposed in this paper could be placed on a solar orbit close to the Earth or on the Earth's orbit. This special equipment represents a system which

includes one large and one small parabolic mirrors both highly reflective and with the same focal point. The reflectivity of a mirror is given by reflective foils (or plates) which are stretched on a lightweight parabolic support for the mirror. The light rays coming from the Sun are focalized by the large parabolic mirror onto the focal point; afterward they are reflected by the small parabolic mirror as a group of parallel rays which pass through a central hole located in the center of the large parabolic mirror. A mirror tube attached to the large parabolic mirror by means of an articulation permits the orientation of the concentrated light beam as required (see **Figure 8**).

The role and functions of the main components:

1. Large parabolic mirror. Role: capture and focus sunlight onto the common focal point.

2. Small parabolic mirror. Role: receives the light rays coming from the large parabolic mirror and reflects them forming a beam of concentrated parallel rays of light.

3. Mobile mirror tube guide. Role: directs the light beam as required.

4. Spherical articulation. Role: permits the rotation of the light guide around one point.

5. Resistance structure. Role: keeps in position the foil forming the large parabolic structure. The foil is stretched on this structure.

6. Connection structure. Role: aligns the mirrors so their axes are always parallel and their focal point is common.

7. Positioning engines. Role: keep the SECSL in the correct position and maintain stability.
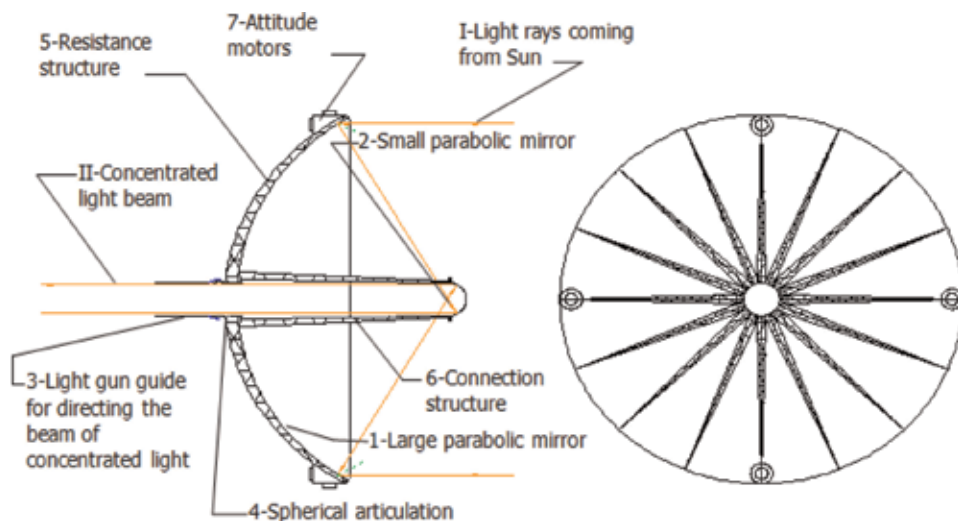
Figure 8.
Main design features of SECSL.

The SECSL is table in space; according to the law of momentum conservation, the sum of all light impulses is zero. However, when the light beam is directed toward the target, this balance is changed, and compensation forces must be applied to keep the system in position (i.e., with the concave side of the large parabolic mirror oriented toward the Sun).

2.1 Estimating the power of a SECSL system

Solar power is the key future for our civilization to expand in space. The main component of this power is electromagnetic radiation. The spectrum of solar radiation is the spectrum of a black body having a temperature of 5800 K [9]. The electromagnetic radiation is emitted in a broadband of frequencies. Electromagnetic energy is initially emitted in the range of gamma rays, as a result of nuclear fusion reactions. Gamma rays during their travel from the Sun's core to the surface are converted into low-energy photons. Thus the Sun does not emit gamma rays; it emits only X-rays, ultraviolet light, visible light, infrared light, and radio waves. The spectrum of nearly all solar electromagnetic radiation striking the Earth's atmosphere ranges from 100 nm to 1 mm.

In **Figure 9** the power emitted by the Sun under the form of X rays and ultraviolet is low. Most of the power is emitted in the range of visible light. Infrared and radio frequencies have less power. Assuming the SECSL is placed near the Earth, the irradiance can be assumed to be $E_e = 1360$ W/m^2.

Both mirrors are made from gold-plated Mylar foil with remarkable reflectivity coefficient [10]. **Figure 10** shows that for most frequencies, gold has a reflection coefficient of $R_g = 0.98$ compared to aluminium or silver. In the case of the SECSL, the best foil should be made of gold-plated fine and thin graphite fabric due to gold's remarkable reflection coefficient and graphite's high heat transfer coefficient and high emissivity coefficient.

If the large parabolic mirror is oriented with the reflective (concave) face towards the Sun, the amount of energy captured is maximized.

For example, if the large mirror has a radius of r = 10 m and assuming the solar irradiance is $E_e = 1360$ W/m^2, the total collected power is
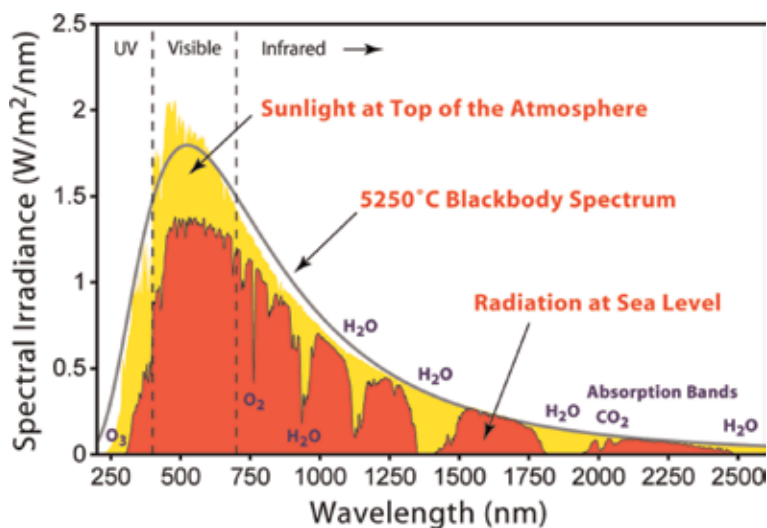
Figure 9.
The spectrum of the Sun.
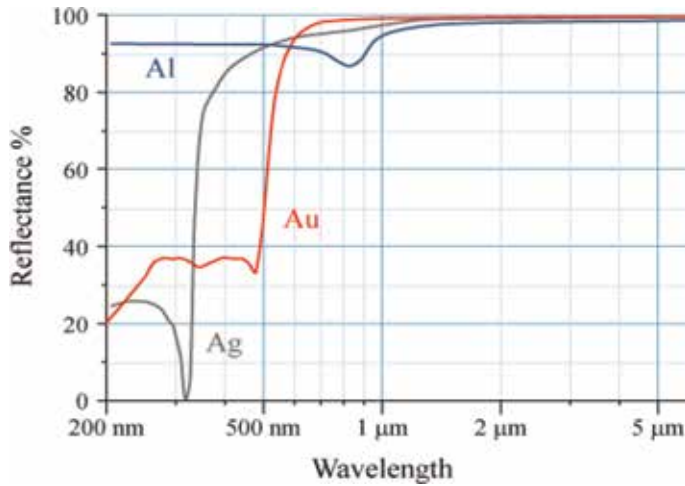
Figure 10.
Reflection coefficient of metals.

$$P = E_e \cdot \pi \cdot r^2 = 1360 \cdot \pi \cdot 10^2 = 427.256 \text{ kW} \qquad (1)$$

The total collected power is significant. However, when this radius increases, the power collected from the Sun becomes very high. **Table 1** shows the correlation between the SECSL mirror diameter and the amount of collected power. As shown in the table, when the radius of the large parabolic mirror r = 50 m, the collected power is P = 10681.4 kW. Such a mirror is relatively easy to be built in space due to the absence of gravitational forces.

For a simple sample calculation, assume that a SECSL having a radius of large parabolic mirror, r = 50 m, is focused on an iron asteroid for 10 s. Consider iron properties listed in the literature [11]:

Crt. no.	Radius of large parabolic mirror, r (m)	Collected solar power, P (kW)	Crt. no.	Radius of large parabolic mirror, r (km)	Collected solar power, P (terawatt)
1	5	106.8	13	1	0.004
2	10	427.3	14	2	0.017
3	15	961.3	15	3	0.038
4	20	1709.0	16	4	0.068
5	30	3845.3	17	6	0.154
6	40	6836.1	18	8	0.273
7	50	10681.4	19	10	0.427
8	60	15381.2	20	12	0.615
9	70	20935.6	21	14	0.837
10	80	27344.4	22	16	1.093
11	90	34607.8	23	18	1.383
12	100	42725.7	24	20	1.708

Table 1.
Collected solar power for different large parabolic mirror radii.

- Melting temperature: t_m = 1538°C, T_m = 1811 K

- Boiling temperature: t_b = 2862°C, T_b = 3135 K

- Heat capacity: c = 0.45 kJ/kgK (considered the same for solid and liquid iron)

- Heat of fusion: c_f = 247.3 kJ/kg

- Heat of vaporization: c_v = 6088.3 kJ/kg

The heat quantity needed in order to vaporize 1 kg of iron can be calculated:

$$E_1 = 1 \cdot c \cdot (T_b - T_c) + c_f \cdot 1 + c_v \cdot 1 = 0.45 \cdot 3135 + 247.3 + 6088.3 = 7746 \text{ kJ/kg} \tag{2}$$

Reading from **Table 1** the power for the mirror with a radius r = 50 m, in 10 s the power beam into the asteroid is

$$E = 10 \cdot 10681.4 = 106814 \text{ kJ} \tag{3}$$

This total energy can vaporize a mass of iron given by

$$M = \frac{E}{E_1} = \frac{106814}{7746} = 14 \text{ kg} \tag{4}$$

Hitting the asteroid continuously (hundreds or thousands of times) in this manner, it can be deflected from a collision trajectory with the Earth. Even the trajectory of massive asteroids can be changed. Due to local vaporization of the asteroids, mass leads to the apparition of a reaction force produced by the expanding vapors.

In space the construction of such a gigantic system should be easier due to the absence of gravity. Calculations done using the above equations show that an SECSL having the radius of the large parabolic mirror r = 10 km can send a beam of concentrated light into the asteroid at a power of 0.427 terawatt. Such a power can vaporize an iron asteroid having the mass of 100 tons in just 8 s.

The time required to destroy or deflect an asteroid using the SECSL system is reasonably low. Practically, the asteroid can be destroyed in a few minutes because obviously the SECSL beam hits the target with the speed of light.

2.2 Heat transfer calculations

Simple calculations show that SECSL works properly both near the Earth (where irradiance Ee = 1360 W/m^2) and at 0.1 AU distance from the Sun (where irradiance is Es = 136,000 W/m^2).

Assume that a SECSL placed near the Earth having the large parabolic mirror radius r_{LPM} = 10 km and the radius of the small parabolic mirror r_{SPM} = 1.25 km; this system is capable of concentrating the sunlight by a factor of 64.

Consider that the reflection coefficient for a gold-plated foil $R_{gf/p}$ = 0.98 and the emissivity of carbon fabric/plate $e_c \approx 1$.

Assume that the whole power absorbed by the gold-plated foil is radiated according to Stefan-Boltzmann law:

$$E_e \cdot \left(1 - R_{gf/p}\right) \cdot R_{gf/p} \cdot \left(\frac{r_{LPM}}{r_{SPM}}\right)^2 = \sigma \cdot T^4 \tag{5}$$

In Eq. (1) $\sigma = 5.67 \cdot 10^{-8}$ W/m²K⁴ represents the Stefan-Boltzmann coefficient for black body radiation. Using the given data, thermal balance is achieved at T = 410 K (t = 137°C), which is under the maximum allowable working temperature for carbon composites with polymeric matrix (t = 280–300°C).

Considering that the thickness of the gold-plated foil is δ = 0.05 mm and the average thermal transfer coefficient for graphite is λ = 80 W/m K at t = 137°C, the temperature difference Δt needed for heat transfer from the gold reflective face to the rear carbon face is given by the following thermal balance equation:

$$E_e \cdot \left(1 - R_{gf/p}\right) \cdot R_{gf/p} \cdot \left(\frac{r_{LPM}}{r_{SPM}}\right)^2 = \lambda \cdot \frac{\Delta t}{\delta} \tag{6}$$

For the given equation, the thermal difference necessary for heat transfer would be Δt = 0.001°C; the result shows that heat is quickly transferred from the gold-plated face to the graphite fabric/plate due to the high thermal conductivity of the graphite and small thickness.

At the beginning of this chapter, we've stated that SECSL works properly even at 0.1 AU from the Sun, where the irradiance is 100 times stronger. Considering the same constants and mirror dimensions as before and using Eq. (1) we find that the surface temperature of the small parabolic mirror is T_{SPM} = 1296 K (t_{SPM}=1023°C) which is under the melting point of pure gold (1064°C).
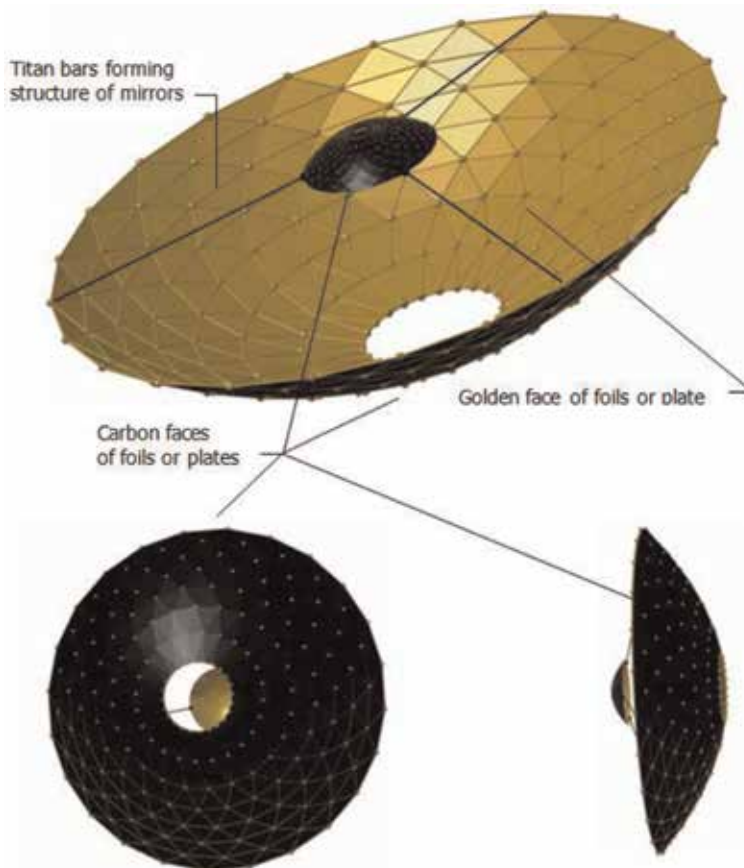
Figure 11.
SECSL equipment built using triangular cells.

Thermal balance at the surface of the large parabolic mirror is achieved at T_{LPM} = 476 K (t_{LPM} = 203°C) still under 280–300°C—the working temperature limit for carbon fiber composite with polymeric matrix.

2.3 SECSL mass calculation

In **Figure 11** the cell design is based on triangular shapes. It can be either hexagonal or rectangular cells, i.e., if rectangular cells are used, it yields a light structure, but the stability is reduced compared to the design of triangular cells. When using gold-plated foils, the structure bars can be square and straight. If gold-plated plates are used, the bars must be curved according to the parabolic surfaces of the mirrors which in this case results in a higher accuracy in focusing the light.

Such a construction can be relatively easily built in space if "SpiderFab" robots are used (see **Figure 12**) [12]. Preliminary calculations show that the resistance structure of the large parabolic mirror can be built from 528 bars with 9.3 m in length. If the bars are square tubes made from titanium having dimensions of $20 \times 20 \times 0.2$ mm^3, calculations show that the total mass is 357 kg. If graphite fiber composites are used instead of titanium, the mass of the large parabolic mirror decreases to about one-third due to the extremely low density of these materials.
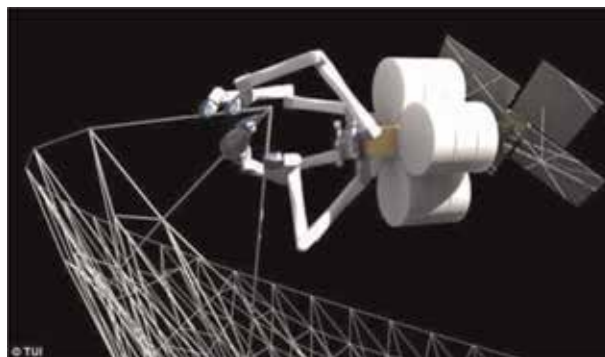
Figure 12.
NASA's SpiderFab robot in space.

3. Solar-thermal system for deorbiting space debris

This system is similar to the one presented in Chapter 2, composed of two parabolic mirrors, a large one and a small one (see **Figure 13**). Just like in the case of SECSL, the mirrors are made from very thin composite material (graphite fiber) plated with gold foils or gold plates on the concave face. The concave faces of the two mirrors face each other having the same focal point. The solar light rays which are parallel to the axis of the large parabolic mirror are reflected into its focal point and onto the small parabolic mirror and form parallel rays which are directed along the common axis. The diameter of the concentrated light beam is the same as the diameter of the small mirror ("d"). The concentrated light beam passes through a cutout (hole) in the center of the large parabolic mirror with diameter d$^+$. The hole in the large parabolic mirror is closed by a gold-plated shutter.

The system operates as follows: the system is oriented with the large parabolic mirror to the Sun using the attitude thrusters, while the shutter is closed. The light guide tube is aligned with the space debris, and the faces of the lens are curved at the appropriate radii in order to focus the light on the space debris.
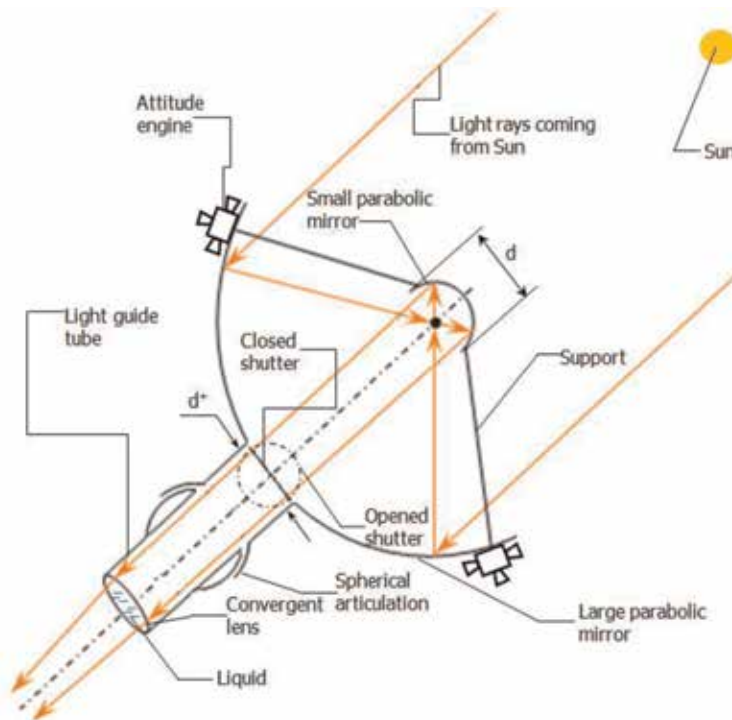
Figure 13.
Design of solar-thermal system.

When the shutter opens, the light coming from the Sun is focused by the large parabolic mirror in the common focal point and then is reflected by the small parabolic mirror toward the hole "d⁺" and the light guide tube. At the end of the light tube, the light is focused by the lens in a focal point which is positioned onto the space debris. The focused light locally vaporizes/ionizes the space debris material. The thrust force created pushes the space debris toward the Earth surface where it burns in the atmosphere.

When the shutter is closed, the light rays are sent back toward the small parabolic mirror and back to the Sun.

An alternative to the parabolic mirror system is the Cassegrain-type or Gregorian-type solar-thermal system. These systems are used in manufacturing optical telescopes or radio antennas [13].

Basically, a Cassegrain reflector (see **Figure 14**) [14] is a combination of a large concave and a small convex (hyperbolic) mirror. This design permits placing a focal point at a convenient location behind the large parabolic mirror using a compact mechanical system.

On the other hand, the Gregorian reflector [15] uses a small concave (parabolic) mirror with a focal point that doesn't coincide with the focal point of the large parabolic mirror (see **Figure 14**).

Although the Cassegrain-type and the Gregorian-type solar-thermal system can focus the light in a single point placed behind the large parabolic mirror, it is more difficult to change the focal point distance and direct the concentrated light beam onto the space debris.

3.1 Orbits for the solar-thermal system for space debris deorbiting

This system can be placed on a geocentric orbit, heliocentric orbit, or Sun-synchronous orbit. The most advantageous is the Sun-synchronous orbit (helio-
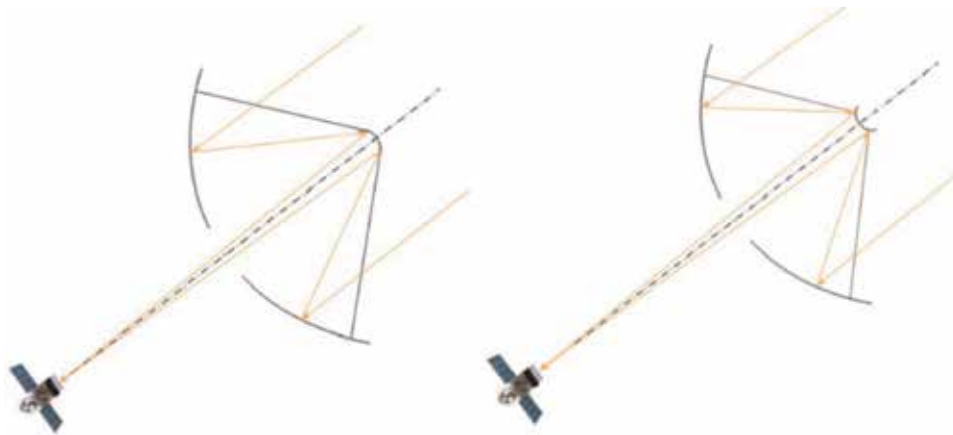
Figure 14.
Gregorian-type (left) and Cassegrain-type (right) solar-thermal systems.

synchronous orbit) [16] because the satellite is placed in constant sunlight. For example, heavy military or weather satellites are placed on Sun-synchronous orbits.

3.2 Lens design

The lens that is placed in the light tube has the role to focus the light on a very small area in order to assure very high power density. Theoretically, the energy can be focused on a geometric point. In reality due to chromatic aberration and shape errors, light is not focused quite precisely. The lens presented in **Figure 15** is made out of and elastic material filled with a colourless liquid.

Approximating surfaces "S1" and "S2" with spheres having radii "r_1" and "r_2," respectively, assuming the thickness of the lends is denoted as "d" and neglecting the optical effect of transparent elastic material (which is very thin) if the refractive index of the liquid is "n," the focal distance "f" of the lens is given by the following equation [13]:

$$\frac{1}{f} = (n-1) \cdot \left[\frac{1}{r_1} - \frac{1}{r_2} + \frac{(n-1) \cdot d}{n \cdot r_1 \cdot r_2} \right] \tag{7}$$
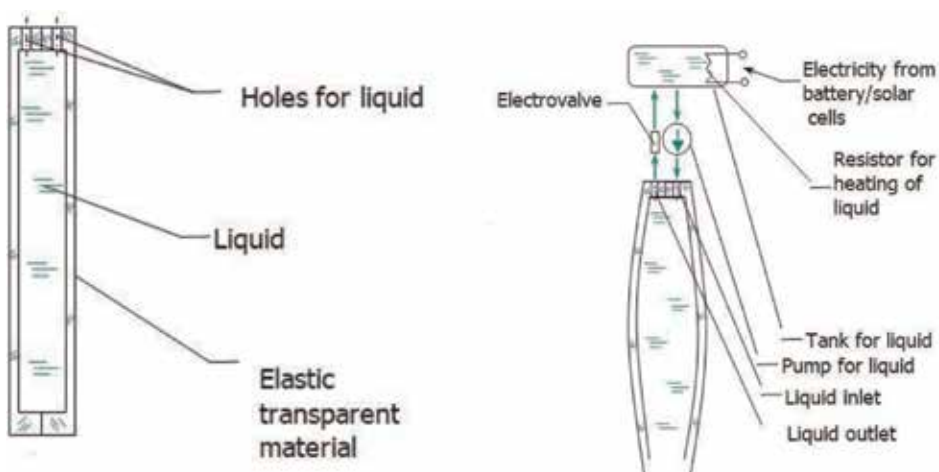
Figure 15.
Lens design filled with liquid.

In order to simplify the case of such model, consider $r_1 = r_2 = r$:

$$\frac{1}{f} = (n-1) \cdot \left[\frac{1}{r} - \frac{1}{r} + \frac{(n-1) \cdot d}{n \cdot r \cdot r}\right] = \frac{(n-1)^2 \cdot d}{n \cdot r^2} \tag{8}$$

Eq. (8) shows that for a given n and d, when $r \rightarrow \infty$ (i.e., low pressure of liquid inside the lens), $f \rightarrow \infty$, i.e., theoretically the system can hit the target (space debris) at any distance. However, due to aberration and imprecision of lens dimensions, this distance is limited. Lens operation is illustrated in **Figure 16**.

The temperature of liquid must be kept in an appropriate range for preserving the liquid state (avoiding of freezing). A resistor fed by battery charged by solar cells heats the liquid which is circulated permanently by a pump with a low speed. The electro-valve is normally opened. When hitting the space debris is necessary, the electro-valve is closed, and the liquid bends the lens to the necessary curvature. Some suitable liquids and reflective indexes are given in **Table 2** [17].

The transparent elastic material can be polydimethylsiloxane (PDMS) which has good optical properties and large elongation and is highly transparent (over 96%) in the range of visible wavelengths. PDMS refractive index is $n_{PDMS} = 1.41$. In a terrestrial application, such an elastomeric membrane having 60 microns in thickness was used in manufacturing convex lenses [18]. The refractive liquid used in that design was water.
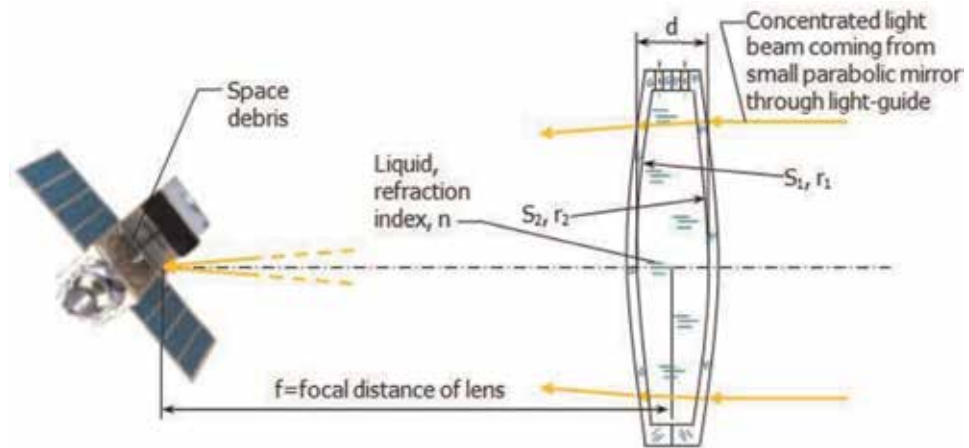
Figure 16.
How a lens filled with liquid operates to eliminate space debris.

No.	Liquid	Refractive index, n
1	Aniline	1.586
2	Benzyl benzoate	1.568
3	Ethylene glycol	1.43
4	Glycerin (glycerol)	1.47
5	Water	1.333

Table 2.
Suitable liquids for lens.

3.3 Estimated power, specific impulse, and thrust calculations

3.3.1 Estimated power calculations

The space debris is made of various metals (aluminium, titanium, carbon fiber composite, steel, etc.). For example, consider a space debris made out of aluminium. In Chapter 2 we've considered the space debris made out of iron.

Consider aluminium properties listed in the literature [19]. For simplicity they are considered constant for a wide range of temperatures:

- Melting temperature: t_m = 660.3°C, T_m = 933.3 K

- Boiling temperature: t_b = 2470°C, T_b = 2743 K

- Heat capacity (solid aluminium): c_S = 0.9 kJ/kg K

- Heat capacity (liquid aluminium): c_L = 1.18 kJ/kg K

- Heat of fusion: c_f = 398 kJ/kg (10.71 kJ/mol)

- Heat of vaporization: c_v = 6088.3 kJ/kg

- First ionization energy: c_{ion} = 577.5 kJ/mol (21,388 kJ/kg)

Using Eq. (2) for 1 kg of aluminium and assuming that the starting temperature T_0 = 0 K, the total heat needed to vaporize aluminium is

$$E_{vap} = 1 \cdot c_S \cdot (T_b - T_0) + c_f \cdot 1 + c_L \cdot (T_b - T_m) + c_v \cdot 1 \qquad (9)$$

Making the appropriate substitutions in Eq. (9) results

$$E_{vap} = 0.9 \cdot 2743 + 398 + 1.18 \cdot (2743 - 933.3) + 10518 = 15520 \text{ kJ/kg} \qquad (10)$$

The total energy needed to ionize aluminium atoms after vaporization is

$$E_{ion} = E_{vap} + c_{ion} = 15520 + 21388 = 36908 \text{ kJ/kg}$$

In **Table 3** the amount of aluminium that the system can vaporize and ionize in 1 s is presented.

3.3.2 Estimated specific impulse and thrust calculations

The process of generating reaction force due to material ablation is very complex. This effect was observed by pointing a laser to a material surface [20]. In this present case, the process should be similar.

In the case of laser rays, ablation takes place when the material is removed from a substrate through direct absorption of laser ray energy. As a first condition, the radiation energy must exceed a given threshold, which is less than 10 J/cm^2 for metals, 2 J/cm^2 for insulating inorganic materials, and 1 J/cm^2 for organic insulation materials [20].

The solar-thermal system discussed here (see **Table 2**, case no. 1) satisfies this requirement because, even when the power of the smallest mirror is $0.98 \times 0.98 \times 88.4$ = 84.9 kW, it provides an energy of 10 J in 1.18×10^{-4} s [20].

Case no.	Radius of large parabolic mirror, r_{lpm} (m)	Collected solar power, P (kW)	Flow of aluminium vapors per second, g	Flow of aluminium ions (first level) per second, g
1	5	88.4	6	2
2	7.5	240.3	15	7
3	10	427.3	28	12
4	15	961.3	62	26
5	20	1709.0	110	46
6	25	2670.3	172	72

Table 3.
The quantity of aluminium vaporized by the system in 1 s.

Another condition is related to the energy absorption mechanism. Chemical composition, microstructure, and morphology of material strongly influence the absorption of heat.

Heating debris must be sufficiently fast for homogenous nucleation and expansion of vapor bubbles and ions.

Some simulations done for interaction of laser rays have shown that [21]:

- The degree of light absorption increases as the cavity deepens.

- Maximum energy absorbed by the cavity is around 80% of the total energy of radiation.

- The radiation is multiple times reflected by the cavity, and as a result, the energy is highly concentrated at the center and the bottom of the cavity and forms the final conical shape of the cavity.

- The surface temperature is much higher than the normal boiling point.

- In order to be able to remove the material, it must have a homogenous boiling regime and evaporation; the power intensity must be over 108 W/cm^2.

Note: The mentioned simulations have been conducted only for iron, not for aluminium or other materials currently used in manufacturing satellites and space equipment, but the effect should be similar (**Figure 17**).

In some experiments a specific impulse of around 4000 s was measured for carbon and aluminium in ionized state produced by the laser ray [23]:

During those experiments the following observations were made:

- The speed of the ejected atoms and implicitly Isp is inversely proportional to the square roots of the atomic mass of ablated material; the lighter the element the higher the specific impulse.

- Thrust tends to increase with atomic mass of ablated material.

- The speed of the ejected atoms was independent of angle at 22 cm away from the target.

- The ablation time was 1.5 s.
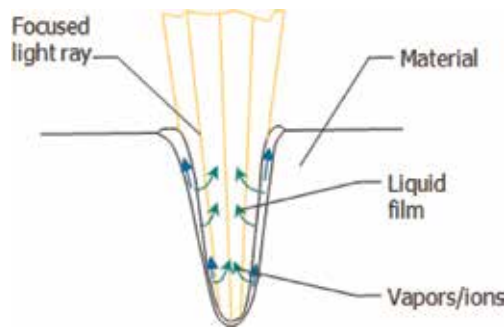
Figure 17.
The effect of a focused light ray on a material [22].

For the case where Isp has a known value, one can evaluate the thrust force by the following equation:

$$T_f = g_0 \cdot I_{sp} \cdot \dot{m} \tag{11}$$

where g_0 represents the gravitational acceleration at the Earth's surface (g_0 = 9.81 m/s^2). $\dot{m}$ represents the mass of ions ejected in 1 s.

Momentum coupling coefficient C_m is another method for thrust evaluation [20]. This coefficient characterizes thrust production efficiency. The coefficient is determined as the thrust to laser power ratio. This parameter determines the minimum light power required to produce a 1 N thrust:

$$C_m = \frac{T_f}{P} \tag{12}$$

According to the above reference, $C_{m\ max}$ Al = 6·10−5 N/W for aluminium. That means that in the case of ablation of a space debris made of aluminium using a solar-thermal system with a power of P = 88.4 kW, the thrust force resulted is

$$T_f = P \cdot C_{m\ max\ Al} = 88400 \cdot 6 \cdot 10^{-5} = 5.3 \text{ N} \tag{13}$$

In case the large parabolic mirror has a diameter of r_{lpm} = 25 m, the thrust force is

$$T_{f\ 25} = P \cdot C_{m\ max\ Al} = 2670300 \cdot 6 \cdot 10^{-5} = 160.2 \text{ N} \tag{14}$$

In both cases the thrust force is remarkably high and can deorbit space debris with just a few hits.

4. A new design of space equipment for rapid disintegration in atmosphere after reentry

This new design is inspired by the tragic loss of the Space Shuttle Columbia's crew on February 1, 2003 [24]. Columbia disintegrated over Texas and Louisiana when it reentered the Earth's atmosphere. During the launch of the space shuttle, a piece of foam insulation struck the left wing of the orbiter deteriorating its ablative protection [24]. When time came for the space shuttle to reenter the Earth's atmosphere, the damage caused by the foam insulation allowed hot air to penetrate into

the wing creating an irregular hole. Air entered the left wing with high speed, quickly became very hot when stagnating, and destroyed the internal structure of the wing.

4.1 Lessons learned after the Space Shuttle Columbia disaster

During the reentry phase, shock waves produced by hypersonic velocities and the frictional effect of the atmosphere began to heat Columbia's surface. The temperature varied depending on location: the orbiter's nose and leading edges of the wing experiencing temperatures greater than 1538°C [25].

The breach created during launch in the ablative protection of the left wing allowed for hot gases to penetrate the wing and to advance in the same direction inside the wing and to the fuselage (see **Figure 18**). This phase became known as "phase I" from "Initialization."

During the "Initialization" phase, the wing lost its aerodynamic characteristics, and the destruction process was extremely short, lasting from 13:59:37.5 GMT to 13:59:39.7 GMT (2.2 s) (see **Figure 19**) [25].

The "Acceleration" phase quickly followed the "phase I" which lasted for 0.07 s. The destruction continued with total dispersal of the space vehicle and burning in the atmosphere (see **Figure 20**). This phase can be called "phase D" from "Dispersal" and lasted for 55 s (**Figure 21**).

4.2 Space equipment for rapid disintegration during atmosphere reentry

As presented in Chapter 1, ESA's "Design for Demise" concept must be implemented in every space equipment. Following those guidelines, the present paper presents a new vision of that concept.
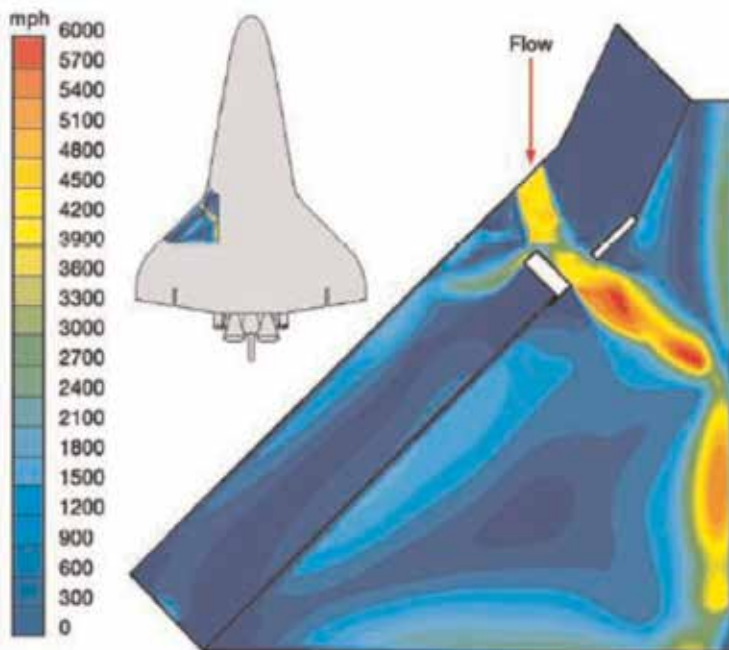
Figure 18.
Velocity distribution on Columbia's left wing at the beginning of the disaster (phase I) [25].
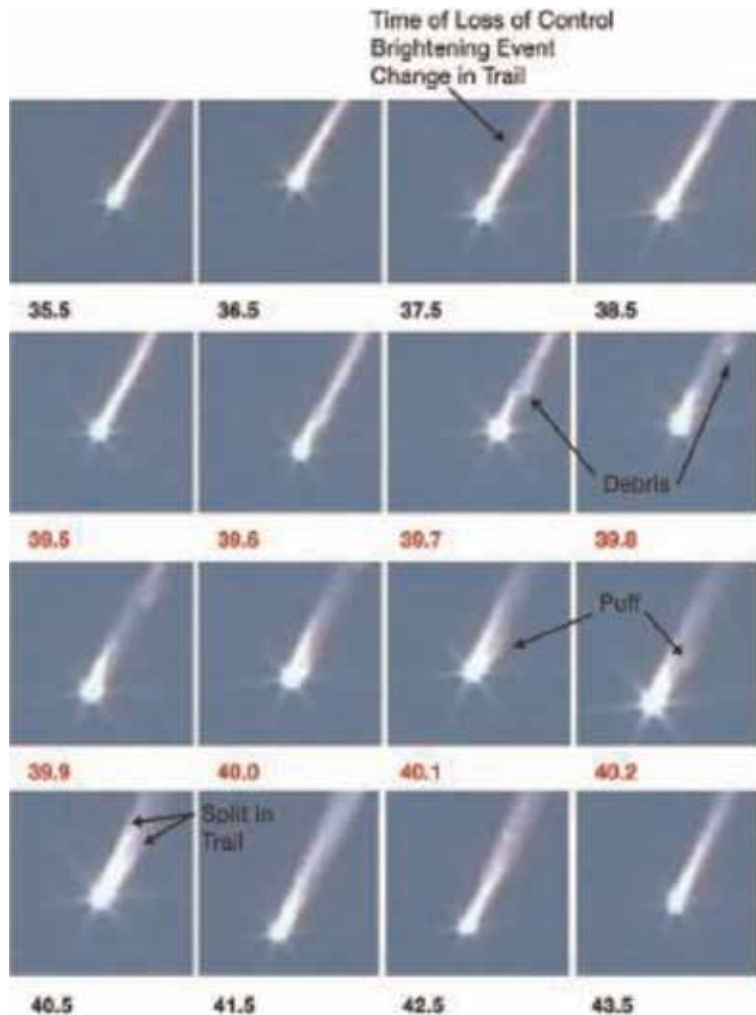
Figure 19.
Initiation phase of the destruction process (phase I) [25].

Figure 20.
Acceleration phase of the destruction process (phase A) [25].

It is known that satellite equipment is covered by a protection box which shields them against environmental factors such as cosmic radiation, solar wind, light (ultraviolet, visible, infrared), cosmic dust, and rarefied atmosphere. Usually, this box is a prism which has a pretty low dynamic drag, and, as a result, reaching high temperatures on the surface of the satellite is delayed; therefore the satellite disintegration is delayed during reentry. The situation is even more critical in the

Figure 21.
Total dispersal phase (phase D) [25].

case of the last stages of launching rockets which have a good aerodynamic shape in order to have a low aerodynamic drag during the ascending phase of the launch.

According to the space equipment design presented in this paper, special doors must be incorporated in the external fairing of the space equipment. The holes in the fairing can have any shape (rectangular, triangular, hexagonal, circular, etc.) depending on the position of the fairing. Doors fitted on every hole must be articulated by a cylindrical articulation (i.e., to permit a rotation of the door around an axis); this allows the door to open to the interior of the box when external pressure increases and to close when the pressure inside the fairing is higher than the external pressure. The door is fixed to the fairing through brazing with low fusible metals or strong resins (Loctite, Araldite) which decompose at low temperatures (150–200 to 700°C in special cases). Both the resin and metallic alloys must be extremely resistant at low temperatures but must lose their strength when temperature reaches several hundreds of degree Celsius. In in the early stages of the reentry, the epoxy resins decompose at temperatures between 150 and 200°C, and the braze alloys are melting when the local temperature reaches 200–700°C. As a result, the doors (covers) are pushed inside the fairing, and the external air enters inside where stagnates reach extremely high temperatures. The new external geometry of the space equipment leads to an increase of aerodynamic drag and converts kinetic energy into heat, which enhances the burning process.

By placing more doors on the fairing, no matter how the space equipment rotates during reentry, at least one door is opened by the dynamic pressure, and the rest of them are closed by the same dynamic pressure. Heating inside the fairing is maximum due to air stagnation, which leads to a rapid disintegration of the space equipment.

If the covers (doors) are not articulated, they are pushed inside the equipment by the ambient pressure acting on the surface of the fairing. Being pushed inside, the doors allow the air to flow inside the fairing around the equipment, but does not stagnate; thus heating does not occur, and the aerodynamic drag is low. For this reason the heating hate will be lower than when articulated covers are used.

For an even faster disintegration of the space equipment, the satellite components are wrapped in 0.05-mm thick aluminium or magnesium foil. These lightweight foils will burn first followed shortly by the equipment. This new technology can be seen in **Figures 22–27**.

Applying this design will determine the space debris to be disintegrated according to Space Shuttle Columbia's tragic disintegration phases I, A, and D.
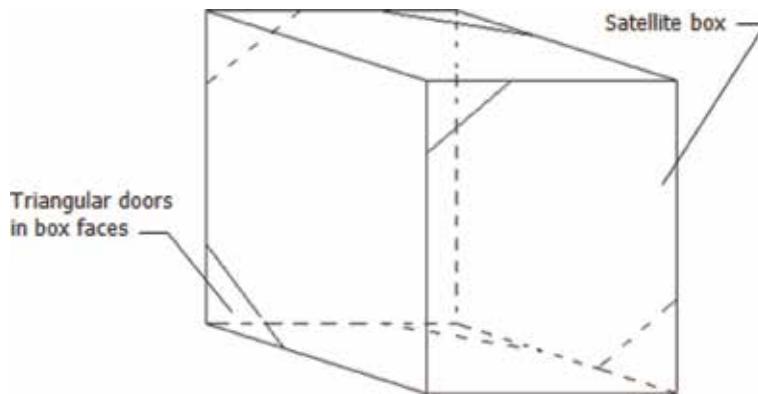
Figure 22.
Example of satellite box with doors.
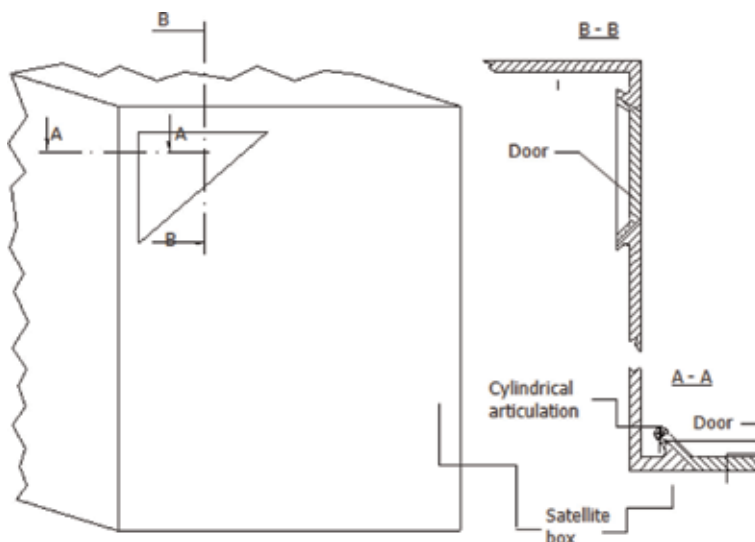
Figure 23.
Articulated door design.
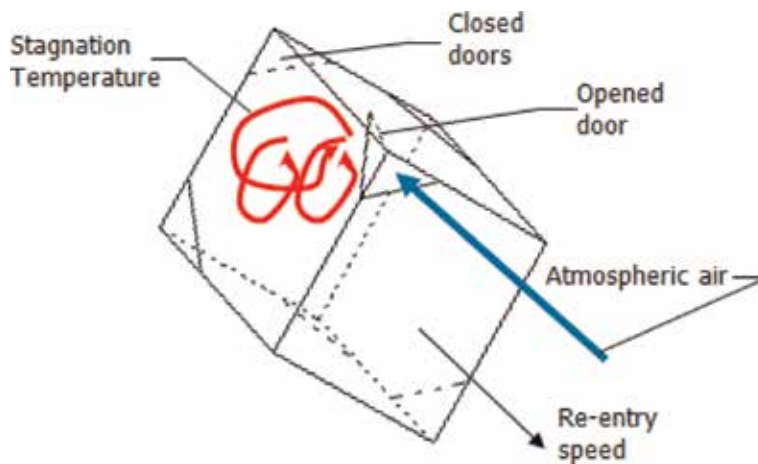
Figure 24.
Stagnation temperature inside the satellite box.
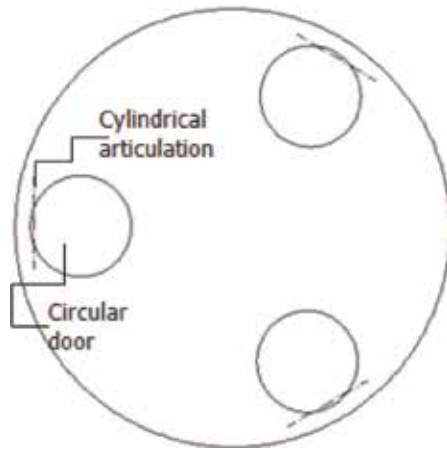
Figure 25.
Example of fuel tank with articulated circular doors.
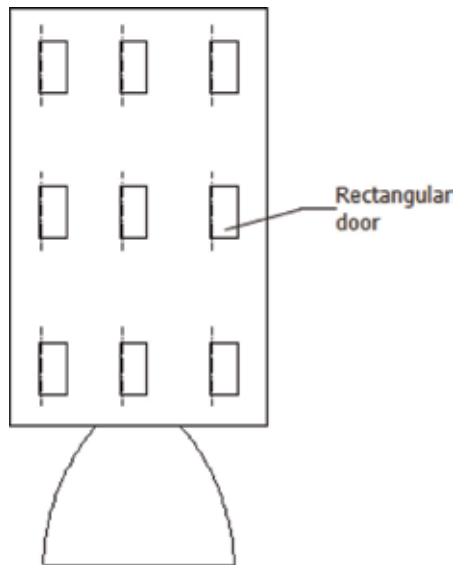
Figure 26.
Example of last-stage rocket with articulated rectangular doors.
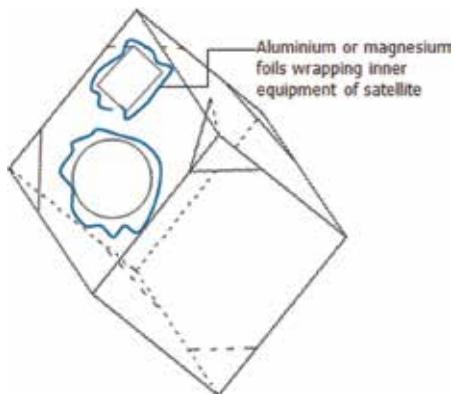
Figure 27.
Example of satellite equipment wrapped in aluminium or magnesium foil.

Author details

Constantin Sandu[1*], Cristian-Teodor Olariu[1] and Radu-Constantin Sandu[2]

1 Romanian Research and Development Institute for Gas Turbines-COMOTI, Bucharest, Romania

2 S.C. Structural Management Solutions S.R.L., Bucharest, Romania

*Address all correspondence to: constantin.sandu@comoti.ro

IntechOpen

References

[1] Inside NASA's Plan to Catch an Asteroid. [Internet]. Available from: https://www.space.com/20612-nasa-asteroid-capture-mission-explained.html. [Accessed: 2019-05-29]

[2] Fifth European Conference on Space Debris. [Internet]. Available from: https://www.esa.int/About_Us/ESOC/Fifth_European_Conference_on_Space_Debris_to_address_key_issues. [Accessed: 2019-05-29]

[3] Ze Z. Space debris and present active debris removal techniques. In: Beijing Space Sustainability Conference; 13–14 October, 2011; Beijing; 2011

[4] Debris objects in low-Earth orbit (LEO). [Internet]. Available from: http://www.esa.int/spaceinimages/Images/2008/03/Debris_objects_in_low-Earth_orbit_LEO. [Accessed: 2019-05-29]

[5] Space Debris and Space Traffic Management. [Internet]. Available from: https://aerospace.org/article/space-debris-and-space-traffic-management. [Accessed: 2019-05-29]

[6] Alby F. Spot 1 end of life disposition maneuvers. Advances in Space Research. 2005;**35**:1335-1342

[7] SP1301-Position Paper-Space Debris Mitigation-Implementing Zero Debris Creation Zones. European Space Agency. [Internet]. Available from: http://www.esa.int/esapub/sp/sp1301/sp1301.pdf. [Accessed: 2019-05-29]

[8] Space Debris. [Internet]. Available from: http://www.esa.int/Our_Activities/Operations/Space_Debris/Mitigating_space_debris_generation. [Accessed: 2019-05-29]

[9] Solar Energy Fundamentals. [Internet]. Available from: http://physics.oregonstate.edu/~giebultt/COURSES/ph313/ppt/Ch06.1.pdf. [Accessed: 2019-05-29]

[10] Gold Coating. [Internet]. Available from: https://spinoff.nasa.gov/spinoff1997/hm2.html. [Accessed: 2019-05-29]

[11] The melting temperature of pure iron. [Internet]. Available from: https://www.chegg.com/homework-help/questions-and-answers/24-melting-temperature-pure-iron–1538-c-b-400-c-c-1147-c-d-727-c-25-eutectic-concentratio-q13180725. [Accessed: 2019-05-29]

[12] Robert P, Hoyt RP. An Architecture for Self-Fabricating Space Systems, AIAA SPACE 2013 Conference and Exposition; September 2013. DOI: 10.2514/6.2013-5509

[13] Electronic Imaging in Astronomy: Detectors and Instrumentation. McLean S. Springer Science & Business Media; 17 August, 2008. p. 86

[14] All-reflecting Two-mirror Telescopes. [Internet]. Available from: https://www.telescope-optics.net/two-mirror.html. [Accessed: 2019-05-29]

[15] Gregory James: Optica Promota; 1663. [Internet]. Available from: http://www.17centurymaths.com/contents/James%20Gregory/Definitions%20&%20Introductory%20Material.pdf. [Accessed: 2019-05-29]

[16] Geometry of a Sun-Synchronous Orbit. [Internet]. Available from: https://landsat.gsfc.nasa.gov/geometry-of-a-sun-synchronous-orbit/. [Accessed: 2019-05-29]

[17] Refractive Index for some common Liquids, Solids and Gases. [Internet]. Available from: https://www.engineeringtoolbox.com/refractive-index-d_1264.html. [Accessed: 2019-05-29]

[18] Tunable-focus liquid lens controlled using a servo motor. [Internet].

Available from: https://www.
osapublishing.org/oe/fulltext.cfm?uri=
oe-14-18-8031&id=97917. [Accessed:
2019-05-29]

[19] Aluminium- Specifications,
Properties, Classifications and Classes.
[Internet]. Available from: https://www.
azom.com/article.aspx?ArticleID=2863.
[Accessed: 2019-05-29]

[20] Phipps C, Birkan M, Bohn W,
Eckel H-A, Hirosawa H, Lippert T, et al.
Review: Laser ablation propulsion.
Journal of Propulsion and Power.
July-August, 2010;**26**(4)

[21] Brown MS, Arnold CB.
Fundamentals of laser-material
interaction and application to multiscale
surface modification. In: Sugioka K
et al., editors. Laser Precision
Microfabrication. Springer Series in
Materials Science. Vol. 135. Berlin,
Heidelberg: Springer-Verlag; 2010,
2010. DOI: 10.1007/978-3-642-10523-
4__4

[22] Ki H, Mohanty PS, Mazumder J.
Modelling of high-density laser–
material interaction using fast level set
method. Journal of Physics D: Applied
Physics. 2001;**34**:364-372

[23] Pakhomov A, Thompson MS, Swift
W Jr, Gregory DA. Ablative laser
propulsion: Specific impulse and thrust
derived from force measurements.
AIAA Journal. November, 2002;**40**(11):
2305-2311. DOI: 10.2514/2.1567

[24] Cause and Consequences of the
Columbia Disaster. [Internet]. Available
from: http://www.spacesafetymagazine.
com/space-disasters/columbia-disaster/
columbia-tragedy-repeated/. [Accessed:
2019-05-29]

[25] Columbia Crew Survival
Investigation Report- NASA/SP-2008-
565. [Internet]. Available from: https://
www.nasa.gov/pdf/298870main_SP-
2008-565.pdf. [Accessed: 2019-05-29]

Solar System Exploration Augmented by In Situ Resource Utilization: System Analyses, Vehicles, and Moon Bases for Saturn Exploration

Bryan Palaszewski

Abstract

Human and robotic missions to Saturn are presented and analyzed with a range of propulsion options. Historical studies of space exploration, planetary spacecraft and astronomy, in situ resource utilization (ISRU), and industrialization all point to the vastness of natural resources in the solar system. Advanced propulsion is benefitted from these resources in many ways. While advanced propulsion systems were proposed in these historical studies, further investigation of nuclear options using high-power nuclear electric and nuclear pulse propulsion as well as advanced chemical propulsion can significantly enhance these scenarios. Updated analyses based on these historical visions are presented. At Saturn, nuclear pulse propulsion with alternate propellant feed systems and Saturn moon exploration with chemical propulsion and nuclear electric propulsion options are discussed. Issues with using in situ resource utilization on Saturn's moons are discussed. At Saturn, the best locations for exploration and the use of the moons as central locations for Saturn moon exploration are assessed. Environmental issues on Titan's surface may present extreme challenges for some ISRU processes. In-space bases for moon-orbiting propellant processing and ground-based processing will be assessed.

Keywords: in situ resource utilization (ISRU), moon base, rocket propulsion, systems analysis, specific impulse, nuclear propulsion

1. Introduction

Exploration and utilization of the outer solar system have always been a goal of the planetary science community and spacecraft engineers. Saturn with its fantastic ring system and many diverse moons has been the focus of exploration by the two Voyager flyby missions and the orbiting Cassini spacecraft. These space vehicles have identified areas of great scientific interest and also places on the moons where water, cryogenic ices, and other natural resources can be gathered. Using in situ resource utilization (ISRU) will allow more extensive exploration of the planet and its moons. This chapter presents analyses of the transportation options in the Saturn system, such as nuclear electric orbital transfer vehicles and chemical propulsion

moon landers. Far future human exploration, using nuclear propulsion is also addressed. A combination of these technologies may allow excellent surveys of the moons and then finally human exploration and perhaps moon base construction.

2. In situ resource utilization (ISRU)

In situ resource utilization (ISRU) is the use of materials on other bodies in the solar system. These in situ materials can be in the regolith, the atmosphere, or any other part of the natural environment. Using ISRU on or in the vicinity of many planetary bodies has been studied for decades. Numerous experiments have been conducted to define the methods of extracting resources from ices, gases, and regolith. Some of the earliest ISRU experiments were conducted in 1965 [1]. Based on spectroscopic measurements from Earth, simulated lunar rock and dust were created. The simulated rock and dust were then subjected to chemical processes that were designed to extract oxygen from the lunar materials [1]. Mars ISRU has been addressed in numerous references [2–6]. Reference [6] (JSC) discusses the six steps in ISRU development: identification, prospecting, resource capturing, utilization (propellants, etc.), power generation, and manufacturing. Additional extensive experiments and analyses are planned for the Mars 2020 rover, with an experiment called MOXIE that will separate oxygen from Mars' carbon dioxide atmosphere [7]. A concerted effort of many organizations, the commercial lunar propellant architecture, was focused on the efforts to capture lunar polar ice [8]. Using ISRU on outer planet moons was addressed in Refs. [9, 10] (HOPE, Ash, and BP). Outer planet analyses for capturing fusion fuels from Uranus and Neptune were conducted in Refs. [11–13].

3. Saturn and its moons

Saturn is the second largest planet in the solar system. Its orbit has an average distance from the Sun of 1.433 million km. The ring system surrounding Saturn is very extensive and spectacular and has a rich set of resonances and dynamics. The Cassini mission spacecraft instruments gathered a rich set of data throughout its lifetime. Saturn also has powerful radiation belts both near the planet and far beyond the ring system. Due to the radiation environment, the moons are a more important location for any spaceflight operations.

Based on the observations of the Voyager and Cassini spacecraft, the moons of Saturn contain a rich set of ices. Spectroscopic data show the nature of these ices to be water ice with other frozen gases: nitrogen, methane, etc. The moons' temperatures are in the range on 75–130 K. **Table 1** provides the density of the major moons. The relatively low density also implies that the moons are primarily composed of frozen ices.

Figure 1 shows the semimajor axes of the moon. Iapetus is the most distant at 3.56 million km from Saturn. The most proximate major moon is Mimas, which is only 185,000 km from Saturn [14–19]. Additional references on the moons of Saturn are provided at the end of this chapter [20–30].

3.1 Enceladus

Enceladus is a small icy moon near the outermost ring of Saturn; its radius is 248 km. Its semimajor axis is 238,020 km. Its gravity level is 2×10^{-2} of Earth's gravity. This moon is particularly exciting as it is sewing water into space, and its water

Moon	radius (km)	mass (10^20 kg)	density (kg/m^3)
Mimas	191.0	0.38	1,152.0
Enceladus	248.0	1.08	1,606.0
Tethys	526.0	6.18	956.0
Dione	560.0	10.96	1,470.0
Rhea	762.0	23.10	1,234.0
Titan	2,575.0	1,345.50	1,880.0
Iapetus	712.0	18.10	1,088.0

Table 1.
Saturn moon density, modified from Ref. [14].
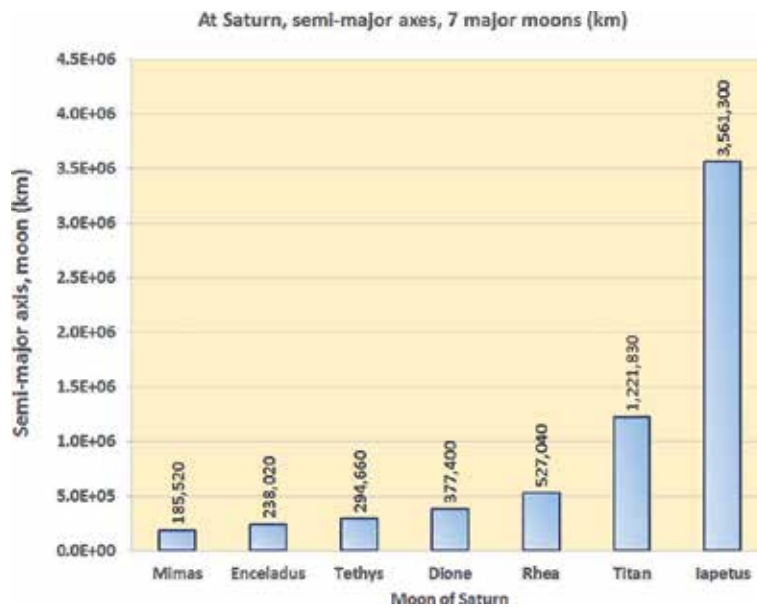
Figure 1.
Semimajor axes of the seven major moons of Saturn.

is feeding mass to Saturn's rings. The water plume emanates from the so-called tiger stripes in the southern hemisphere. The temperature of the tiger stripes is 10–100°K warmer than the surrounding icy surface. The Cassini spacecraft had made multiple flybys of Enceladus and detected organic molecules in the water plume. Thus, this moon may harbor the precursors of simple life forms.

3.2 Titan

Titan is the largest moon of Saturn with a radius of 2576 km. Its semimajor axis is 1.2218 million km. Titan has an appreciable atmosphere of 98.4% nitrogen, 1.4% methane, and other trace gases. Its gravity is 0.14 of Earth's gravity. Because of its dense clouds, radar must be used to gather data from space. The Cassini spacecraft observed lakes on Titan; these lakes are composed of liquid methane and ethane. These lakes are approximately that size of the Great Lakes of North America. The surface of Titan is approximately 94°K, and the surface is a complex crust of water ices and frozen hydrocarbons. Simulations and gravity data suggest an ocean of liquid water about 100 km below the frozen surface.

Body	R (km)	m (kg)	a (m/s^2)	G level
Saturn	60,268.0	5.6800E+26	1.0434E+01	1.066E+00
Mimas	191.0	3.7900E+19	6.9321E-02	7.079E-03
Enceladus	248.0	1.0800E+20	1.1717E-01	1.197E-02
Tethys	526.0	6.18E+20	1.4904E-01	1.522E-02
Dione	560.0	1.1000E+21	2.3405E-01	2.390E-02
Rhea	762.0	2.3100E+21	2.6546E-01	2.711E-02
Titan	2,575.0	1.3455E+23	1.3540E+00	1.383E-01
Iapetus	712.0	1.8100E+21	2.3824E-01	2.433E-02

Table 2.
Gravity levels of Saturn and its major moons.

3.3 Iapetus

Iapetus is one of the most distant large moons from Saturn, and its radius is 712 km. Its gravity level is 2.4×10^{-2} of Earth's gravity. This moon has a ridge that girdles a significant fraction of the equator. One hemisphere has very dark material, with an albedo is 2–6%, while the other hemisphere in comparison is very bright. The composition of the dark material is perhaps organic material and carbon. Simulations have suggested that the dark materials may have been deposited by numerous particle collisions. An alternative theory is that magma from the interior has risen to the surface and that magma may be visible in photos as materials that have filled in numerous craters.

3.4 Icy moon gravity levels

Table 2 provides the gravity levels of the major moons. While Titan has a surface gravity level of 14% of Earth, the remaining moons have gravity levels of 1×10^{-2} Earth gravity or less. Such low gravity levels may make transportation, operations, and industrial processing on the moon's surfaces very challenging. On the other hand, the low gravity is helpful is reducing the delta-V needed to transport large masses to and from the moon's surface.

4. Mission planning and delta-V data

Table 3 provides the delta-V to reach low orbit about the moon and the moon's escape velocities. As Titan is the largest moon, the delta-V for escape is the largest: 3.17 km per second. These delta-V values will be important in selecting the most attractive moons for ISRU processing. The planetary gravitational constants and radii were found in Ref. [19].

4.1 Exploration vehicles

As a prelude to human missions, a detailed survey of the major Saturnian moons is planned. The survey is driven by ISRU requirements: identification, prospecting, resource capturing, and utilization. The final steps will be power generation and manufacturing on the surface of the moons.

A first survey of the major moons will include orbiters and small landers. A suggested set of spacecraft would be nuclear electric propulsion transfer vehicle and a small chemical propulsion lander. The NEP transfer vehicle would use a complement

Body	G (km^3/s^2)	R (km)	r, or altitude (km)	Estimated landing or ascent delta-V (km/s), with 20% gravity losses	Escape velocity (km/s), with 20% gravity losses
Saturn	3.7931E+07	60,268.0	10	30.102	42.575
Mimas	2.5290E+00	191.0	100	0.112	0.195
Enceladus	7.2065E+00	248.0	100	0.173	0.289
Tethys	4.1237E+01	526.0	100	0.308	0.475
Dione	7.3400E+01	560.0	100	0.400	0.614
Rhea	1.5414E+02	762.0	100	0.507	0.763
Titan	8.9781E+03	2,575.0	100	2.198	3.169
Iapetus	1.2078E+02	712.0	100	0.463	0.699

Table 3.
Landing, launch, and escape of delta-V for the seven major moons of Saturn.

of science instruments to assess the ices and regolith on the moons' surface. A mega-watt class radar system aboard the orbiter would provide data on ice thicknesses and regolith composition. Once an attractive site is identified, the chemical propulsion lander can descend to the surface and perform a series of in situ assessments. Chemical laboratories delivered to the surface can sample the ices and regolith. Samples may even be returned to orbit for caching and planned return to Earth.

4.2 Space vehicle sizing

The nuclear electric propulsion (NEP) vehicles or orbital transfer vehicles (OTVs) are described by the following mass scaling equation. The dry mass scaling equation used was [31–35]

$$\text{Mdry, stage (kg)} = \text{reactor specific mass (kg/kW)} \bullet P \text{ (kWe)} \\ + 0.05 \bullet M_p \text{ (kg)} + \text{fixed mass (kg)}$$

The low-thrust OTV delta-V values are noted in **Tables 4** and **5** for each round-trip mission.

The NEP vehicle has a specific impulse of 5000 seconds with a propulsion system efficiency of 50%. The power level of the reactor was 10 MWe, and the reactor specific mass was 10 kg/kWe. The propellant tankage dry mass fraction was 5%, and the fixed mass was 20 MT [31]. Additional mission assumptions are discussed in the next sections.

The chemically propelled oxygen/hydrogen propulsion landers were described with a mass scaling equation. In sizing the chemical propulsion landers, a vehicle mass scaling equation was used [31–35]:

$$M_{dry,stage} \text{ (kg)} = M_{dry,coefficient} \bullet M_p \text{ (kg)}$$

where $M_{dry,stage}$ is the stage dry mass, including residual propellant (kg); $M_{dry,coefficient}$ is the B mass coefficient (kg of tank mass/kg of usable propellant mass); M_p is the usable propellant mass (kg).

In almost every case, the chemical propulsion landers had a B coefficient of 0.4. With the very large delta-V missions at Titan, the B coefficient was 0.2. The lander specific impulse was 480 seconds [31, 36–38].

Moon	Mimas	Enceladus	Tethys	Dione	Rhea	Titan	Iapetus	Total
Mimas	0.000	3.530	5.903	8.594	11.639	17.443	22.584	69.694
Enceladus	3.530	0.000	2.829	5.191	8.273	14.088	19.391	53.303
Tethys	5.903	2.829	0.000	2.848	5.775	11.554	16.699	45.608
Dione	8.594	5.191	2.848	0.000	3.084	8.897	14.261	42.876
Rhea	11.639	8.273	5.775	3.084	0.000	5.817	11.210	45.797
Titan	17.443	14.088	11.554	8.897	5.817	0.000	5.693	63.491
Iapetus	22.584	19.391	16.699	14.261	11.210	5.693	0.000	89.837
	69.694	53.303	45.608	42.876	45.798	63.491	89.837	

Table 4.
Round-trip delta-V map for Saturn's moons (seven moons).

Moon	Mimas	Enceladus	Tethys	Dione	Rhea	Titan	Total
Mimas	0.000	3.530	5.903	8.594	11.639	17.443	47.110
Enceladus	3.530	0.000	2.829	5.191	8.273	14.088	33.911
Tethys	5.903	2.829	0.000	2.848	5.775	11.554	28.909
Dione	8.594	5.191	2.848	0.000	3.084	8.897	28.615
Rhea	11.639	8.273	5.775	3.084	0.000	5.817	34.588
Titan	17.443	14.088	11.554	8.897	5.817	0.000	57.798
Total	47.110	33.911	28.909	28.615	34.588	57.799	

Table 5.
Round-trip delta-V map for Saturn's moons (six moons, without Iapetus).

4.3 Mission delta-V results

Examples of the chemical propulsion lander masses are shown in **Figures 2** and **3**: Titan and Enceladus, respectively. At Titan and Enceladus, the smallest 1 MT payload landers would be for ISRU prospecting and exploration. The 50 MT payload landers would be for industrial scale ISRU propellant production plant delivery.

The NEP vehicle delta-V values are shown in **Tables 4** and **5**. The delta-V was computed with a low-thrust trajectory estimation algorithm. **Table 4** shows the round-trip delta-V values for trips between the seven major moons; the table shows that using Dione as a central exploration moon, the total delta-V for a fleet of OTVs is minimized. An option with only six moons was also investigated, noted in **Table 5**. As Iapetus is the most distant moon in the system of moons, a separate analysis was conducted excluding Iapetus. For both the seven moon and the six moon options of **Tables 4** and **5**, the moon Dione shows the minimal fleet delta-V. Though this is the moon showing the minimal delta-V for the entire fleet, the influence of the OTV and lander mass may change the optimal (or minimal mass) solution.

At Saturn: Titan Lander Mass (MT), Two-Way Flights,
delta-V = 6.34 km/s , Isp = 480 s, M,tank = 0.2 M,p

	1	2	3	4
☐ Payload mass (MT)	1	5	10	50
▪ Lander mass (MT)	9.8	49.0	98.0	490.2

Y-axis: Lander mass (MT)
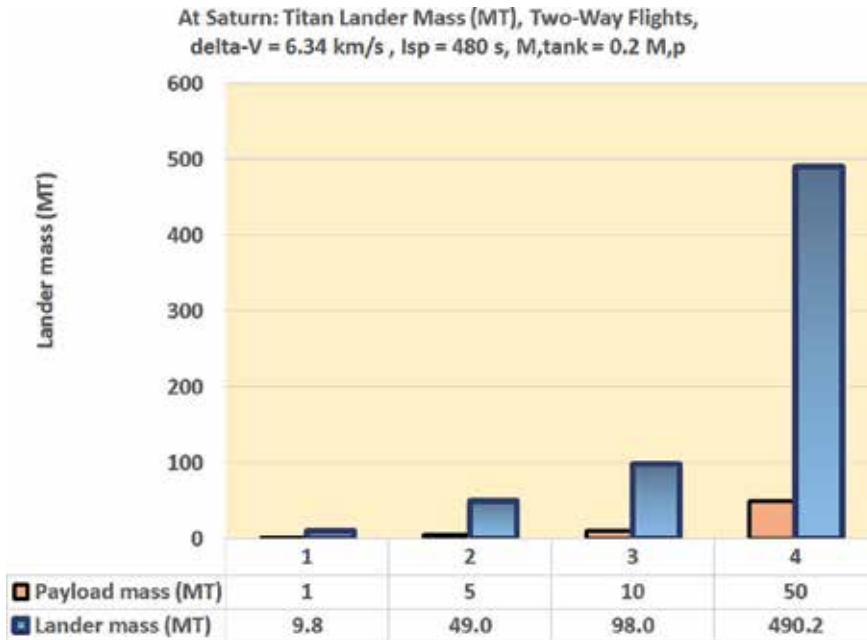
Figure 2.
Saturn moon lander mass for Titan, round-trip flights, payload masses of 1–50 MT.

At Saturn: Enceladus Lander Mass (MT), Two-Way Flights,
delta-V = 0.6 km/s , Isp = 480 s, M,tank = 0.4 M,p

	1	2	3	4
☐ Payload mass (MT)	1	5	10	50
☐ Lander mass (MT)	1.3	6.6	13.2	66.1

Y-axis: Lander mass (MT)
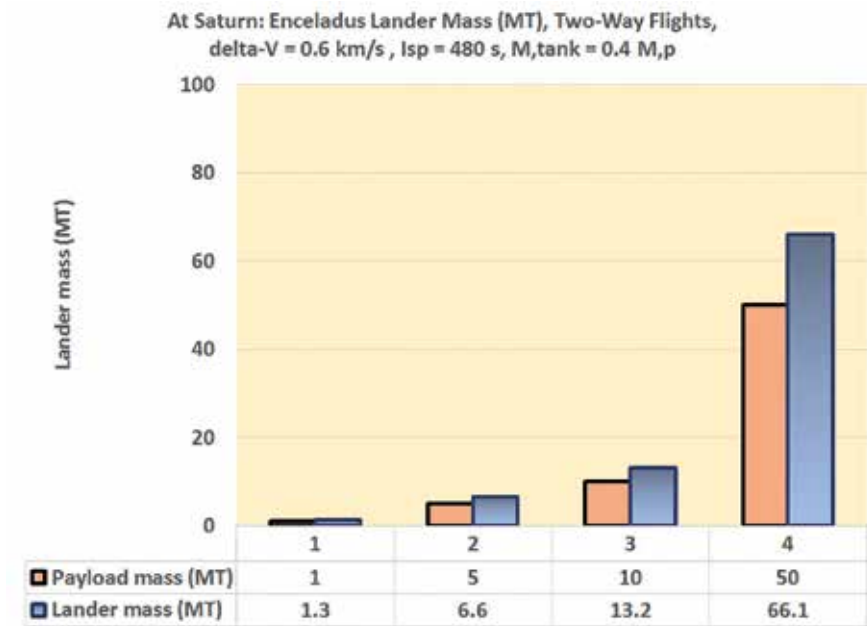
Figure 3.
Saturn moon lander mass for Enceladus, round-trip flights, payload masses of 1–50 MT.

4.4 Factory analysis

The ISRU factory will allow the OTV to be refueled from water ices on the moons. Initially, the OTVs, their science landers, and factory lander are delivered to the centric moon. The OTVs are delivered with no NEP propellants and only

Moon Base Water Processing Factory Mass, 50 MT Hydrogen Payload (OTV Propellant), B = 0.2

	Light	Heavy	LW	SLW
450 Isp	31.8	37.8	28.8	26.8
460 Isp	31.3	37.3	28.3	26.3
480 Isp	30.5	36.5	27.5	25.5
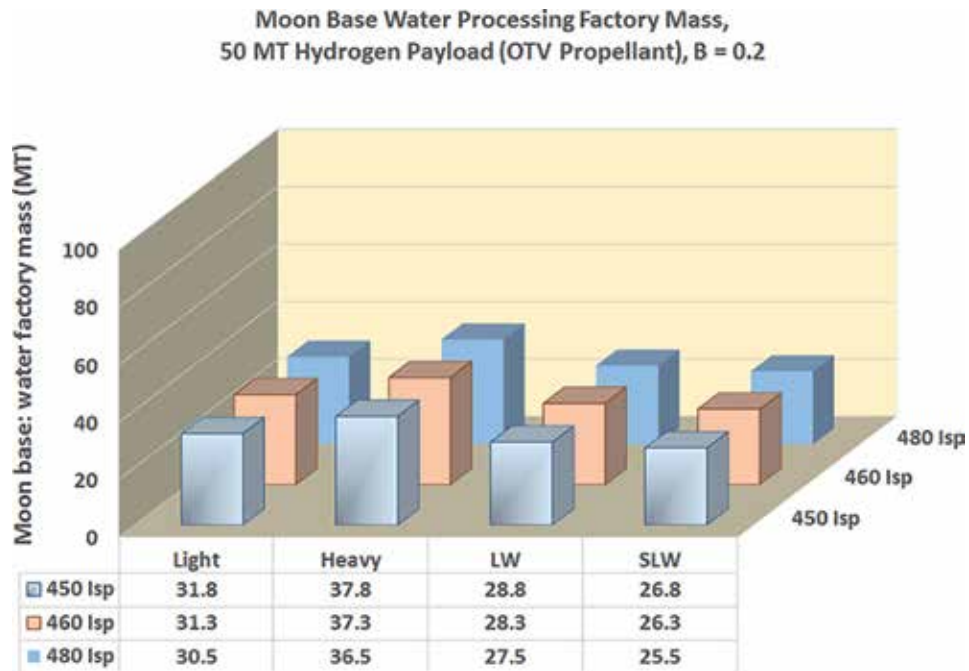
Figure 4.
Moon base factory masses, for 50 MT payload landers.

oxygen and hydrogen propellants for the science landers (with a 1 MT payloads) and 50 MT payload factory lander. Once in orbit about the centric moon, the factory lander with the 50 MT ISRU factory lands. The mining and conversion of water ice to oxygen and hydrogen for the factory lander's ascent to orbit are conducted. Additional hydrogen is created on the centric moon and that hydrogen is delivered to the orbiting OTVs. The OTVs can then be dispatched on their moon exploration flights to the other remaining moons. The factory lander will have to perform several flights to deliver the full propellant loads for the orbiting OTVs. **Figure 4** presents the estimated masses of a series of propellant factories. The factory masses are based on the lander Isp and the factory design, which is a function of the level of integration with the lander.

For example, a light propellant factory has separate tanks for lander and factory. A heavy propellant factory has separate tanks for lander and factory but has higher masses for enclosures that protect against the elements, winds, micrometeoroids, etc. Also, higher masses are included for foundations for cryogenic surfaces (creating a stable structure for the base). For a super lightweight propellant factory, propellants and all fluids are fed to and stored in lander tanks. Appendix A delineates the masses in the heavy configuration.

In **Figure 5**, the masses of the ISRU factory and the OTV propellant masses needed for the Saturn moon survey are compared. With the cases without Iapetus, six moons are surveyed. The mass of the ISRU factory is 50 MT. In all cases, the total OTV propellant load is significantly higher that the factory mass. Thus, the use of the factory can enable not only the first survey of the moons but many more. Typically, nuclear reactors have been designed for a 7-year life at full power and a 10-year overall life (operating for the last 3 years at a reduced power level). Given the typical 7-year lifetime of a space nuclear reactor [13], the number of OTV flights can be 6–7.
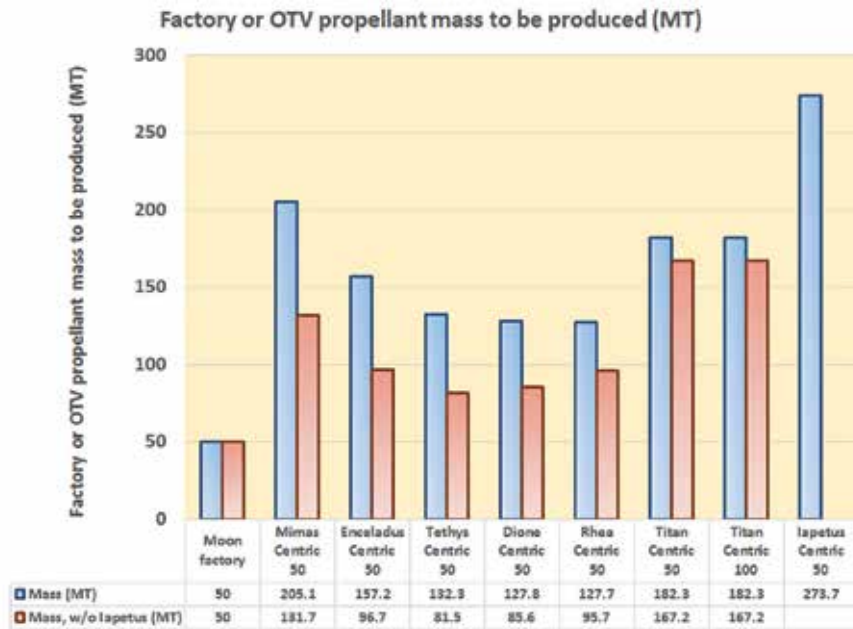
Figure 5.
Moon factory mass comparison with OTV propellants needed.

4.5 Mission scenario results and interpretations

To fully explore the moons, a fleet of OTVs and landers were conceived. One OTV and one lander would visit each moon. At the central or centric moon, a 50 MT ISRU factory is landed. The 50 MT payload includes an ISRU factory and a set of empty propellant tanks. The factory creates the propellant for all of the NEP OTVs and landers. The propellant tanks will be filled with the moon-derived ISRU propellants.

The lander was designed to bring that propellant into orbit to refuel the OTVs. The lander propellant tanks are fueled with oxygen and hydrogen. The lander then ascends to the escape conditions of the moon's orbit. Then the lander performs a rendezvous with the OTV(s) and refuels OTV(s); it may also refuel the smaller exploration landers aboard the OTV(s). The newly fueled OTV with its exploration lander completes the orbit transfer to another moon. After completing its exploration, the OTV returns to the moon with ISRU propellant factory.

An additional case for Titan with a 100 MT lander payload was included. This case was added as the lander delta-V for Titan is the highest of all of the moons; therefore, a larger propellant mass is needed for each flight. A larger lander payload case might be attractive in reducing the number of flights needed for refueling the OTVs.

An overall fleet mass of the OTVs and the landers was then estimated. The fleet consisted of one NEP OTV and lander designed to visit a specific moon. Each OTV carried a lander with a 1 MT payload. For the seven moon options, seven OTVs and seven exploration landers were sized. Each OTV was sized to operate from a central moon. As noted above, an additional lander operating from the centric moon was added to provide the ISRU refueling capability for the OTV fleet.

Using the mission delta-V values and vehicle sizing data, the following optima for moon exploration were found. In **Table 6**, the total mass of the OTV

Moon	OTV Mp (MT)	Lander Mp (MT)	Lander and OTV dry mass (MT)	Total mass (MT)
Mimas Centric 50	205.1	5.1	832.7	1,042.9
Enceladus Centric 50	157.2	9.7	811.9	978.9
Tethys Centric 50	132.3	14.4	814.8	961.4
Dione Centric 50	127.8	20.0	810.0	957.8
Rhea Centric 50	127.7	26.6	818.2	972.5
Titan Centric 50	182.3	362.6	876.0	1,420.9
Titan Centric 100	182.3	725.3	1003.5	1,911.1
Iapetus Centric 50	273.7	23.5	825.3	1,122.5

Table 6.
Total masses of the lander and OTV fleets, for moon-centric options, including seven moons.

At Saturn: Mass Required for Moon Centric Operations, 7 Moons - NEP alpha = 10 kg/kWe, NEP Isp = 5000 s, Lander Isp = 480 s, Lander Payload = 50 and 100 MT

	Mimas Centric 50	Enceladus Centric 50	Tethys Centric 50	Dione Centric 50	Rhea Centric 50	Titan Centric 50	Titan Centric 100	Iapetus Centric 50
OTV Mp (MT)	205.1	157.2	132.3	127.8	127.7	182.3	182.3	273.7
Lander Mp (MT)	5.1	9.7	14.4	20.0	26.6	362.6	725.3	23.5
Lander and OTV dry mass (MT)	832.7	811.9	814.8	810.0	818.2	876.0	1003.5	825.3
Total mass (MT)	1,042.9	978.9	961.4	957.8	972.5	1,420.9	1,911.1	1,122.5

Figure 6.
Total masses of the lander and OTV fleets, for moon-centric options, including seven moons.

and lander fleets using a central moon are shown; the minimal mass is 958 MT for the moon Dione. **Figure 6** also presents the fleet mass data. While Dione represents the minimal fleet mass, the optimum is fairly broad over a set of four moons: Enceladus, Tethys, Dione, and Rhea. After further exploration and consideration of currently imprecisely known factors (ice composition, regolith strength, ease of access to any subsurface moon oceans, etc.), an optimal moon can be selected.

Table 7 presents the same analyses, excluding Iapetus. In **Table 6**, the minimal fleet mass is found for the moon Dione. In **Table 7**, the minimal fleet mass is for the moon Tethys: the fleet mass is 785 MT. While Tethys represents the moon

Moon	OTV (MT)	Mp Lander (MT)	Mp Lander and OTV dry mass (MT)	Total mass (MT)
Mimas Centric 50	131.7	5.1	706.1	842.9
Enceladus Centric 50	96.7	9.7	685.9	792.4
Tethys Centric 50	81.5	14.4	689.2	785.2
Dione Centric 50	85.6	30.1	684.9	800.5
Rhea Centric 50	95.7	26.6	694.6	816.9
Titan Centric 50	167.2	362.6	752.3	1,282.1
Titan Centric 100	167.2	725.3	879.7	1,772.2

Table 7.
Total masses of the lander and OTV fleets, for moon-centric options, including six moons (without Iapetus).

with the minimal fleet mass, the optimum is fairly broad over a set of four moons: Enceladus, Tethys, Dione, and Rhea.

By excluding Iapetus, the total fleet mass is significantly reduced; for Dione, the fleet mass is reduced from 958 to 800 MT. Further restrictions of the moon exploration fleet (e.g., from six to four moons) may be needed to fit within the payload capacity of future interplanetary transfer vehicle (ITVs). As Iapetus is more remote than the other moons, it is possible that a separate ISRU space base may be more attractive than a centralized ISRU space base.

Due to the low gravity level of the moons, a moon-orbiting space base may be attractive. Processing control of ices in a low-gravity environment may be very difficult. It is suggested that an artificial gravity space base in orbit about the moon may be the best location of resource processing. After a series of small missions have been conducted, a large ISRU space base may be established. The base might be a refueling point for extensive exploration. The water ices from the moons would be brought to the space base for processing, to allow the refueling of the landers and the NEP OTVs.

5. The far future: human Saturn missions with nuclear pulse propulsion (NPP)

Historical analyses of human missions to the outer planets have included many nuclear propulsion conceptual designs. Nuclear pulse propulsion was investigated and was considered a practical alternative to any chemical propulsion options. The round-trip impulsive delta-V for such missions was approximately 60 km/s [34, 38–41].

Human missions to Jupiter and Saturn were suggested in the 1960s. Large-scale exploration missions with many astronauts were planned. The primary propulsion system considered was nuclear pulse propulsion. Many small nuclear packages were exploded behind the vehicle, propelling it onto a high-thrust trajectory. For a human Jupiter or Saturn mission, the delta-V was approximately 60 km/s. While the round-trip Jupiter missions were designed to orbit Callisto, at Saturn, Titan was selected. Titan is the largest moon of Saturn, the delta-V to land there is high, 2.2 km/s, and the escape velocity is 3.17 km/s. These values represent an all propulsive landing on Titan and include a 20% delta-V penalty for gravity losses [23]. Such a propulsive delta-V was selected to make the comparisons with the other

Human Saturn Missions, NPP, four maneuvers, Isp = 3,000 seconds, 358 MT pusher plate, B = 0.01

	1	2	3	4	5
Delta-V (km/s)	60	80	90	100	120
LEO mass (MT)	5,916	11,819	16,719	23,667	47,524
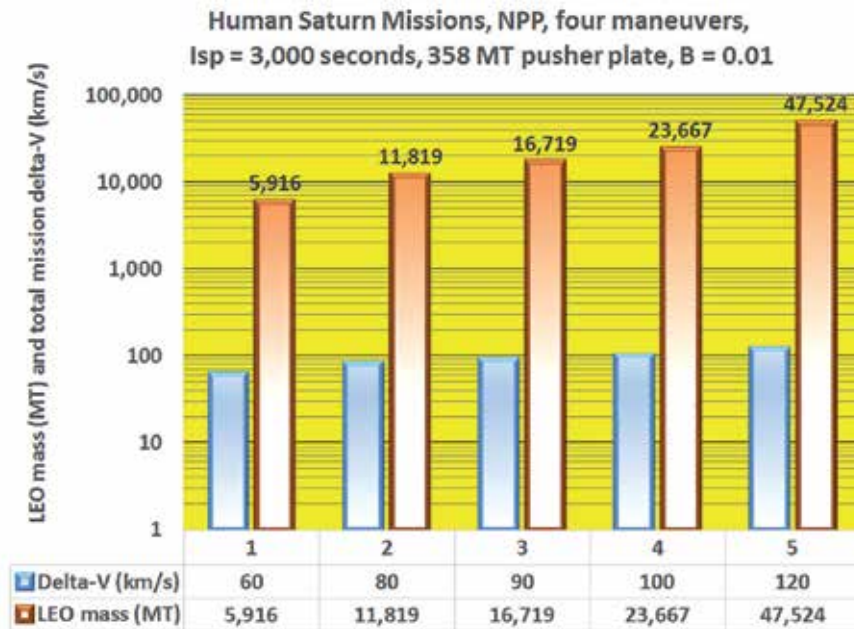
Figure 7.
Saturn NPP sizing and mission data, B = 0.01 Mp [23].

moon landers as consistent as possible. If a lander were to be used for many flights, repacking parachutes or reoutfitting a robotic lander with additional parachutes on orbit may be cumbersome.

Figure 7 shows the mass of the Saturn missions for a range of delta-V of 60–120 km/s. While the 60 km/s missions represent a fast mission to Saturn (approximately 250–500 days), a fast mission in both directions may require 120 km/s. The vehicle mass for the 120 km/s missions is over 47,000 MT, while the 60 km/s mission requires less than 6000 MT.

In Ref. [23], using ISRU for refueling a fast Saturn mission was analyzed. Saturn's atmosphere was considered a likely source of the nuclear fuels: helium 3 and deuterium. After analyses of the ISRU transportation systems, it was found that Uranus was a more likely atmospheric fuel source. The complexity of moving OTVs from low Saturn orbit to an assembly point (such a Titan) and the trip time for the low-thrust transfers (for a round-trip delta-V of over 94 km/s) were very prohibitive. With the Uranus option, the nuclear fuels were mining and sent to Titan. The round-trip OTV delta-V for lifting the mined fuels to a moon of Uranus was approximately 32 km/s. While the delta-V for mining transportation is lower, the need for an interplanetary transfer vehicle (ITV) is apparent. A relatively low-energy Uranus to Saturn transfer is possible with an NEP ITV. While the ISRU option for the fast Saturn mission is attractive, the time for gathering the nuclear fuels may require 10 years of mining operations.

6. Concluding remarks

Saturn and its moon have always been fascinating. Ever since Galileo Galilei noted in his early telescopic observations that "Saturn has ears," the excitement

for Saturn exploration has been strong. Both Saturn and its moons are rich with resources: hydrogen and helium in the planet's atmosphere and ices on the moons. Using the resources of the outer planet moons, new options for exploration are possible. Multiple moons can be visited and explored. High-power OTV with nuclear power can reveal the nature of the ices and regolith of the moons.

Detailed exploration of the major moons can be completed with a set of small chemical propulsion moon landers and nuclear electric orbital transfer vehicles. A series of such OTV and landers showed several optimal locations for conducting a moon survey. Dione was an optimal location for the minimization of the OTV and lander fleet mass. A central moon location allowed a large ISRU factory to fuel many OTV and exploration lander flights.

Far future human exploration of the Saturn system may employ very high-energy nuclear propulsion systems. Nuclear pulse propulsion vehicles may allow fast transfers to Saturn and the delivery of robotic exploration vehicles and human explorers. Using ISRU for refueling a fast Saturn mission was analyzed. Saturn's atmosphere was considered a likely source of nuclear fuels: helium 3 and deuterium. After analyses of the ISRU transportation systems, it was found that Uranus was a more likely atmospheric fuel source. There are numerous benefits of ISRU in Saturn and Uranus systems. With ISRU, our exploration options are nearly endless, and the abilities to uncover the secrets of Saturn moons are awaiting our scientific investments.

Nomenclature

3He	helium 3
4He	helium (or helium 4)
AMOSS	atmospheric mining in the outer solar system
ASC	aerospacecraft
CC	closed cycle
delta-V	change in velocity (km/s)
GCR	gas core rocket
GTOW	gross takeoff weight
H_2	hydrogen
He	helium 4
ISRU	in situ resource utilization
Isp	specific impulse (s)
K	kelvin
kWe	kilowatts of electric power
LEO	low Earth orbit
MT	metric tons
MWe	megawatt electric (power level)
NEP	nuclear electric propulsion
NPP	nuclear pulse propulsion
NTP	nuclear thermal propulsion
NTR	nuclear thermal rocket
OC	open cycle
O_2	oxygen
PPB	parts per billion
PSC	permanently shadowed craters
PSR	permanently shadowed regions

A. Appendix A: moon base factory masses

		450	460	480	
		Lander MP	Lander MP	Lander MP	
Propellant factory for moons: The factory will take the raw materials from the outer planet moon's surface, lake(s), or ocean(s) and process them into oxygen and hydrogen for the chemical propulsion lander(s). Additional liquid hydrogen will also be produced as the fuel for the NEP OTVs (hydrogen MPD or PIT propulsion). Water may have to be processed from regolith or and liquid reservoir (lake(s), or ocean(s)).		B	B	B	B, H2
	Heavy Propellant factory.	0.2	0.2	0.2	0.1
	Mass, estimated (MT)	Mp (MT)	Mp (MT)	Mp (MT)	H2 mass (MT)
Subsystem list - overview:		26.33	25.58	24.22	50
Factory machines.	2	2	2	2	
Enclosures, protection against the elements, winds, micrometeoroids, etc.	2	2	2	2	
Foundations for cryogenic surfaces (creating a stable structure for the base).	0	0	0	0	
Buoyancy systems, if floating on cryogenic lakes, oceans, etc.	0	0	0	0	
Safety systems.	1	1	1	1	
Drilling systems (potentially deep drilling, for salt water oceans).	0	0	0	0	
Melting – heating systems (for permafrost, cryogenic ices, extracting water from water ice-regolith mix, etc.).	2	2	2	2	
Liquid feed systems.	1	5.27	5.12	4.84	
Gaseous feed systems.	1	1	1	1	
Liquefaction systems.	2	2	2	2	
Liquid storage: cryogenic.	2	5.27	5.12	4.84	5
Liquid storage: non-cryogenic.	2	2	2	2	
Gaseous storage.	2	2	2	2	
And:					
Liquid oxygen and liquid hydrogen storage.	1	5.27	5.12	4.84	
Liquid oxygen and liquid hydrogen transfer to landers.	1	1	1	1	
And:					
Liquid hydrogen - Payload transportation to landers.	1	1	1	1	
Liquid hydrogen - Payload loading onto landers.	1	1	1	1	
Subtotal (MT)	21	32.80	32.35	31.53	5
Total (MT), factory and payload storage		37.80	37.35	36.53	

Author details

Bryan Palaszewski
NASA John H. Glenn Research Center at Lewis Field, Cleveland, OH, USA

*Address all correspondence to: bryan.a.palaszewski@nasa.gov

IntechOpen

References

[1] Rosenberg SD, Guter GA, Miller FE, Beegle RL Jr. Research on processes for utilization of lunar resources. Aerojet General; Contract NAS 7-225, Report No. 3049 (Final), August 1965

[2] Palaszewski B, Frisbee R. Advanced propulsion for the Mars Rover Sample Return Mission, AIAA 1988-2900, July 1988

[3] Stancati ML, Jacobs MK, Cole KJ, Collins JT. In situ propellant production: Alternatives for mars exploration. Science Applications International Corporation, Report No. SAIC-91/1052, Study No. SAIC 1-120-631-S28, NASA CR 187192, Contract NAS3-25809, October 1991

[4] John S. Lewis, Mining the Sky: Untold Riches from the Asteroids, Comets, and Planets. Lebanon, Indiana: Perseus Publishing; 1997

[5] Linne Diane L. Overview of NASA technology development for in-situ resource utilization (ISRU). In: 68th International Astronautical Congress; 25-29 September 2017

[6] Sanders GB. Overview of past lunar in situ resource utilization (ISRU) development by NASA. In: European Space Agency (ESA) Workshop: Towards the Use of Lunar Resources; 3-5 July 2018; Noordwijk, Netherlands; 03 July 2018

[7] Hinterman E. Simulating oxygen production on Mars for MOXIE (Mars Oxygen In-Situ Resource Utilization Experiment). In: IAC-18, A5,2, 9 x 42905, 2018

[8] Kornuta D. Commercial Lunar Propellant Architecture—A Collaborative Study of Lunar Propellant Production [Internet]. 2018. Available from: http://www.isruinfo.com/

[9] Ash R et al. Outer planet satellite return missions using in situ propellant production. Acta Astronautica. 1981;**8**(5-6):511-526

[10] Adams RB et al. Conceptual design of in-space vehicles for human exploration of the outer planets. NASA Technical Publication TP—2003-212691, November 2003

[11] Palaszewski B. Atmospheric mining in the outer solar system: Resource capturing, storage, and utilization. AIAA 2012-3742, July 2012

[12] Palaszewski B. Atmospheric mining in the outer solar system: Issues and challenges for mining vehicle propulsion. AIAA 2011-6041, August 2011

[13] Palaszewski B. Atmospheric mining in the outer solar system: Outer planet in-space bases and moon bases for resource processing. AIAA 2017-4937, July 2017

[14] Hussmann H, Sohl F, Spohn T. Subsurface oceans and deep interiors of medium-sized outer planet satellites and large trans-neptunian objects. Icarus. 2006;**185**:258-273

[15] Spencer JR, Howett CJA, Verbiscer AJ, Hurford TA, Gorius NJP. High resolution observations of active and passive thermal emission from Enceladus' south pole in 2015: The closest and the coldest. In: 47th Lunar and Planetary Science Conference; Abstract 2860; 2016

[16] Zahnle KJ, Korycansky DG, Nixon CA. Big impacts and transient oceans on titan. In: Workshop on the Habitability of Icy worlds; Abstract 4063; 2014

[17] Shina K, Kumarb R, Udachina KA, Alavia S, Ripmeestera JA. Ammonia

clathrate hydrates as new solid phases for Titan, Enceladus, and other planetary systems. Proceedings of the National Academy of Sciences of the United States of America. 2012;**109**(37):14785-14790

[18] Ostro SJ, West RD, Janssen MA, Lorenz RD, et al. Cassini RADAR observations of Enceladus, Tethys, Dione, Rhea, Iapetus, Hyperion, and Phoebe. Icarus. 2006;**183**:479-490

[19] National Space Science Data Center. Available form: nssdc.gsfc.nasa.gov

[20] Buffett BA. Clathrate hydrates. Annual Review of Earth and Planetary Sciences. 2000;**28**:477-507. Copyright q 2000 by Annual Reviews

[21] Chenette DL, Stone EC. The Mimas Ghost revisited: An analysis of the electron flux and electron microsignatures observed in the vicinity of Mimas at Saturn. The Aerospace Corporation, Aerospace Report No. ATR-83(9990)-3, 8 June 1983

[22] Tajeddine R, Rambaux N, Lainey V, Charnoz S, Richard A, Rivoldini A, et al. Constraints on Mimas' interior from Cassini ISS libration measurements. Science. 2014;**346**(6207):322-324

[23] Lainey V et al. New constraints on Saturn's interior from Cassini astrometric data. Icarus. 2017;**281**:286-296

[24] Verbiscer A, French R, McGhee C. Hubble space telescope photometry of Mimas, Enceladus, Tethys, Dione, and Rhea. In: Solar System Remote Sensing Symposium; 2002

[25] Howett C, Spencer JR, Pearl JC, Hurford TA, Segura M, Cassini Cirs Team. Unexpected and unexplained surface temperature variations on Mimas. In: American Geophysical Union, Fall Meeting 2010; Abstract id. P31B-1531, December 2010

[26] Clark RN Mosher JA, Cruikshank DP, Filacchione G, Baines KH, Nicholson PD, Sotin C, Buratti BJ, Brown RH. Mimas between 0.35-5.1 microns from Cassini VIMS observations. In: 42nd Lunar and Planetary Science Conference; 2011

[27] Squyres SW, Reynolds RT. Geologic studies of outer solar system satellites: Iapetus and Europa. In: NASA. Washington Reports of Planetary Geology Program; (SEE N84-23431 13-91); April 1984. pp. 41-43

[28] Mosqueira I, Estrada PR. On the origin of the saturnian satellite system: Did iapetus form in-situ? In: Lunar and Planetary Science XXXVI; 2005

[29] Hendrix AR, Hansen CJ. Iapetus and phoebe as measured by the cassini uvis. In: Lunar and Planetary Science XXXVI; 2005

[30] Tosi F, Turrini D, Coradini A, Filacchione G, the VIMS Team. Probing the origin of the dark material on Iapetus. Monthly Notices of the Royal Astronomical Society. 2010;**403**:1113-1130

[31] Palaszewski B. "Solar system exploration augmented by in-situ resource utilization: Lunar base issues," Chapter in Lunar Science Book, IntechOpen, 2019

[32] Palaszewski B. Atmospheric mining in the outer solar system: Aerial vehicle mission and design issues. AIAA 2015-4078, July 2015

[33] Palaszewski B. Atmospheric mining in the outer solar system: Orbital transfer vehicles and outer planet moon base options. AIAA 2016-4889, July 2016

[34] Palaszewski B. Solar system exploration augmented by in-situ

resource utilization: Mercury and Saturn propulsion investigations. AIAA 2016-0717, January 2016

[35] Palaszewski B. Metallized propellants for the human exploration of Mars. AIAA Journal of Propulsion and Power. 1992;**8**(6):1192-1199. NASA-Lewis Research Center, NASA TP-3062, Case For Mars IV Conference; Boulder, CO; 4-8 June 1990

[36] Bensky M. Propulsion requirements for soft landing in extraterrestrial environments. Rocketdyne, NAS7-124, NASA CR-55088, February 1963

[37] Palaszewski B. Lunar missions using advanced chemical propulsion: System design issues. AIAA Journal of Spacecraft and Rockets. 1994;**31**(3): 458-465. NASA-Lewis Research Center, NASA TP-3065, AIAA 90-2341, 26th AIAA/ASME/SAE Joint Propulsion Conference; Orlando, FL; July 1990

[38] Interplanetary maneuvers in manned helionautical missions. (Ehricke, 1965) AIAA 1965-695

[39] Ehricke KA. Solar transportation In: 4th Goddard Memorial Symposium; Am. Astronautical Soc.; Washington, DC; 15-16 March 1966

[40] Teng O, LaRouche Youth Movement, Freeman M. A grand vision of man's role in colonizing the universe. Book review; Krafft Ehricke's moon: The extraterrestrial imperative; Technology Editor of Executive Intelligence Review; 2009. Available from: http://www.21stcenturysciencetech.com/Articles_2009/Summer-2009/Extraterrestrial_Imperative.pdf

[41] Schmidt GR, Bonometti JA, Irvine CA. Project Orion and future prospects for nuclear pulse propulsion. Journal of Propulsion and Power. 2002;**18**(3):497-504

Chapter 4

Space Access for Future Planetary Science Missions

Colin Sydney Coleman

Abstract

Planetary science demands increasingly elaborate experiments, with the result that mission objectives are often limited by space access capability. The orbital skyhook is a momentum transfer device that has been proposed as an alternate launch system. It is an extended orbital structure that rotates to allow access by a low speed suborbital vehicle. After docking, the vehicle gains momentum from the skyhook and is accelerated to orbital velocity, after which the skyhook energy must be replenished. The construction of an orbital skyhook is shown to be feasible with current materials. It is a fully reusable launch system with very high propellant efficiency and could provide the launch capability needed for future planetary science missions.

1. Introduction

Proposals for a momentum transfer based launch system are not new. Konstantin Tsiolkovsky, credited with the concept of multi-stage rocket vehicles, also proposed the orbital tower. Much later Yuri Artsutanov inverted this idea to suggest a geostationary satellite with a counterweight and a tether extending to the Earth's surface. This so called 'space elevator' was first published in 1960 in Komsomolskaya Pravda and later discovered independently in the US when the term 'skyhook' was coined [1]. The structure was shown to be stable against the effects of lunar tidal forces and payload motions, and functions by extracting energy from Earth rotation [2]. The problem is that no known material has sufficient strength to construct a space elevator in Earth orbit.

Difficulties with the space elevator led to the proposal of the asynchronous orbital skyhook [3]. (The original concept was credited to John McCarthy at Stanford.) This is an extended orbital structure that rotates so that each end periodically comes to a low altitude and velocity, at which instants the system is easy to access. Initial studies advocated configurations that place a low demand on the tether material properties, as this was thought to be the principal challenge. To replace energy lost during launch it was proposed that the skyhook be used to return a similar quantity of material from orbit to Earth.

Detailed studies of the asynchronous skyhook [4, 5] addressed engineering aspects of the tether and docking mechanism. They proposed a set of configurations in which access is provided by a hypersonic vehicle operating at a speed of at least

3.1 km/s (Mach 10). This high speed of the access vehicle reduces the skyhook rotation rate and so places less stress on the tether material.

Hypersonic flight technology is not yet capable of providing routine access to the high Mach number regime. By contrast, several reusable vehicles are available that provide access to suborbital flight trajectories using combinations of air-breathing and rocket propulsion [6, 7]. High strength fiber technology has also made substantial progress with the incorporation of carbon nanotubes into the molecular structure [8]. This suggests a need to review the orbital skyhook concept with a focus on configurations that allow low speed access. It is also necessary to explore different approaches to energy replenishment that do not require access to a repository of orbiting material.

Section 2 reviews the skyhook concept and estimates the parameters of a practical launch system. Expressions for the skyhook mass properties are obtained in Section 3 for the case where centripetal force is the dominant source of tension. The dynamics is modeled in Section 4 assuming the structure remains linear, with the tether mass properties represented by a compact object at the mass centroid. Electric propulsion is proposed as a mechanism for energy replenishment in Section 5, and the feasibility of supplying propellant for the thrusters is explored. Section 6 describes the advantages of a skyhook launch system for future planetary science missions, and Section 7 summarizes the main results.

2. Concept description

An orbital skyhook launch system involves three phases, each exploiting a different physical process. It begins with the delivery of a payload by suborbital vehicle. Docking occurs at one of the skyhook endpoints when it is near minimum altitude and velocity. The suborbital vehicle is required to attain only a small fraction of the energy needed for orbit, and does not need to operate in a hypersonic flight regime. It can therefore employ mature airframe and propulsion technologies, making it easier to design for efficiency and reusability.

The second phase is momentum transfer from the skyhook to the payload [9]. After docking the payload gains energy as the skyhook rotates, reaching a maximum after half a cycle. If the payload is not released energy transfers back to the skyhook in the second half of the cycle as it returns to minimum energy. By selecting when the payload is released, it can be placed into an elliptical orbit or on an escape trajectory. Note that if the payload is released at a subsequent minimum energy point, the skyhook energy and orbit are left unaffected. This means the vehicle is transported around the Earth at orbital velocity, with the only energy cost being that of gaining access to the skyhook.

In the third phase energy drawn from the skyhook during launch must be replenished. If the payload mass is small relative to the total system mass, the orbital perturbation is also small. In this case the structure remains above the atmosphere through subsequent rotations, and energy replenishment may occur over an extended period. Electric propulsion is proposed for this purpose. It provides a small thrust with a large specific impulse, and therefore high propellant efficiency. Propellant can be delivered with the payload to supply thrusters at the skyhook endpoints, but it will be shown that a better approach is to apply thrust at the skyhook mass centroid.

Of interest here are skyhook configurations that offer low speed access. Ideally the endpoint speed should match the orbital velocity relative to Earth's surface. In addition, acceleration during launch must not be excessive. For a skyhook in a circular equatorial orbit with radius R and orbital frequency Ω the endpoint ground track speed and acceleration are given by:

$$v_M = R\Omega - L\omega - 465 \tag{1}$$

$$a_M = R\Omega^2 \left[(1 - L/R)^{-2} - 1 \right] + L\omega^2 \tag{2}$$

Here L and ω are the skyhook half-length and rotation frequency, and Eq. 2 includes the acceleration components due to gravity, orbital velocity and skyhook rotation.

Specifying the endpoint velocity and acceleration yields two implicit equations for the skyhook parameters. With a nominal orbital radius of 8000 km the skyhook length is small enough to apply the limit $L \ll R$. Then for a minimum energy state at zero velocity and 40 m/s^2 acceleration, the skyhook parameters are $L = 1090$ km and $\omega = 0.006 \text{s}^{-1}$. This system can be accessed at zero velocity by a vehicle capable of ascending to an altitude of 532 km. Moreover, the maximum acceleration experienced during launch is similar to that of a conventional launch vehicle.

One of the skyhook endpoints is at minimum energy when the structure is oriented radially. This state occurs with a period $\tau = \pi/(\omega - \Omega)$ corresponding to a ground track distance of 3176 km around the equator. The orbital parameters could be adjusted so this distance is an exact fraction of the equatorial circumference, in which case the minimum energy states occur above fixed points on the equator. These locations are natural sites at which to establish bases to operate the suborbital access vehicles.

3. Mass properties

The skyhook configurations of interest here have an endpoint speed near orbital velocity to allow access at low energy. The high rotation rate means tension is mainly due to centripetal force, with the field gradient contribution being negligible.

Consider a symmetric skyhook comprising two equal masses m connected by a massive tether of length $2L$ and define the origin at the center. The tether cross-section is $a(r)$ and the tether material has uniform density ρ and ultimate tensile strength T. For a skyhook with rotation frequency ω the tension σ at radius r obeys:

$$\sigma'(r) = -\rho\omega^2 r a(r) \tag{3}$$

Substituting $a(r) = \sigma(r)/T$ and noting that $a(L) = mL\omega^2/T$ this equation can be solved for the tether cross-section:

$$a(r) = \frac{mL\omega^2}{T} \exp\left[\chi^2 \left\{ 1 - \left(\frac{r}{L}\right)^2 \right\} \right] \tag{4}$$

Here $\chi^2 = \rho\omega^2 L^2/2T$ is a dimensionless parameter characterizing the skyhook. By symmetry the mass centroid is at the origin. This structure may be generalized to describe a set of asymmetric configurations with unequal end masses at different distances from the centroid. The symmetric configuration has the benefit of offering two opportunities to access the skyhook in each rotation cycle, but asymmetric configurations allow access to a greater variety of launch trajectories.

The tether mass M_T and moment of inertia I_T are given by:

$$M_T = 2\rho \int_0^L a(r)dr \tag{5}$$

$$I_T = 2\rho \int_0^L a(r) r^2 dr \tag{6}$$

Evaluating the integrals and simplifying:

$$M_T/m = 2\sqrt{\pi}\, \chi \exp\left[\chi^2\right] \mathrm{erf}(\chi) \tag{7}$$

$$I_T/mL^2 = \sqrt{\pi}\chi^{-1} \exp\left[\chi^2\right] \mathrm{erf}(\chi) - 2 \tag{8}$$

The limit $\chi \to 0$ represents a material of infinite strength, in which case the tether mass and moment of inertia vanish. Adding the contributions of the two end masses leads to expressions for the mass properties of the entire skyhook:

$$M/m = 2\sqrt{\pi}\, \chi \exp\left[\chi^2\right] \mathrm{erf}(\chi) + 2 \tag{9}$$

$$I/mL^2 = \sqrt{\pi}\, \chi^{-1} \exp\left[\chi^2\right] \mathrm{erf}(\chi) \tag{10}$$

These expressions for the skyhook mass properties indicate the dependence on tether material properties, and provide key parameters for dynamical modeling.

An important feature of a tether is the taper factor, the ratio of maximum to minimum cross-section area. A tether constructed from low strength material has a large taper factor, indicating its impracticality. The nominal skyhook described above with a carbon fiber tether has a taper factor of 237, in which case the diameter at the centroid is about 15 times that the end points. If the tether had the properties of carbon nanotubes the taper factor reduces to 3.3. The properties of any future tether material are likely to fall within these bounds.

Table 1 indicates the mass properties of the nominal skyhook for several tether materials. Notionally high strength materials like steel and diamond are excluded by the very large taper factor. Aramid fibers like Kevlar are possible but the total mass is large. The strongest carbon fiber offers a solution with a skyhook mass about 4600 times the endpoint mass. If materials with still greater tensile strength become available, such as by incorporating carbon nanotubes or colossal carbon tubes into the tether material, the taper factor and skyhook mass can be much smaller.

For the skyhook configuration described here the endpoint mass is regarded as the maximum payload capability. This assumes the endpoint mass may be replaced by a docking mechanism of negligible mass to capture the payload. Engineering margins have not been included in this analysis, but the nominal configuration is a

Material	Density (kg/m^3)	Strength (MPa)	χ^2	Taper Factor	Mass (M_T/m)	Moment (I_T/mL^2)
Steel 2800	8000	2693	67.7	1.2×10^{25}	2.9×10^{27}	3.1×10^{23}
Diamond	3500	2800	26.7	4.1×10^{11}	3.9×10^{13}	2.7×10^{10}
Aramid fiber	1440	3757	8.2	3629	1.05×10^5	783.4
Zylon (PBO)	1560	5800	5.75	315	6421	96.1
Carbon fiber (T1100S)	1790	7000	5.47	237	4596	75.8
Carbon nanotube	1340	63,000	0.45	1.58	5.46	5.06
Colossal carbon tube	116	7000	0.35	1.43	1.70	5.93

Table 1.
Tether mass properties for various materials (from Eqs. (4), (7) and (8)).

'worst case' in the sense that skyhook rotation is specified to allow access at zero velocity relative to the Earth. If the access vehicle provides a horizontal velocity component the rotation rate is smaller, in which case the taper factor and skyhook mass are also decreased.

4. Equations of motion

Skyhook length is a significant factor in the dynamics because field strength is not uniform across the structure. This differs from most problems in astrodynamics where the object of interest is small compared to the field gradient length scale, or the system can be simplified by assuming spherical symmetry.

Here the skyhook is assumed to behave as a rigid body, kept in tension by the rotation and experiencing no stretching or bending. The validity of these assumptions depends on the tether material properties, but they are sufficient for the present purpose. The structure is expected to remain linear due to the large centripetal restoring force that counters any bending.

The equations of motion of a rigid body are typically obtained by a Lagrangian method using the mass properties. This formulation ignores the field gradient effect, which is important for skyhook dynamics. To see this note that the skyhook structure experiences a moment due to the two arms being subject to different field strengths according to their proximity to Earth. If the skyhook were treated as a single compact object this behavior would not be represented.

The skyhook system is modeled here as three objects connected by tethers of fixed length L as illustrated in **Figure 1**. The central object has the mass properties of the tethers as calculated above. This formulation represents the physical extent of the skyhook in a non-uniform field. It is also a good approximation for the mass distribution of the tether if it has a significant taper factor, in which case much of the mass is concentrated near the centroid. Based on these considerations a Newtonian formulation is used for the analysis.

The system state is described by a six element vector comprising the skyhook centroid location $r = (r, \theta)$ and orientation angle φ and their derivatives. The endpoint locations are specified by the vectors r_1 and r_2 which are functions of the state
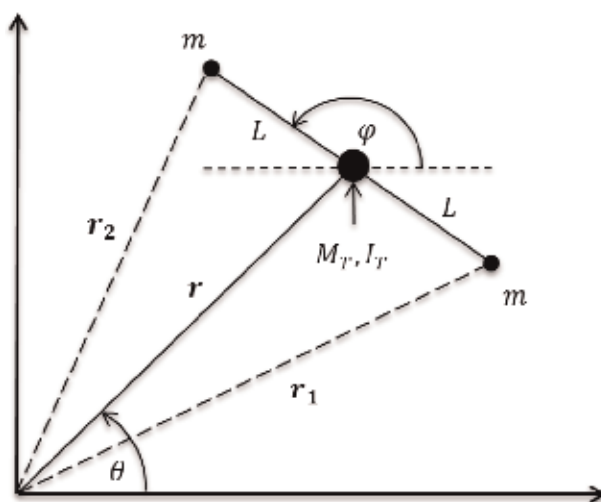

Figure 1.
Skyhook geometry with the tether mass and moment of inertia represented by a compact object at the mass centroid.

vector and may be written as follows where $\hat{\boldsymbol{t}} = (\cos\varphi, \sin\varphi)$ is the skyhook orientation unit vector:

$$r_{1,2} = \boldsymbol{r} \mp L\hat{\boldsymbol{t}} \tag{11}$$

The gravitational force on each mass is projected through the centroid to obtain the net radial and azimuthal forces, and onto the normal for the torque:

$$F_r = -\left(\frac{GM_E}{r_1^2}m\right)\hat{r}_1.\hat{\boldsymbol{r}} - \left(\frac{GM_E}{r_2^2}m\right)\hat{r}_2.\hat{\boldsymbol{r}} - \left(\frac{GM_E}{r^2}M_T\right) \tag{12}$$

$$F_\theta = -\left(\frac{GM_E}{r_1^2}m\right)\hat{r}_1.\hat{\boldsymbol{\theta}} - \left(\frac{GM_E}{r_2^2}m\right)\hat{r}_2.\hat{\boldsymbol{\theta}} \tag{13}$$

$$\tau = -\left(\frac{GM_E}{r_1^2}m\right)L\,\hat{r}_1.\hat{\boldsymbol{t}}' + \left(\frac{GM_E}{r_2^2}m\right)L\hat{r}_2.\hat{\boldsymbol{t}}' \tag{14}$$

Here $\hat{\boldsymbol{t}}' = (\sin\varphi, -\cos\varphi)$ is a unit vector normal to the skyhook. In circular polar co-ordinates the acceleration is:

$$\ddot{\boldsymbol{r}} = (\ddot{r} - r\dot{\theta}^2)\hat{r} + (r\ddot{\theta} + 2\dot{r}\dot{\theta})\hat{\theta} \tag{15}$$

The skyhook equations of motion are then:

$$\ddot{r} - r\dot{\theta}^2 = F_r/(2m + M_T) \tag{16}$$

$$r\ddot{\theta} + 2\dot{r}\dot{\theta} = F_\theta/(2m + M_T) \tag{17}$$

$$\ddot{\varphi} = \tau/I = \tau/mL^2\left\{\sqrt{\pi}\,\chi^{-1}\exp\left[\chi^2\right]\mathrm{erf}(\chi)\right\} \tag{18}$$

Evaluating the vector dot products and re-arranging:

$$\ddot{r} = r\dot{\theta}^2 - \frac{GM_Em}{2m + M_T}\frac{1}{2r}\left\{\left(\frac{1}{r_1} + \frac{1}{r_2}\right) + \left(\frac{r_1^3 + r_2^3}{r_1^2 r_2^2}\right)\cos(\theta_1 - \theta_2) + \frac{2}{r}\frac{M_T}{m}\right\} \tag{19}$$

$$\ddot{\theta} = -\frac{2\dot{r}\dot{\theta}}{r} + \frac{GM_Em}{2m + M_T}\frac{1}{2r^2}\left(\frac{r_1^3 - r_2^3}{r_1^2 r_2^2}\right)\sin(\theta_1 - \theta_2) \tag{20}$$

$$\ddot{\varphi} = -\frac{GM_Em}{2I}\left(\frac{r_1^3 - r_2^3}{r_1^2 r_2^2}\right)\sin(\theta_1 - \theta_2) \tag{21}$$

The skyhook trajectory was obtained by numerical solution of these equations of motion for the nominal parameters. The endpoint altitude and ground track speed are shown in **Figure 2**. Note that the minimum energy point occurs at zero ground track speed at an altitude of 532 km. The specific energy of a stationary object at this altitude is about 5% of one in orbit. The configuration could be altered to allow access at a lower altitude, but it may then incur an unacceptable risk of collision with satellites in low Earth orbit.

During launch momentum transfers from the skyhook to the payload, perturbing the skyhook orbit into an ellipse. This perturbation is small if the skyhook mass is much greater than the payload mass, as is true for most tether materials. If the tether material is sufficiently strong the skyhook mass can be small enough for the orbital perturbation to be significant. This can be overcome by placing ballast mass at the centroid.

Endpoint Trajectory
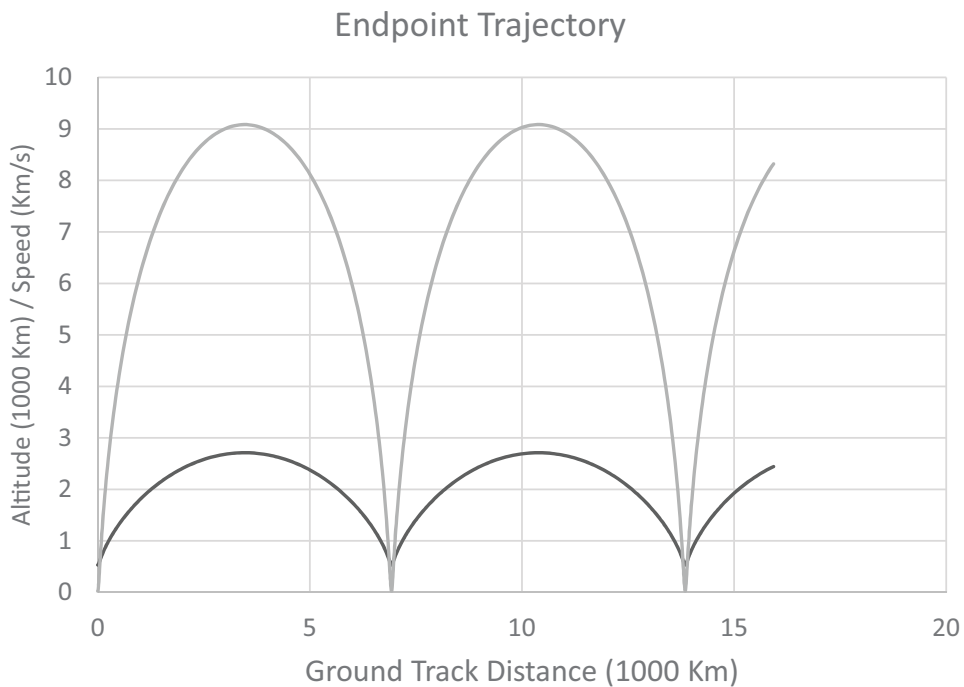
Figure 2.
Altitude (dark) and ground track speed (light) of a skyhook endpoint.

5. Energy replenishment

After launch it is necessary to replenish the skyhook energy and circularize the orbit. If the orbital eccentricity is small there is no interaction between the skyhook and the atmosphere, so this may occur over many orbits. Electric thrusters are proposed as a suitable technology for maintaining the skyhook orbit. They produce thrust with a high specific impulse, and therefore utilize propellant very efficiently.

The preferred location to apply thrust is the skyhook centroid. A force at this point maximizes energy transfer, the rate of work being the product of the thrust and orbital velocity V_0. The skyhook is also very robust at the centroid, and with a local acceleration near zero it is the optimal location for solar arrays to power the thrusters. Note that mass at the centroid does not affect the skyhook structure or energy transfer rate. This means the propulsion system mass and efficiency is of no concern. The key thruster performance characteristics are the efflux velocity and mass flow rate, which together determine the propellant quantity and time needed to achieve energy replenishment.

Electric propulsion has been developed for tasks that require a small thrust with high specific impulse. Examples include orbital transfer and deep space missions, for which ion thrusters are the preferred technology. Energy replenishment requires a high specific impulse and sufficient thrust to limit the replenishment time. A magnetoplasmadynamic (MPD) motor is best suited for this purpose. MPD thruster technology is developmental, but their performance can be inferred from experimental demonstrators.

An MPD thruster creates an electric current in plasma in the presence of a magnetic field. The field may be generated externally by coils or intrinsically by the current itself. In either case Lorentz force acts on the plasma and expels it at high velocity. Laboratory MPD thrusters have demonstrated 5 N of thrust with a mass
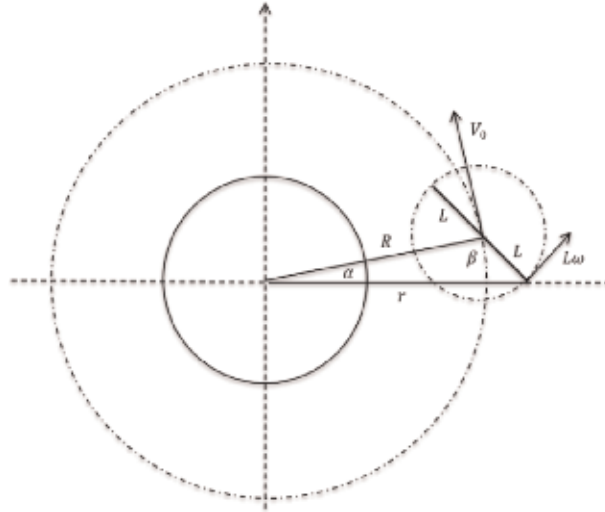
Figure 3.
Skyhook orbital geometry and payload velocity at detachment.

flow rate of 60 mg/s [10]. The MPD thruster is a compact and robust device, but it operates most efficiently at high power levels in the order of 1 MW. It is estimated that a practical MPD thruster could achieve a thrust of 2.5–25 N with an efflux velocity of 15–60 km/s [11].

A thruster with efflux velocity V_E and mass flow rate $\dot{m}$ acting at the centroid can replenish the launch energy $E_L = m_0 V_0^2/2$ for a payload m_0 in a period T_R given by:

$$T_R = E_L/\dot{E} = m_o V_0/2V_E\dot{m} = m_P/\dot{m} \tag{22}$$

The ratio $m_P/m_o = V_0/2V_E$ is the fraction of payload mass that must be reserved for propellant to replenish launch energy. For an efflux velocity of 50 km/s this ratio is 0.07. This means the amount of propellant needed to replenish launch energy is only 7% of the payload mass. With a realistic mass flow rate of 0.4 g/s the time needed to replenish the energy used to launch a 1000 kg payload is about 2 days. This can obviously be reduced by operating several such thrusters in parallel.

The quantity of propellant needed for energy replenishment is much smaller than the payload mass, but it must be delivered to the skyhook centroid. This can be achieved by having the skyhook launch a transport vehicle into an elliptical orbit, after which it uses conventional propulsion systems to perform an orbital transfer maneuver and rendezvous with the centroid. The analysis concludes by demonstrating that it is possible to deliver propellant efficiently to the skyhook centroid.

Skyhook endpoint kinematics is characterized by near uniform circular motion for both the orbit and the rotation. The velocity may be determined by adding the two rotational velocities as illustrated in **Figure 3**.

$$v_r = -V_0 \sin(\alpha) + L\omega \sin(\alpha + \beta) \tag{23}$$
$$v_\theta = V_0 \cos(\alpha) - L\omega \cos(\alpha + \beta) \tag{24}$$

The triangle in the figure is fully specified, so all angles can be expressed in terms of the skyhook parameters and endpoint radial coordinate. If the payload detaches at a speed less than escape velocity it enters an elliptical orbit with a periapsis, apoapsis and eccentricity given by:

$$r_P = \left(\frac{2}{r} - \frac{v^2}{GM_E} \right)^{-1} (1 - e) \tag{25}$$

$$r_A = \left(\frac{2}{r} - \frac{v^2}{GM_E} \right)^{-1} (1 + e) \tag{26}$$

$$e^2 = 1 - \frac{r^2 v_\theta^2}{GM_E} \left(\frac{2}{r} - \frac{v^2}{GM_E} \right) \tag{27}$$

The transition to a circular orbit can be achieved with a bi-elliptical transfer maneuver [12]. This involves a prograde impulse at apoapsis to increase the periapsis, followed by a retrograde impulse at periapsis to circularize the orbit. The maneuver can be implemented with a series of small impulses over several orbits, but the single orbit procedure serves to illustrate the process. The velocity changes at apoapsis and periapsis are given by:

$$\Delta V_A = \sqrt{\frac{2GM_E}{r_A} - \frac{2GM_E}{R + r_A}} - \sqrt{\frac{(1 - e)GM_E}{r_A}} \tag{28}$$

$$\Delta V_P = \sqrt{\frac{2GM_E}{R} - \frac{2GM_E}{R + r_A}} - \sqrt{\frac{GM_E}{R}} \tag{29}$$

The initial orbit depends on the skyhook configuration and its orientation when the payload is released. For the nominal skyhook most orbits have a periapsis smaller than Earth radius, necessitating an impulse during the first orbit to increase the periapsis to avoid reentry into the atmosphere. Only a small impulse is needed for this purpose, which can be provided by a conventional rocket. The rest of the orbital transfer maneuver can be achieved efficiently by employing low thrust electric propulsion over multiple orbits.

To illustrate the process consider a vehicle that is released from the skyhook at an orientation angle $\beta = 1.6$ radians. It enters an elliptical orbit with periapsis 5550 km and apoapsis 71,400 km. A velocity change of 68 m/s at apoapsis increases the periapsis to 6500 km, sufficient to avoid reentry. This can be provided by a chemical rocket with a propellant mass fraction of 0.03. Subsequent circularization of the orbit at the centroid radius requires a velocity change of about 2.8 km/s which can be provided by electric thrusters with a propellant mass fraction of 0.06. This means a reusable vehicle can be used to transport propellant to the skyhook centroid, with only 10% of the initial mass expended as propellant during the journey.

6. Planetary science

Planetary science and space-based astronomy demand increasingly complex infrastructure, and the high cost of launch limits the scope of experiments. A more efficient launch process would allow larger vehicles to be constructed and more ambitious experiments to be undertaken. The orbital skyhook is a fully reusable launch system with high propellant efficiency, and which can be constructed using current materials technology. It can deliver payloads directly to Earth orbit, or to a trajectory for transfer to lunar orbit.

Access to orbit is the first stage of any planetary science mission. Typically a launch vehicle places the spacecraft and its propulsion system into orbit to await the appropriate time to commence interplanetary transfer. Because of the high launch cost a low energy trajectory is usually employed. This restricts the available launch

window and increases the transit time. With a more efficient launch process it would be possible to use a larger and more capable propulsion system, and thus to allow a less efficient trajectory. This flexibility could be used to deliver a larger experimental payload, conduct more frequent missions, or achieve a reduced transit time.

An emerging ambition of national space programs is a return to the moon, often extending to the establishment of permanent bases on the moon and in lunar orbit. Planetary science is unlikely to be a primary driver of this initiative, but it stands to be a significant beneficiary. For astronomy the moon offers a low gravity environment free of atmospheric and ionospheric effects, Earth based radio emissions, and interference due to the large number of satellites in low Earth orbit. A skyhook launch system that provides efficient transport to the moon would allow astronomical experiments with far greater sensitivity than is possible with terrestrial instruments.

Lunar orbit is also a favorable location from which to launch planetary science missions. It is close enough for easy access but at a significantly higher energy than low Earth orbit. Complex modules constructed on Earth can be delivered efficiently by the skyhook, while fuel and water can be supplied from the moon at a much lower energy cost. Vehicles returning from the moon could dock with the skyhook as it approaches a minimum energy state, using it to decelerate in preparation for a low speed re-entry while also returning energy to the system. The use of an orbital skyhook for efficient transport to and from the moon is therefore a key enabler of future planetary science missions.

7. Conclusions

The orbital skyhook derives its advantage principally from using different propulsion technologies in the various physical regimes experienced during a launch. The payload gains energy by momentum transfer from the skyhook, with this energy being later repaid over an extended period. This overcomes the large energy threshold associated with a launch by drawing from a repository and replenishing it efficiently by electric propulsion.

The focus here is on skyhook configurations that allow access at a low speed relative to the Earth. These can be accessed much more easily, but necessarily rotate rapidly to counter the orbital velocity. This means centripetal force dominates the tension, making it is possible to obtain simple expressions for the skyhook mass properties. With a carbon fiber tether the skyhook mass is about 4600 times greater than the endpoint mass, which represents the maximum launch payload. The skyhook mass can be greatly reduced if a stronger tether material were to become available.

Because the skyhook is an extended structure in a non-uniform field, it is subject to forces and torques that vary with orientation. To represent this behavior the skyhook was modeled as a linear structure comprising two masses connected by an inelastic massive tether. The tether mass properties were represented as a compact object at the mass centroid, and a Newtonian formulation used to obtain the equations of motion. These equations were solved numerically to confirm their validity and investigate the dynamics.

Skyhook energy lost during a launch can be replenished by an electric thruster acting at the centroid. The MPD motor is a suitable propulsion technology for this purpose, and was shown to be capable of achieving energy replenishment in a reasonable time with high propellant efficiency. This result holds regardless of the size and efficiency of the propulsion system because the energy transfer process depends only on the efflux velocity and mass flow rate.

Applying thrust at the centroid is beneficial because the structure is most robust at this point and the local acceleration is near zero. It is necessary, however, to transport propellant to the centroid and a mechanism is proposed to achieve this. A transport vehicle is launched by the skyhook into an elliptical orbit, after which it executes an orbital transfer maneuver to rendezvous with the centroid. This process can be accomplished with a high propellant efficiency using available propulsion systems.

The endpoint mass represents the maximum skyhook payload capacity. This envisages the endpoint carrying a docking mechanism of negligible mass that can accept the payload. The skyhook mass scales linearly with the endpoint mass, and so also with the maximum payload. When an initial system has been established it can be used to launch material to add to the structure to increase the payload capacity. This process is likely to be limited by the access vehicle payload capacity, at which point there is no benefit in further increasing the skyhook mass.

Planetary science requires increasingly elaborate experiments. Improved launch efficiency allows more ambitious missions to be undertaken, with larger propulsion systems to deliver more massive experiments to the planet of interest with sufficient propellant for soft landing on the planet surface. The renewed enthusiasm of national space programs for a return to the moon could provide the incentive for construction of an orbital skyhook to provide efficient transport to and from the moon. This would make it possible to conduct astronomical observations from the moon with a sensitivity far greater than is possible from Earth, and to exploit lunar orbit as a base for launching future planetary science missions.

Author details

Colin Sydney Coleman
Defence Science and Technology Group, Edinburgh, Australia

*Address all correspondence to: colin.coleman@dst.defence.gov.au

IntechOpen

References

[1] Isaacs J, Vine A, Bradner H, Bachus G. Satellite elongation into a true "sky-hook". Science. 1966;**151**(3711): 682-683

[2] Pearson J. The orbital tower: A spacecraft launcher using the Earth's rotational energy. Acta Astronautica. 1975;**2**(9–10):785-799

[3] Moravec H. A non-synchronous orbital skyhook. Journal of the Astronautical Sciences. 1977;**25**(4): 307-322

[4] Bogar T, Bangham M, Forward R, Lewis M. Hypersonic airplane space tether orbital launch (HASTOL) system: Interim study results. In: 9th International Space Planes and Hypersonic Systems and Technologies Conference; Norfolk VA; 1999

[5] Bogar T et al. Hypersonic airplane space tether orbital launch system. NASA Institute for Advanced Concepts. Research Grant No 07600-018, Phase 1 Final Report; 2000

[6] Branson's virgin galactic reaches edge of space. BBC News. 13 December 2018

[7] Amos J. New Shepard: Bezos claims success on second spaceship flight. BBC News. 24 November 2015

[8] Coleman J et al. Small but strong: A review of the mechanical properties of carbon nanotube-polymer composites. Carbon. 2006;**44**:1624-1652

[9] Coleman C. The orbital skyhook: Launch dynamics and energy replenishment. In: International Astronautical Conference; Adelaide; 2017

[10] Albertoni R et al. Experimental study of a 100-KW Class applied-field MPD thruster. In: IEPC-2011-110, 32nd International Electric Propulsion Conference; Wiesbaden, Germany; 2011

[11] Choueiri E. New dawn of electric rocket. Scientific American. 2009;**300**: 58-65

[12] Hoelker R, Sibler R. The bi-elliptical transfer between co-planar circular orbits. Planetary and Space Science. 1961;**7**:164-175

Impact Models of Gravitational and Electrostatic Forces

Klaus Wilhelm and Bhola N. Dwivedi

Abstract

The far-reaching gravitational force is described by a heuristic impact model with hypothetical massless entities propagating at the speed of light in vacuum transferring momentum and energy between massive bodies through interactions on a local basis. In the original publication in 2013, a spherical symmetric emission of secondary entities had been postulated. The potential energy problems in gravitationally and electrostatically bound two-body systems have been studied in the framework of this impact model of gravity and of a proposed impact model of the electrostatic force. These studies have indicated that an *antiparallel* emission of a secondary entity—now called *graviton*—with respect to the incoming one is more appropriate. This article is based on the latter choice and presents the modifications resulting from this change. The model has been applied to multiple interactions of gravitons in large mass conglomerations in several publications. They will be summarized here taking the modified interaction process into account. In addition, the speed of photons as a function of the gravitational potential is considered in this context together with the dependence of atomic clocks and the redshift on the gravitational potential.

Keywords: gravitation, electrostatics, potential energies, gravitational redshift and anomalies, secular mass increase

1. Introduction

Newton's law of gravity gives the attraction between two spherical symmetric bodies A and B with masses M and m, respectively, for a separation distance of their centres r (large compared to the sizes of the bodies) at rest in an inertial frame of reference. The force acting between A and B is

$$\boldsymbol{K}_{\mathrm{G}}(r) = -\frac{G_{\mathrm{N}} M \hat{\boldsymbol{r}}}{r^2} \, m, \tag{1}$$

where $G_{\mathrm{N}} = 6.674\,08(31) \times 10^{-11}$ m^3 kg^{-1} s^{-2} is the constant of gravity[1], $\hat{\boldsymbol{r}}$ is the unit vector of the radius vector $\boldsymbol{r}$ with origin at A and $r = |\boldsymbol{r}|$. The first term on the right-hand side represents the classical gravitational field of the mass M.

---

[1] This value and those of other constants (except h, Planck's constant, and e, charge of electron; cf. page 4 and SI, 9th edition 2019) are taken from CODATA 2014 [1].

In close analogy, Coulomb's law yields the force of the electrostatic interaction between particles C and D with charges Q and q, respectively:

$$\boldsymbol{K}_{\mathrm{E}}(r) = \frac{Q\,\hat{r}}{4\pi r^2 \varepsilon_0}\, q,\tag{2}$$

where $\varepsilon_0 = 8.854\,187\,817\ldots \times 10^{-12}$ F m^{-1} is the electric constant in vacuum. Here charges with opposite signs lead to an attraction and with equal signs to a repulsion.

$$\boldsymbol{E}_Q(r) = \frac{Q\,\hat{r}}{4\pi r^2 \varepsilon_0}\tag{3}$$

is the classical electrostatic field of a charge Q.

For two electrons, e.g. the ratio of the gravitational and electrostatic forces is

$$R_{\mathrm{G}}^{\mathrm{E}} = \frac{|\boldsymbol{K}_{\mathrm{E}}(r)|}{|\boldsymbol{K}_{\mathrm{G}}(r)|} = 4.16574 \times 10^{42}.\tag{4}$$

Eq. (1) yields a very good approximation of the gravitational forces, unless effects treated in the general theory of relativity (GTR) [2] are of importance.

The physical processes of the gravitational and the electrostatic fields—in particular their potential energies—are still a matter of debate: Planck [3] wondered about the energy and momentum of the electromagnetic field. A critique of the classical field theory by Wheeler and Feynman [4] concluded that a theory of action at a distance, originally proposed by Schwarzschild [5], avoids the direct notion of fields. Lange [6] calls the fact "remarkable" that the motion of a closed system in response to external forces is determined by the same law as its constituents. It should be recalled here that von Laue [7] considered radiation confined in a certain volume ("Hohlraumstrahlung") and showed that the radiation contributed to the mass of the system according to Einstein's mass-energy equation (see Eq. (51)). In a discussion of energy-momentum conservation for gravitational fields, Penrose [8] finds even for isolated systems " ... something a little 'miraculous' about how things all fit together, ... ", and Carlip [9] wrote in this context: " ... after all, potential energy is a rather mysterious quantity to begin with ... ".

Related to the potential energy problem is the disagreement of Wolf et al. and [10] and Müller et al. [11] on whether the gravitationally redshifted frequency of an atomic clock is caused by the gravitational potential

$$U(r) = -\frac{G_{\mathrm{N}}M}{r}\tag{5}$$

or by the local gravity field $\boldsymbol{g} = \nabla U$.

These remarks and disputes motivated us to think about electrostatic and gravitational fields and the problems related to the potential energies.

2. Gravitational and electrostatic interactions

If far-reaching fields have to be avoided, gravitational and electrostatic models come to mind similar to the emission of photons from a radiation source and their absorption or scattering somewhere else—thereby transferring energy and momentum with the speed of light $c_0 = 299\,792\,458$ m s^{-1} in vacuum [12–15].

We have proposed a heuristic model of Newton's law of gravitation in [16]—without far-reaching gravitational fields—involving hypothetical massless entities. Originally they had been called quadrupoles but will be called *gravitons* now. In subsequent studies, conducted to test the model hypothesis, it became evident that energy and momentum could not be conserved in a closed system without modifying the interaction process of the gravitons with massive bodies and massless particles, such as photons. The modification and the consequences in the context of the gravitational potential energy will be discussed in the following sections together with related topics.

The analogy between Newton's and Coulomb's laws suggests that in the latter case, an impact model might be appropriate as well—with electric dipole entities transferring momentum and energy. This has been proposed in [17]. The equations governing the behaviour of gravitons and dipoles in the next sections are very similar in line with the similarity of Newton's and Coulomb's laws.

Both concepts are required for a description of the gravitational redshift in terms of physical processes in Section 3.8.

2.1 Definitions of gravitons

Without a far-reaching gravitational field, the interactions have to be understood on a local basis with energy and momentum transfers by gravitons. This interpretation has several features in common with a theory based on gravitational shielding conceived by Nicolas Fatio de Duillier [18] at the end of the seventeenth century. A French manuscript can be found in [19], and an outline in German has been provided by Zehe [20]. Related ideas by Le Sage have been discussed in [21].

The gravitational case, in contrast to the electrostatic one, does not depend on polarized particles. Gravitons with an electric quadrupole configuration propagating with the speed of light c_0 will be postulated in the case of gravity. They are the obvious candidates as they have small interaction energies with positive and negative electric charges and, in addition, can easily be constructed with a spin of $S = \pm 2$, if indications to that effect are taken into account, cf. [22].

The vacuum is thought to be permeated by the gravitons that are, in the absence of near masses, isotropically distributed with (almost) no interaction among each other—even dipoles have no mean interaction energy in the classical theory (see, e.g. [23, 24]). The graviton distribution is assumed to be a nearly stable, possibly slowly varying quantity in space and time. It has a constant spatial number density:

$$\rho_G = \frac{\Delta N_G}{\Delta V}. \qquad (6)$$

Constraints on the energy spectrum of the gravitons will be considered in later sections. At this stage we define a mean energy of

$$T_G = |\boldsymbol{p_G}|c_0 = p_G c_0 \qquad (7)$$

for a massless graviton with a momentum vector of $\boldsymbol{p_G}$.

2.2 Definitions of dipoles

A model for the electrostatic force can be obtained by introducing hypothetical electric dipoles propagating with the speed of light. The force is described by the action of dipole distributions on charged particles. The dipoles are transferring momentum and energy between charges through interactions on a local basis.

Apart from the requirement that the absolute values of the positive and negative charges must be equal, nothing is known, at this stage, about the values themselves, so charges of $\pm|q|$ will be assumed, where q might or might not be identical to the elementary charge $e = 1.602\,176\,634 \times 10^{-19}$ C (exact) [25].

The electric dipole moment is

$$\pm\,\boldsymbol{d} = |q|\,\boldsymbol{l} = |q|l\,\hat{\boldsymbol{n}} \tag{8}$$

parallel or antiparallel to the velocity vector $c_0\,\hat{\boldsymbol{n}}$, where $\hat{\boldsymbol{n}}$ is a unit vector pointing in a certain direction and l is the separation distance of the charges. This assumption is necessary in order to get attraction and repulsion of charges depending on their mutual polarities. In Section 2.5 it will be shown that the value $|\boldsymbol{d}|$ of the dipole moment is not critical in the context of our model. The dipoles have a mean energy

$$T_{\mathrm{D}} = |\boldsymbol{p_{\mathrm{D}}}|c_0 = p_{\mathrm{D}}c_0, \tag{9}$$

where $\boldsymbol{p_{\mathrm{D}}}$ represents the momentum of the dipoles. As a working hypothesis, it will first be assumed that $|\boldsymbol{p_{\mathrm{D}}}|$ is constant remote from gravitational centres with the same value for all dipoles of an isotropic distribution. The dipole distribution is assumed to be nearly stable in space and time with a spatial number density

$$\rho_{\mathrm{D}} = \frac{\Delta N_{\mathrm{D}}}{\Delta V}, \tag{10}$$

but will be polarized near electric charges and affected by gravitational centres.

2.3 Virtual entities

As an important step, a formal way will be outlined of achieving the required momentum and energy transfers by discrete interactions. The idea is based on virtual gravitons and dipoles in analogy with other virtual particles, cf. [26–28].

2.3.1 Virtual gravitons

A particle with mass M is symmetrically emitting virtual gravitons with moments $\boldsymbol{p_{\mathrm{G}}^{*}}$ and energies of $T_{\mathrm{G}}^{*} \ll Mc_0^2$. The emission rate is proportional to M. The gravitons will have a certain lifetime Δt_{G} and interact with "real" gravitons. In the literature, there are many different derivations of an energy-time relation, e.g. in [29–31]. Considerations of the spread of the frequencies of a limited wave-packet led Bohr [32] to an approximation for the indeterminacy of the energy that can be rewritten as

$$T_{\mathrm{G}}^{*} \approx \frac{h}{\Delta t_{\mathrm{G}}} \tag{11}$$

with $h = 6.626\,070\,15 \times 10^{-34}$ J s (exact), the Planck constant [25]. For propagating gravitons, the equation

$$T_{\mathrm{G}} = h\,\frac{c_0}{l_{\mathrm{G}}} \tag{12}$$

is equivalent to the photon energy relation $E_\nu = h\nu = hc_0/\lambda$, where λ corresponds to l_{G}, which can be considered as the wavelength of the hypothetical
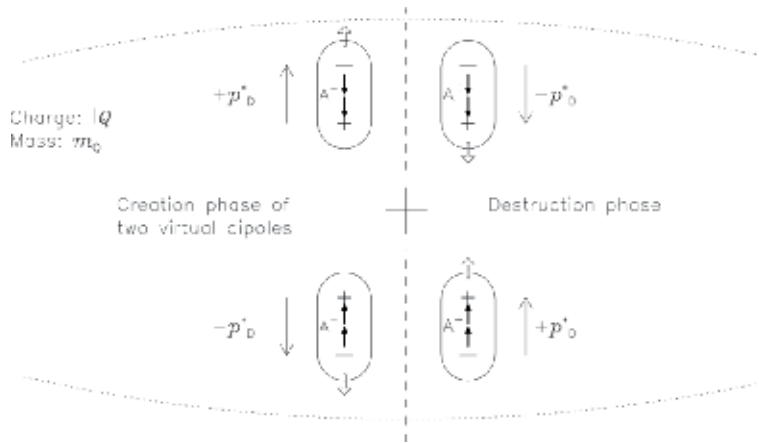
Figure 1.
Conceptional presentation of the creation and destruction phases of virtual dipole pairs by a charge and the corresponding momentum vectors of the virtual dipoles (long arrows). The dipoles are assumed to have a spin of $S = \pm 2 \times \hbar/2$ (short arrows) (**Figure 2** *of [17]).*

gravitons. Since there is experimental evidence that virtual photons (identified as evanescent electromagnetic modes) behave non-locally [33, 34], the virtual gravitons might also behave non-locally. Consequently, the absorption of a real graviton could occur momentarily by a recombination with an appropriate virtual one.

2.3.2 Virtual dipoles

We assume that a particle with charge Q is symmetrically emitting virtual dipoles with $\boldsymbol{p}_{\mathrm{D}}^{*}$. The emission rate is proportional to its charge and the orientation such that a repulsion exists between the charge and the dipoles. The symmetric creation and destruction of virtual dipoles are sketched in **Figure 1**. The momentum balance is shown for the emission phase on the left and the absorption phase on the right side.

Virtual dipoles with energies of $T_{\mathrm{D}}^{*} \ll m_{Q} c_{0}^{2}$ will have a certain lifetime Δt_{D} and interact with *real* dipoles. The energy-lifetime relation

$$T_{\mathrm{D}}^{*} \approx \frac{h}{\Delta t_{\mathrm{D}}} \tag{13}$$

corresponds to that of the gravitons in Eq. (11). The equation

$$T_{\mathrm{D}} = h \frac{c_{0}}{l_{\mathrm{D}}} \tag{14}$$

is for propagating dipoles also equivalent to the photon energy relation, with l_{D} corresponding to λ.

2.4 Newton's law of gravity

The gravitons are absorbed by massive bodies from the background and subsequently emitted at rates determined by the mass M of the body independent of its charge:

$$\frac{\Delta N_{M}}{\Delta t} = \rho_{\mathrm{G}} \kappa_{\mathrm{G}} M = \eta_{\mathrm{G}} M, \tag{15}$$
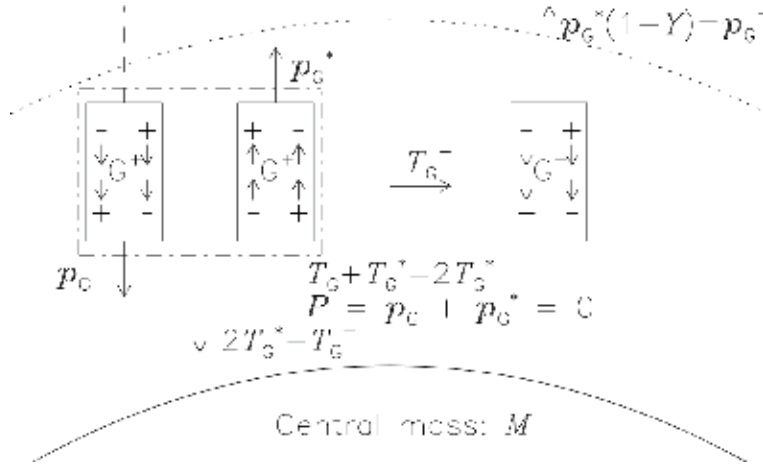
Figure 2.
Interaction of gravitons with a body of mass M. A graviton arriving with a momentum $\boldsymbol{p}_G$ on the left combines together with a virtual graviton with $\boldsymbol{p}_G^* = -\boldsymbol{p}_G$. The excess energy liberates a second virtual graviton with $\boldsymbol{p}_G^-$ on the right in a direction antiparallel to the incoming graviton. The excess energy T_G^- is smaller than T_G^*. The conceptual diagram shows gravitons with a spin $S = \pm 4 \times \hbar/2$ and G^+ or G^- orientation. It is unclear whether such a spin would have any influence on the interaction process (modified from Figure 1 of [16]).

where κ_G is the gravitational absorption coefficient and η_G the corresponding emission coefficient.

Spatially isolated particles at rest in an inertial system will be considered first. The sum of the absorption and emission rates is set equal to the intrinsic de Broglie frequency of the particle, cf. Schrödinger's Zitterbewegung [8, 35–39]. Since the absorption and emission rates must be equal in Eq. (15), this gives an emission coefficient of

$$\eta_G = \kappa_G \rho_G = \frac{1}{2}\frac{c_0^2}{h} = 6.782 \times 10^{49} \ \text{s}^{-1} \ \text{kg}^{-1}, \tag{16}$$

i.e. half the intrinsic de Broglie frequency, since two virtual gravitons are involved in each absorption/emission process (cf. **Figure 2**). The absorption coefficient is constant, because both ρ_G and η_G are constant. For an electron with a mass of $m_e = 9.109\,383\,56(11) \times 10^{-31}$ kg, the virtual graviton production rate equals its de Broglie frequency $\nu_{G,e}^B = m_e c_0^2/h = 1.235\ldots \times 10^{20}$ Hz.

The energy absorption rate of an atomic particle with mass M is

$$\frac{\Delta N_M}{\Delta t} T_G^{ab} = \kappa_G \rho_G M T_G. \tag{17}$$

Larger masses are thought of as conglomeration of atomic particles.
The emission energy, in turn, is assumed to be reduced to

$$T_G^{em} = (1 - Y) T_G \tag{18}$$

per graviton, where Y $(0 < Y \ll 1)$ is defined as the reduction parameter. This leads to an energy emission rate of

$$\frac{\Delta N_M}{\Delta t} T_G^{em} = -\eta_G M (1 - Y) T_G. \tag{19}$$

Without such an assumption, the attractive gravitational force could not be emulated, even with some kind of shadow effect as in Fatio's concept, cf. [18, 19].

The reduction parameter Y and its relation to the attraction are discussed below. If the energy-mass conservation [40] is applied, its consequence is that the mass of matter increases with time at the expense of the background energy of the graviton distribution.

A spherically symmetric emission of the liberated gravitons had been assumed in [16]. Further studies summarized in Sections 3.1, 3.6 and 3.8 indicated that an *antiparallel* emission with respect to the incoming graviton has to be assumed in order to avoid conflicts with energy and momentum conservation principles in closed systems. This important assumption can best be explained by referring to **Figure 2**. The interaction is based on the combination of a virtual graviton with momentum $\boldsymbol{p}_G^*$ and an incoming graviton with $\boldsymbol{p}_G$ followed by the liberation of another virtual graviton in the opposite direction supplied with the excess energy T_G^-. Regardless of the processes operating in the immediate environment of a massive body, it must attract the mass of the combined real and virtual gravitons, which will be at rest in the reference frame of the body. The excess energy T_G^- is, therefore, reduced and so will be the liberation energy, as assumed in Eq. (18). The emission in Eq. (19) will give rise to a flux of gravitons with reduced energies in the environment of a body with mass M. Its spatial density is

$$\rho_M(r) = \frac{\Delta N_M}{\Delta V_r} = \frac{\Delta N_M}{\Delta t} \frac{1}{4\pi r^2 c_0} = \eta_G \frac{M}{4\pi r^2 c_0}, \tag{20}$$

where the volume increase in the time interval Δt is

$$\Delta V_r = 4\pi r^2 c_0 \Delta t. \tag{21}$$

The radial emission is part of the background in Eq. (6), which has a larger number density ρ_G than $\rho_M(r)$ at most distances r of interest. Note that the emission of the gravitons from M does not change the number density or the total number of gravitons. For a certain r_M, defined as the mass radius of M, it has to be

$$\rho_G = \left[\frac{\Delta N_M}{\Delta V_r}\right]_{r_M} = \frac{\eta_G}{c_0} \frac{M}{4\pi r_M^2}, \tag{22}$$

because all gravitons of the background that come so close interact with the mass M in some way. The same arguments apply to a mass $m \neq M$ and, in particular, to the electron mass m_e.

Therefore

$$\sigma_G = \frac{m}{4\pi r_m^2} = \frac{M}{4\pi r_M^2} = \frac{m_e}{4\pi r_{G,e}^2} \tag{23}$$

will be independent of the mass as long as the density of the background distribution is constant. The quantity σ_G is a kind of surface mass density. The equation shows that σ_G is determined by the electron mass radius $r_{G,e}$, for which estimates will be provided in Sections 3.2 and 3.3. From Eqs. (16), (22) and (23), it follows that

$$\kappa_G \sigma_G = c_0. \tag{24}$$

The flux of modified gravitons from M will interact with a particle of mass m and vice versa. The interaction rate in the static case can be found in Eqs. (15) and (20):

$$\frac{\Delta N_{M,m}(r)}{\Delta t} = \kappa_{\mathrm{G}} m \frac{\Delta N_M}{\Delta V_r} = \frac{\kappa_{\mathrm{G}} \eta_{\mathrm{G}}}{c_0} \frac{Mm}{4\pi r^2} = \frac{\kappa_{\mathrm{G}} c_0}{2h} \frac{mM}{4\pi r^2} = \kappa_{\mathrm{G}} M \frac{\Delta N_m}{\Delta V_r} = \frac{\Delta N_{m,M}(r)}{\Delta t}. \quad (25)$$

A calculation with *antiparallel* emissions of the secondary gravitons shows that an interaction of a graviton with reduced momentum $\boldsymbol{p}_{\mathrm{G}}^-$ provides $-\boldsymbol{p}_{\mathrm{G}}\left(2Y - Y^2\right)$ together with its unmodified counterpart from the opposite sides. The resulting imbalance will be

$$\frac{\Delta \boldsymbol{P}_{M,m}(r)}{\Delta t} \approx -2\boldsymbol{p}_{\mathrm{G}} Y \frac{\Delta N_{M,m}(r)}{\Delta t} = -\boldsymbol{p}_{\mathrm{G}} Y \kappa_{\mathrm{G}} \frac{c_0}{h} \frac{Mm}{4\pi r^2}, \quad (26)$$

if the quadratic terms in Y can be neglected for very small Y scenarios.

The imbalance will cause an attractive force that is responsible for the gravitational pull between bodies with masses M and m. By comparing the force expression in Eq. (26) with Newton's law in Eq. (1), a relation between p_{G}, Y, κ_{G} and G_{N} can be established through the constant G_{G}:

$$G_{\mathrm{G}} = p_{\mathrm{G}} Y \kappa_{\mathrm{G}} \approx 4\pi G_{\mathrm{N}} \frac{h}{c_0} = 1.853\ldots \times 10^{-51} \ \mathrm{m}^4 \ \mathrm{s}^{-2}. \quad (27)$$

It can be seen that Y does not depend on the mass of a body. Since Eq. (18) allows stable processes over cosmological time scales only, if Y is very small, we assume in **Figure 3** that $Y < 10^{-15}$.

Note that the mass of a body and thus its intrinsic de Broglie frequency are not strictly constant in time, although the effect is only relevant for cosmological time scales (see lower panel of **Figure 3**). In addition, multiple interactions will occur within large mass conglomerations (see Sections 3.4–3.6) and can lead to deviations from Eqs. (1).

The graviton energy density remote from any masses will be

$$\epsilon_{\mathrm{G}} = T_{\mathrm{G}} \rho_{\mathrm{G}} = \frac{2\pi G_{\mathrm{N}}}{Y} \sigma_{\mathrm{G}}^2, \quad (28)$$

where the last term is obtained from Eq. (27) with the help of Eqs. (16) and (22)–(24).

What will be the consequences of the mass accretion required by the modified model? With Eqs. (17), (19) and (27), it follows that the relative mass accretion rate of a particle with mass M will be

$$A = \frac{1}{M}\frac{\Delta M}{\Delta t} = \frac{2\pi G_{\mathrm{N}}}{c_0} \sigma_{\mathrm{G}} = \frac{2\pi G_{\mathrm{N}}}{c_0} \frac{m_{\mathrm{e}}}{4\pi r_{\mathrm{G,e}}^2}, \quad (29)$$

which implies an exponential growth according to

$$M(t) = M_0 \exp\left[A\left(t - t_0\right)\right] \approx M_0\left(1 + A\,\Delta t\right), \quad (30)$$

where $M_0 = M(t_0)$ is the initial value at t_0 and the linear approximation is valid for small $A\left(t - t_0\right) = A\,\Delta t$. The accretion rate is

$$A = \frac{1.014 \times 10^{-49}}{r_{\mathrm{G,e}}^2} \ \mathrm{m}^2 \ \mathrm{s}^{-1}, \quad (31)$$

if the expression is evaluated in terms of recent parameters.
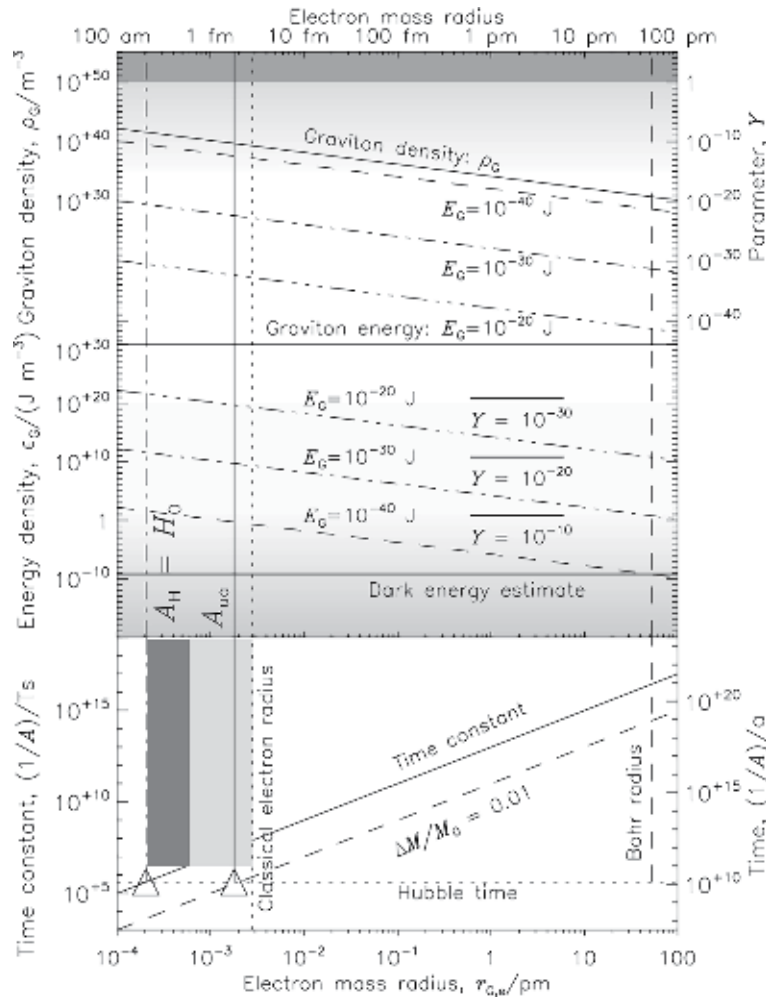
Figure 3.
*Energies of $E_G = (10^{-40}$ to $10^{-20})$ J are assumed for the gravitons, as indicated in the upper and middle panels by different line styles. In the upper panel, the spatial number density of gravitons and the corresponding reduction parameter Y of Eq. (18) are plotted as functions of the electron mass radius $r_{G,e}$. The range $Y \geq 1$ (dark shading) is obviously completely excluded by the model. Even values greater than $\approx 10^{-15}$ are not realistic (light shaded region), cf. paragraph following Eq. (27). The cosmic dark energy estimate (3.9 ± 0.4) GeV m$^{-3} = (6.2 \pm 0.6) \times 10^{-10}$ J m^{-3} (see [44]) is marked in the second panel. It is well below the acceptable range (light shaded and unshaded regions in the middle panel). If, however, only the Y portion is taken into account in the dark energy estimate, the total energy density could be many orders of magnitude larger as shown for Y from 10^{-10} to 10^{-30} by short horizontal bars. In the lower panel, the mass accretion time constant and the time required for a relative mass increase of 1% are shown (on the right side in units of years). Indicated is also the Hubble time $1/H_0$ as well as the lower limit of the electron mass radius (left triangle and dark shaded area) estimated from the Pioneer anomaly. The light shaded area takes smaller Pioneer anomalies into account (see Section 3.2). It is shown up to the vertical dotted line for the classical electron radius of 2.82 fm. The right triangle and the vertical solid line show the result in Section 3.3 based on the observed secular increase of the Sun-Earth distance [45] (modified from **Figure 2** of [16]).*

The gravitational quantities are displayed with these assumptions in a wide parameter range in **Figure 3** (although the limits are set rather arbitrarily). The lower panel displays the time constant of the mass accretion. It indicates that a significant mass increase would be expected within the standard age of the Universe of the order of $1/H_0$ (with the Hubble constant H_0) only for very small $r_{G,e}$.

Fahr and Heyl [41] have suggested that a decay of the vacuum energy density creates mass in an expanding universe, and Fahr and Siewert [42] found a mass creation rate in accordance with Eq. (30).

The relative uncertainty of the present knowledge of the Rydberg constant

$$R_\infty = \frac{\alpha^2 m_e c_0}{2h} = 10\,973\,731.568\,508 \ \text{m}^{-1} \tag{32}$$

is $u_r \approx 5.9 \times 10^{-12}$, where

$$\alpha = \frac{e^2}{2\varepsilon_0 c_0 h} = 7.297\,352\,5664(17) \times 10^{-3} \tag{33}$$

is Sommerfeld's fine-structure constant. Since spectroscopic observations of the distant universe with redshifts up to $z \le 0.5$ are compatible with modern data, it appears to be reasonable to set $(1 + u_r) M_0 \ge M(t) > M_0$ at least for the time interval $\Delta t \le 1.6 \times 10^{17}$ s. Any variation of R_∞, caused by the linear dependence upon the electron mass, which has also been considered in [43], would then be below the detection limit for state-of-the-art methods.

From the emission rate and the lifetime of virtual gravitons in Eqs. (15) and (11), an estimate of their total number and energy at any time can thus be obtained for a body with mass M as

$$N_G^{\text{tot}} = \Delta t_G \, \frac{M c_0^2}{h} \tag{34}$$

and

$$T_G^{\text{tot}} = N_G^{\text{tot}} \, T_G^* \approx M c_0^2, \tag{35}$$

i.e. the mass of a particle would reside within the virtual gravitons.

2.5 Coulomb's law

2.5.1 Electrostatic fields and charged particles

Coulomb's law in Eq. (2) gives the attractive or repulsive electrostatic force between two charged particles at rest in an inertial system. Together with the electrostatic field in Eq. (3), it can be written as

$$\boldsymbol{K}_E(r) = \boldsymbol{E}_Q(r)q. \tag{36}$$

The electrostatic potential $U_E(r)$ of a charge Q, located at $r = 0$, is for $r > 0$

$$U_E(r) = \frac{Q}{4\pi r \varepsilon_0}. \tag{37}$$

The corresponding electrostatic field can thus be written as $\boldsymbol{E}_Q(r) = -\nabla U_E(r)$.

2.5.2 Dipole interactions

Note that the dipoles in the background distribution, cf. Eq. (10), have no mean interaction energy, even in the classical theory (see, e.g. [24]). Whether this

"background dipole radiation" and the "graviton radiation" are related to the dark matter (DM) and dark energy (DE) problems is of no concern here but could be an interesting speculation.

A charge Q absorbs and emits dipoles at a rate

$$\frac{\Delta N_Q}{\Delta t} = \kappa_D \rho_D |Q| = \eta_D |Q|, \qquad (38)$$

where η_D and κ_D are the corresponding (dipole) emission and absorption coefficients.

From energy conservation it follows that absorption and emission rates of dipoles in Eq. (38) of a body with charge Q must be equal. The momentum conservation can, in general, be fulfilled by isotropic absorption and emission processes.

The interaction processes assumed between a positively charged body and dipoles is sketched in **Figure 4**. A mass m_Q of the charge Q has explicitly been mentioned, because the massless dipole charges are not assumed to absorb and emit any dipoles themselves. The conservation of momentum could hardly be fulfilled in such a process. In Section 3.8 we postulate, however, that gravitons interact with dipoles and thereby control their momentum and speed, subject to the condition that $p_G \ll p_D$.
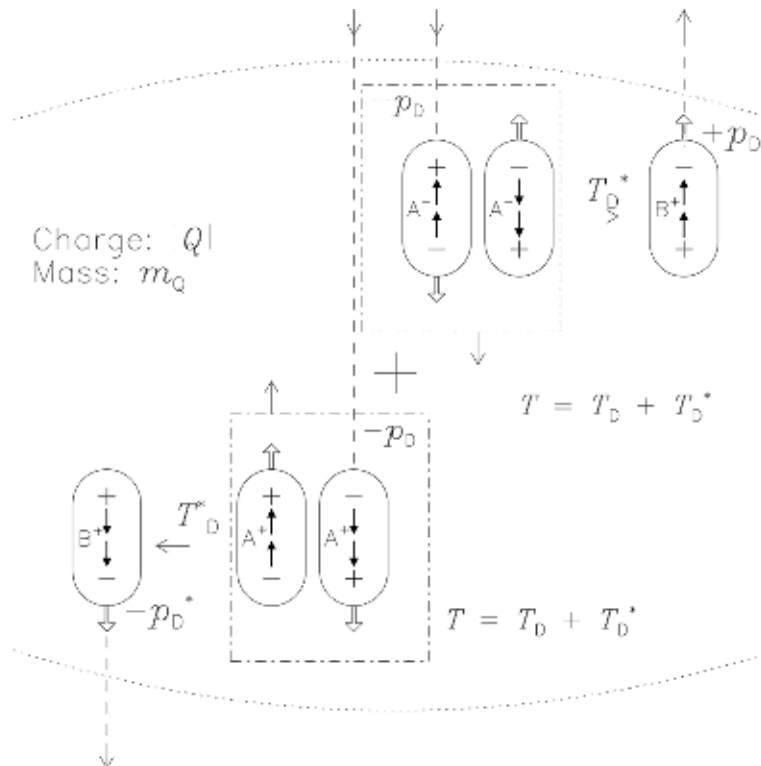
Figure 4.
Virtual dipoles emitted by a charge $+|Q|$ (with mass m_Q) interact with real dipoles, A^+ and A^- arriving with a momentum $-\boldsymbol{p}_D$, each. On the left, a dipole A^+ combines in the lower dashed-dotted box with virtual dipole A^+ in its destruction phase and liberates dipole B^+. No momentum will be transferred to the central charge with $p_D = p_D^*$. The other types of interaction—called direct interaction, in contrast to the indirect one on the left— also require two virtual dipoles, one of them combines in its creation phase with dipole A^- (in the upper box with dashed-dotted boundaries), and the other one is liberated by the excess energy of the annihilation. The central charge received a momentum of $-(p_D + p_D^*) = -2p_D$. No spin reversal has been assumed in both cases.

The assumptions as outlined will lead to a distribution of the emitted dipoles in the rest frame of an isolated charge Q with a spatial density of

$$\rho_Q(r) = \frac{\Delta N_Q}{\Delta V_r} = \frac{1}{4\pi r^2 c_0}\frac{\Delta N_Q}{\Delta t} = \eta_D \frac{|Q|}{4\pi r^2 c_0}, \tag{39}$$

where ΔV_r is given in Eq. (21). The radial emission is part of the background ρ_D, which has a larger number density than $\rho_D(r)$ at most distances r of interest. Note that the emission of the dipoles from Q does not change the number density ρ_D in the environment of the charge but reverses the orientation of *half* of the dipoles affected.

The total number of dipoles will, of course, not be changed either. For a certain r_Q, defined as the charge radius of Q, it has to be

$$\rho_D = \left[\frac{\Delta N_Q}{\Delta V_r}\right]_{r_Q} = \frac{\eta_D}{c_0}\frac{|Q|}{4\pi r_Q^2}, \tag{40}$$

because all dipoles of the background that come so close interact with the charge Q in some way. The same arguments apply to a charge $q \neq Q$. Since ρ_D cannot depend on either q or Q, the quantity

$$\sigma_Q = \frac{|Q|}{4\pi r_Q^2} = \frac{|q|}{4\pi r_q^2} = \frac{|e|}{4\pi r_e^2} \tag{41}$$

must be independent of the charge and can be considered as a kind of surface charge density, cf. "Flächenladung" of an electron defined by Abraham [46], which is the same for all charged particles. The equation shows that σ_Q is determined by the electron charge radius r_e.

At this stage, this is a formal description awaiting further quantum electrodynamic studies in the near-field region of charges. It might, however, be instructive to provide a speculation for the dipole emission rate $\Delta N_Q/\Delta t$ of a charge Q. The physical constants α, c_0, h, ϵ_0 and G_N can be combined to give a dipole emission coefficient

$$\eta_D = \frac{1}{2}\frac{\alpha^2 c_0^2}{h\sqrt{\epsilon_0 G_N}} = 1.486 \times 10^{56} \ \text{s}^{-1} \ \text{C}^{-1} \tag{42}$$

as half the virtual dipole production rate and thus for a charge $|e|$ a rate of

$$\frac{\Delta N_e}{\Delta t} = \eta_D |e| = 2.380 \times 10^{37} \ \text{s}^{-1}. \tag{43}$$

Note that the dipole emission rate is fixed for a certain charge and does not depend on the particle mass. From Eqs. (38), (40) and (41), we get

$$\kappa_D \sigma_Q = c_0. \tag{44}$$

During a *direct* interaction, the dipole A^- (arriving in **Figure 4** from above on the right side) combines together with an identical virtual dipole with an opposite velocity vector. This postulate is motivated by the fact that it provides the easiest way to eliminate the charges and yield $P = -p_D + p_D^* = 0$, where $p_D^* = p_D$ is the magnitude of the momentum vector of a virtual dipole, cf. Eq. (9). The momentum balance is neutral, and the excess energy T_D is used to liberate a second virtual

dipole B^+, which has the required orientation. The charge had emitted two virtual dipoles with a momentum of $+p_D^*$, each, and a total momentum of $-(p_D + p_D^*) = -2p_D$ was transferred to $|Q|$. The process can be described as a reflection of a dipole together with a reversal of the dipole momentum. The number of these direct interactions will be denoted by $\Delta \hat{N}_Q$. The dipole of type A^+ (arriving from above on the left side) can exchange its momentum in an *indirect* interaction only on the far side of the charge with an identical virtual dipole during its absorption (or destruction) phase (cf. **Figure 1**). The excess energy of T_D is supplied to liberate a second virtual dipole B^+. The momentum transfer to the charge $+|Q|$ is zero. This process just corresponds to a double charge exchange. Designating the number of interactions of the indirect type with $\Delta \tilde{N}_Q$, it is

$$\frac{\Delta N_Q}{\Delta t} = \frac{\Delta \hat{N}_Q + \Delta \tilde{N}_Q}{\Delta t} \tag{45}$$

with $\Delta \tilde{N}_Q = \Delta \hat{N}_Q = \Delta N_Q / 2$. Unless direct and indirect interactions are explicitly specified, both types are meant by the term "interaction". The virtual dipole emission rate in **Figure 4** has to be

$$\frac{\Delta N_Q^*}{\Delta t} = 2 \frac{\Delta N_Q}{\Delta t}, \tag{46}$$

i.e. the virtual dipole emission rate equals the sum of the real absorption and emission rates. The interaction model described results in a mean momentum transfer per interaction of p_D *without involving a macroscopic electrostatic field*.

A quantitative evaluation gives the force acting on a test particle with charge q at a distance r from another particle with charge Q. This results from the absorption of dipoles not only from the background but also from the distribution emitted from Q according to Eq. (39) under the assumption of a *constant* absorption coefficient κ_D in Eq. (38). The rate of interchanges between these charges then is

$$\frac{\Delta N_{Q,q}(r)}{\Delta t} = \kappa_D |q| \frac{\Delta N_Q}{\Delta V_r} = \frac{\kappa_D \eta_D}{c_0} \frac{|Q| |q|}{4 \pi r^2} = \kappa_D |Q| \frac{\Delta N_q}{\Delta V_r} = \frac{\Delta N_{q,Q}(r)}{\Delta t}, \tag{47}$$

which confirms the reciprocal relationship between q and Q. The equation, also very similar to Eq. (25), does not contain an explicit value for η_D. It is important to realize that all interchange events between pairs of charged particles are either direct or indirect depending on their polarities and transfer of a momentum of $\pm 2p_D$ or zero.

The external electrostatic potential of a spherically symmetric body C with charge Q is given in Eq. (37). Since the electrostatic force between the charged particles C and D is typically many orders of magnitude larger than the gravitational force, we only take the electrostatic effects into account in this section and neglect the gravitational interactions.

In order to have a well-defined configuration for our discussion, we will assume that body C with mass m_C has a positive charge $Q > 0$ and is positioned at a distance r beneath body D (mass m_D) with either a charge $+|q|$ in **Figure 5** or $-|q|$ in **Figure 6**. Only the processes near body D are shown in detail.

The interaction rates of dipoles with bodies C and D in Eq. (47) (the same for both bodies even if $|Q| \neq |q|$) and the momentum transfers indicated in **Figures 5** and **6**, respectively, lead to a norm of the momentum change rate for bodies C and D of
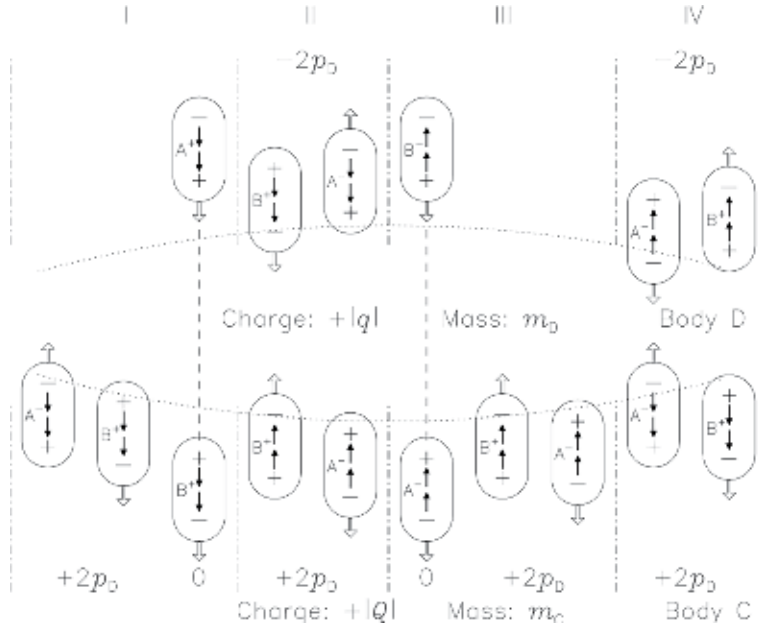
Figure 5.
*Body C with charge $Q > 0$ and mass m_C is positioned in this configuration beneath body D with charge $+|q|$ and mass m_D leading to an electrostatic repulsion of the bodies. This results from the reversal of dipoles by the charge Q followed by direct interactions with the charge $+|q|$ as defined on the right-hand side of **Figure 4**. Two reversals are schematically indicated in columns I and III. The dipoles arriving in columns II and IV from below have the same polarity as if they would be part of the background distribution and do not contribute to the momentum transfer, because of a compensation by dipoles arriving from above. The net momentum transfer caused by the two interacting reversed dipoles thus is $4\boldsymbol{p}_D$, i.e. $2\boldsymbol{p}_D$ per dipole (modified from **Figure 3** of [17]).*

$$\left| \frac{\Delta \boldsymbol{P}_{Q,q}(r)}{\Delta t} \right| = 2p_D \frac{\Delta N_{Q,q}(r)}{\Delta t} = 2p_D \frac{\kappa_D \eta_D}{c_0} \frac{Q\,|q|}{4\pi r^2}. \tag{48}$$

Together with

$$p_D \frac{\kappa_D \eta_D}{c_0} = \frac{T_D \kappa_D \eta_D}{c_0^2} = \frac{1}{2\varepsilon_0} \tag{49}$$

this leads, depending on the signs of the charges Q and q, to a repulsive or an attractive electrostatic force between C and D in accordance with Coulomb's law in Eq. (2).

Important questions are related to the energy T_D and momentum $\boldsymbol{p}_D$ of the dipoles and, even more, to their energy density in space. Eqs. (9), (40), (41) and (44) together with Eq. (49) allow the energy density to be expressed by

$$\epsilon_D = T_D \rho_D = \frac{\sigma_D^2}{2\varepsilon_0}. \tag{50}$$

This quantity is independent of the dipole energy. It takes into account all dipoles (whether their distribution is chaotic or not). Should the energy density vary in space and/or time, the surface charge density σ_Q must vary as well.

If we assume that the electron charge radius r_Q in Eq. (41) equals the classical electron radius $r_e = 2.82$ fm, then an energy density of $\epsilon_D = 1.45 \times 10^{29}$ J m^{-3} (very high compared to the present cosmic dark energy estimate) follows from
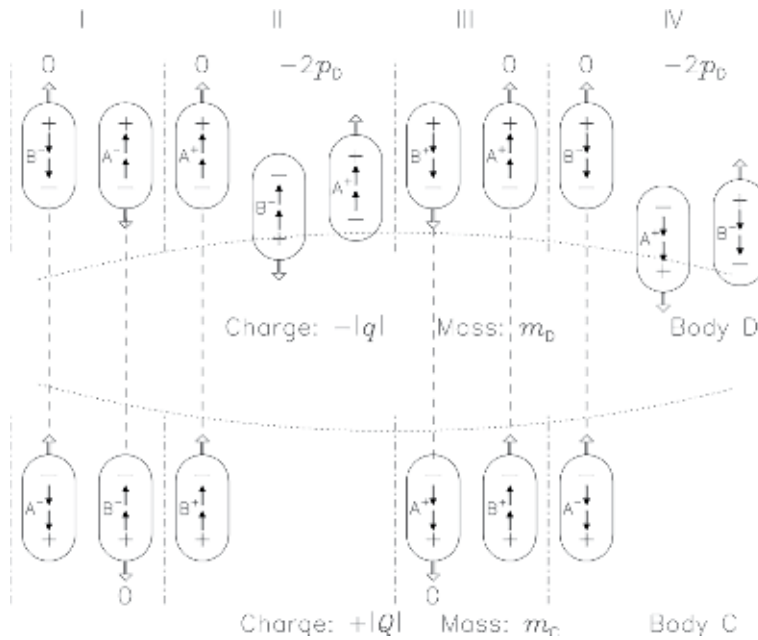
Figure 6.
*Body C is again positioned beneath body D. The charge of D is now −|q|, however, leading to an electrostatic attraction of the bodies. The attraction results from the reversal of dipoles by the charge Q > 0 followed by indirect interactions with charge −|q| as defined on the left-hand side of **Figure 4**. Two events without momentum transfer are schematically indicated in columns II and IV. The dipoles arriving in columns I and III from below have the same polarity as if they would be part of the background distribution. The same is true for all dipoles arriving from above. The net momentum transfer caused by the two reversed dipoles thus is −4$\mathbf{p}_D$, i.e. −2$\mathbf{p}_D$ per dipole (modified from **Figure 4** of [17]).*

Eq. (50). The dipole density $\rho_D = 7.95 \times 10^{56}$ m^{-3} in Eq. (40) is also very high, leading to a dipole energy of $T_D = 1.83 \times 10^{-28}$ J. If, on the other hand, we identify the dipole distribution with DM with an estimated energy density of 2.48×10^{-10} J m^{-3} and require that the dipole energy density corresponds to this value, then extreme values follow for $r_Q = 13.9\,\mu$m, $\rho_D = 3.28 \times 10^{37}$ m^{-3} and $T_D = 7.55 \times 10^{-48}$ J.

3. Applications of impact models

The detection of gravitons and dipoles with the expected properties would, of course, be the best verification of the proposed models. Lacking this, indirect support can be found through the application of the models with a view to describe physical processes successfully for specific situations.

3.1 Potential energies

3.1.1 Gravitational potential energy

As mentioned in Section 1, the study of the potential energy problem [47] had been motivated by the remark that the potential energy is rather mysterious [9].[2]

---

[2] In this context, it is of interest that Brillouin [48] discussed this problem in relation to the electrostatic potential energy.

It led to the identification of the "source region" of the potential energy for the special case of a system with two masses M_E and M_M subject to the condition $M_E \gg M_M$. An attempt to generalize the study without this condition required either violations of the energy conservation principle as formulated by von Laue [49] for a closed system or a reconsideration of an assumption we made concerning the gravitational interaction process in [16]. The change necessary to comply with the energy conservation principle has been discussed in Section 2.4. A generalization of the potential energy concept for a system of two spherically symmetric bodies A and B with masses m_A and m_B without the above condition could then be formulated [50].

We will again exclude any further energy contributions, such as rotational or thermal energies, and make use of the fact that the external gravitational potential of a spherically symmetric body of mass M and radius r in Eq. (5) is that of a corresponding point mass at the centre.

The energy E_m and the momentum $\boldsymbol{p}$ of a free particle with mass m moving with a velocity $\boldsymbol{v}$ relative to an inertial reference system are related by

$$E_m^2 - \boldsymbol{p}^2 c_0^2 = m^2 c_0^4, \tag{51}$$

where $\boldsymbol{p}$ is the momentum vector

$$\boldsymbol{p} = \boldsymbol{v}\,\frac{E_m}{c_0^2} \tag{52}$$

[40, 51]. For an entity in vacuum with no rest mass ($m = 0$), such as a photon [15, 52, 53], the energy-momentum relation in Eq. (51) reduces to

$$E_\nu = p_\nu c_0. \tag{53}$$

In [50] we assume that two spherically symmetric bodies A and B with masses m_A and m_B, respectively, are placed in space remote from other gravitational centres at a distance of $r + \Delta r$ reckoned from the position of A. Initially both bodies are at rest with respect to an inertial reference frame represented by the centre of gravity of both bodies. The total energy of the system then is with Eq. (51) for the rest energies and with Eq. (5) for the potential energy

$$E_S = (m_A + m_B)c_0^2 - G_N\,\frac{m_A m_B}{r + \Delta r}. \tag{54}$$

The evolution of the system during the approach of A and B from $r + \Delta r$ to r can be described in classical mechanics. According to Eq. (48), the attractive force between the bodies during the approach is approximately constant for $r \gg \Delta r > 0$, resulting in accelerations of $b_A = |K_G(r)|/m_A$ and $b_B = -|K_G(r)|/m_B$, respectively. Since the duration Δt of the free fall of both bodies is the same, the approach of A and B can be formulated as

$$\Delta r = s_A - s_B = \frac{1}{2}\,(b_A - b_B)\,(\Delta t)^2 = \frac{1}{2}\left(\frac{1}{m_A} + \frac{1}{m_B}\right)|K_G(r)|\,(\Delta t)^2, \tag{55}$$

showing that $s_A m_A = -s_B m_B$, i.e. the centre of gravity stays at rest. Multiplication of Eq. (55) by $|K_G(r)|$ gives the corresponding kinetic energy equation

$$|K_G(r)|\,\Delta r = \frac{1}{2}\left(\frac{K_G^2(r)\,(\Delta t)^2}{m_A} + \frac{K_G^2(r)\,(\Delta t)^2}{m_B}\right) = \frac{1}{2}\,m_A v_A^2 + \frac{1}{2}\,m_B v_B^2 = T_A + T_B. \tag{56}$$

The kinetic energies[3] T_A and T_B should, of course, be the difference of the potential energy term in Eq. (54) at distances of r and $r + \Delta r$. We find indeed for small Δr with Newton's law in Eq. (1):

$$G_N\, m_A\, m_B \left(\frac{1}{r} - \frac{1}{r + \Delta r} \right) \approx G_N\, \frac{m_A\, m_B}{r^2}\, \Delta r = |K_G(r)|\, \Delta r. \qquad (57)$$

We may now ask the question, whether the impact model can provide an answer to the potential energy "mystery" in a closed system. Since the model implies a secular increase of mass of all bodies, it obviously violates a closed-system assumption. The increase is, however, only significant over cosmological time scales, and we can neglect its consequences in this context. A free single body will, therefore, still be considered as a closed system with constant mass. In a two-body system, both masses m_A and m_B will be constant in such an approximation, but now there are gravitons interacting with both masses.

The number of gravitons travelling at any instant of time from one mass to the other can be calculated from the interaction rate in Eq. (25) multiplied by the travel time r/c_0:

$$\Delta N_{m_A, m_B}(r) = \frac{\kappa_G}{8\pi h} \frac{m_A\, m_B}{r}. \qquad (58)$$

The same number is moving in the opposite direction. The energy deficiency of the interacting gravitons with respect to the corresponding background then is together with Eqs. (18) and (27) for each body

$$\Delta E_G(r) = -p_G\, Y \kappa_G\, \frac{c_0}{8\pi h} \frac{m_A\, m_B}{r} = -G_G\, \frac{c_0}{8\pi h} \frac{m_A\, m_B}{r} = -\frac{G_N}{2} \frac{m_A\, m_B}{r}. \qquad (59)$$

The last term shows—with reference to Eq. (57)—that the energy deficiency ΔE_G equals *half* the potential energy of body A at a distance r from body B and vice versa.

We now apply Eq. (59) and calculate the difference of the energy deficiencies for separations of $r + \Delta r$ and r for interacting gravitons travelling in both directions and get

$$2\{\Delta E_G(r + \Delta r) - \Delta E_G(r)\} = G_N\, m_A\, m_B \left(\frac{1}{r} - \frac{1}{r + \Delta r} \right). \qquad (60)$$

Consequently, the difference of the potential energies between $r + \Delta r$ and r in Eq. (57) is balanced by the difference of the total energy deficiencies.

The physical processes involved can be described as follows:

1. The number of gravitons on their way for a separation of $r + \Delta r$ is smaller than that for r, because the interaction rate depends on r^{-2} according to Eq. (48), whereas the travel time is proportional to r.

2. A decrease of $r + \Delta r$ to r during the approach of A and B increases the number of gravitons with reduced energy.

---

[3] Eqs. (51) and (52) together with $E_0 = mc_0^2$ [c] and $\gamma = 1/\sqrt{1 - v^2/c_0^2}$ yield the relativistic kinetic energy of a massive body: $T = E - E_0 = E_0(\gamma - 1)$. The evaluations for T_A and T_B agree in very good approximation with Eq. (56) for small v_A and v_B.

3. The energies liberated by energy reductions are available as potential energy and are converted into kinetic energies of bodies A and B.

4. With Eqs. (51) and (52) and the approximations in Footnote 3, it follows that the sum of the kinetic energies T_A and T_B, the masses A and B, plus the total energy deficiencies of the interacting gravitons can indeed be considered to be a closed system as defined by von Laue [49].

3.1.2 Electrostatic potential energy.

In this section we will discuss the electrostatic aspects of the potential energy. The energy density of an electrostatic field E outside of charges is given by

$$w = \frac{\varepsilon_0}{2} \, E^2, \tag{61}$$

cf., e.g. [24, 54]. Applying Eq. (61) to a plane-plate capacitor with an area F, a plate separation b and charges $\pm|Q|$ on the plates, the energy stored in the field of the capacitor turns out to be

$$W = \frac{\varepsilon_0}{2} \, E^2 F b = \frac{\varepsilon_0}{2} E^2 \, V. \tag{62}$$

With a potential difference $\Delta U_E = |E| b$ and a charge of $Q = \varepsilon_0 |E| F$ (increased incrementally to these values), the potential energy of Q at ΔU_E is

$$W = \frac{1}{2} Q \, \Delta U_E. \tag{63}$$

The question as to where the energy is actually stored, [54] answered by showing that both concepts implied by Eqs. (62) and (63) are equivalent.

Can the impact model provide an answer for the electrostatic potential energy in a closed system, where dipoles are interacting with two charged bodies? This question we posed in [55]: the number of reversed dipoles travelling at any instant of time from a charge $Q > 0$ to q in **Figures 5** and **6** can be calculated from the interaction rate in Eq. (47) multiplied by a travel time $\Delta t = r/c_0$:

$$\Delta N_{Q,q}(r) = \frac{\kappa_D \eta_D}{c_0^2} \frac{Q \, |q|}{4 \pi r}. \tag{64}$$

The same number of dipoles is moving in the opposite direction from q to Q. From Eqs. (9), (49) and (64), we can determine the total energy of the reversed dipoles:

$$\Delta E_{Q,q}(r) = 2 \Delta N_{Q,q}(r) p_D c_0 = \frac{Q \, |q|}{4 \pi \varepsilon_0 r}. \tag{65}$$

It is equal to the absolute value of the electrostatic potential energy of a charge q at the electrostatic potential $U_E(r)$ in Eq. (37) of a charge Q.

The evolution of the system is similar to that of the gravitational case in Section 3.1.1; however, attraction and repulsion have to be considered during the approach or separation of bodies C and D. The initial distance between C and D be r, when both bodies are assumed to be at rest, and changes to $r \pm \Delta r$ by the repulsive or attractive force $K_E(r)$ between the charges given by Coulomb's law in Eq. (2) The force is approximately constant for $r \gg \Delta r > 0$ causing accelerations of $b_D = K_E(r)/m_D$ and $b_C = -K_E(r)/m_C$, respectively. Since the duration Δt of the

motions of both bodies is the same, the separation (upper sign) or approach (lower sign) of C and D can be formulated as follows:

$$\pm \Delta r = \pm (s_D - s_C) = \pm \frac{1}{2} (b_D - b_C)(\Delta t)^2 = \frac{1}{2} \left(\frac{1}{m_C} + \frac{1}{m_D} \right) K_E(r)(\Delta t)^2. \quad (66)$$

Comparing the second term of the equation with the last one, it can be seen that $s_D m_D = -s_C m_C$, i.e. the centre of gravity stays at rest. Multiplication of Eq. (66) by $K_E(r)$ gives a good estimate of the corresponding kinetic energy:

$$\pm \Delta r K_E(r) = \pm \Delta r \frac{Qq}{4\pi \varepsilon_0 r^2} = \frac{1}{2} \frac{K_E^2(r)}{m_B} (\Delta t)^2 + \frac{1}{2} \frac{K_E^2(r)}{m_A} (\Delta t)^2 = \frac{1}{2} m_D v_D^2 + \frac{1}{2} m_C v_C^2$$
$$= T_D + T_C > 0, \quad (67)$$

where $v_D = b_D \Delta t$ and $v_C = b_C \Delta t$ are the speeds of the bodies, when the distances $r \pm \Delta r$ between C and D are attained. The sum of the kinetic energies T_C and T_D must, of course, be equal to the difference of the electrostatic potential energy at distances of r and $r \pm \Delta r$:

$$\{U(r) - U(r \pm \Delta r)\} q = \frac{Qq}{4\pi \varepsilon_0} \left(\frac{1}{r} - \frac{1}{r \pm \Delta r} \right) \approx \pm \Delta r \frac{Qq}{4\pi \varepsilon_0 r^2} > 0. \quad (68)$$

The variations of the number of $\Delta N_{Q,q}(r)$ dipoles in Eqs. (58) and (65) during the separation or approach of bodies C and D from r to $r \pm \Delta r$ are

$$\delta N_{Q,q}(r, \Delta r) = \Delta N_{Q,q}(r \pm \Delta r) - \Delta N_{Q,q}(r)$$
$$= \frac{\eta_D \kappa_D}{c_0^2} \frac{Q|q|}{4\pi} \left[\frac{1}{r \pm \Delta r} - \frac{1}{r} \right] \approx \mp \Delta r \frac{\eta_D \kappa_D}{c_0^2} \frac{Q|q|}{4\pi r^2}. \quad (69)$$

The number of reversed dipoles thus decreases during the separation of C and D in **Figure 5**. The corresponding energy variation with positive q is

$$\delta E_{Q,q}(r, \Delta r) = 2p_D c_0 \delta N_{Q,q}(r, \Delta r) = -\Delta r |q| \frac{Q}{4\pi \varepsilon_0 r^2} < 0, \quad (70)$$

cf. Eq. (65). The energy of the reversed dipoles thus decreases by the amount that fuels the kinetic energy in Eq. (67).

In the opposite case with negative q and attraction, it can be seen from **Figure 6** that the increased number of reversed dipoles is actually leaving the system without momentum exchange and is lost. The momentum difference, therefore, is again negative

$$\delta P_{Q,q}(r, \Delta r) = -2p_D \delta N_{Q,q}(r, \Delta r) \quad (71)$$

and so is the energy of the reversed dipoles confined in the system:

$$\delta E_{Q,q}(r, \Delta r) = \delta P_{Q,q}(r, \Delta r) c_0 = -|q| \Delta r \frac{Q}{4\pi \varepsilon_0 r^2} < 0. \quad (72)$$

The electrostatically bound two-body system thus is a closed system in the sense defined by von Laue [49], slowly evolving in time during the movements of bodies C and D. The potential energy converted into kinetic energy stems from the modified dipole distributions.

3.2 Pioneer anomaly

Anomalous frequency shifts of the Doppler radio-tracking signals were detected for both Pioneer spacecraft [56]. The observations of Pioneer 10 (launched on 2 March 1972) published by the Pioneer Team will be considered during the time interval $t_1 - t_0 \approx 11.55\,\text{years} = 3.645 \times 10^8$ s between 3 January 1987 and 22 July 1998, while the spacecraft was at heliocentric distances between $r_0 = 40$ ua and $r_1 = 70.5$ ua. The Pioneer team took into account all known contributions in calculating a model frequency $\nu_{\text{mod}}(t)$ which was based on a constant clock frequency f_0 at the terrestrial control stations. Observations at times $t = t_0 + \Delta t$ then indicated a nearly uniform increase of the observed frequency shift with respect to the expected one of

$$\nu_{\text{obs}}(t) - \nu_{\text{mod}}(t) = 2\dot{f}\,\Delta t \tag{73}$$

with $\dot{f} = 5.99 \times 10^{-9}$ Hz s^{-1} [57].

The observations of the anomalous frequency shifts could, in principle, be interpreted as a deceleration of the heliocentric spacecraft velocity by

$$a_{\text{p}} = -(8.74 \pm 1.33) \times 10^{-10} \text{ m s}^{-2}. \tag{74}$$

However, no unknown sunward-directed force could be identified [58]. Alternatively, a clock acceleration at the ground stations of

$$a_t = \frac{a_{\text{p}}}{c_0} = (2.92 \pm 0.44) \times 10^{-18} \text{ s}^{-1} \tag{75}$$

could explain the anomaly. A true trajectory anomaly together with an unknown systematic spacecraft effect was considered to be the most likely interpretation by Anderson et al. [59]. Although Turyshev et al. [60] later concluded that thermal recoil forces of the spacecraft caused the anomaly of Pioneer 10, the discussion in the literature continued.

Assuming an atomic clock acceleration, a constant reference frequency f_0 for the calculation of $\nu_{\text{mod}}(t)$ is not appropriate. Consequently, we modified in [61] the equation

$$\left[\nu_{\text{obs}}(t) - f_0\right] - \left[\nu_{\text{mod}}(t) - f_0\right] = 2\dot{f}\,\Delta t, \tag{76}$$

equivalent to Eq. (73) with

$$f(t) = f_0 + \dot{f}\,\Delta t = f_0\left(1 + \frac{\dot{f}}{f_0}\,\Delta t\right) = f_0\left(1 + a_t\,\Delta t\right) \tag{77}$$

and

$$\nu^{*}_{\text{mod}}(t) = \nu_{\text{mod}}(t) + 2\dot{f}\,\Delta t \tag{78}$$

to

$$\left[\nu_{\text{obs}}(t) - \left(f_0 + \dot{f}\,\Delta t\right)\right] - \left[\nu^{*}_{\text{mod}}(t) - \left(f_0 + \dot{f}\,\Delta t\right)\right]$$
$$= [\nu_{\text{obs}}(t) - f(t)] - [\nu^{*}_{\text{mod}}(t) - f(t)] = 0. \tag{79}$$

Our gravitationally impact model [16] summarized in Section 2.4 leads to a secular mass increase of massive particles in Eq. (30). Consequently the Rydberg constant in Eq. (32) would increase in a linear approximation with the electron mass m_e according to

$$R_\infty^*(t) = \frac{\alpha^2 c_0}{2h} m_e (1 + A\,\Delta t) \tag{80}$$

resulting in frequency increases of atomic clocks with time. They give rise to the clock acceleration in Eq. (77), if we assume $a_t = A$. The most likely values of $r_{G,e}$ in **Figure 3** range from 2.04×10^{-4} pm to 2.82 fm, the classical electron radius, corresponding with Eq. (31) to $A_H = 2.43 \times 10^{-18}$ s$^{-1} \approx H_0$, the Hubble constant, and $A \approx 1.3 \times 10^{-20}$ s^{-1}. Within the uncertainty margins, the high value agrees with a_t in Eq. (75) and would quantitatively account for the Pioneer frequency shift. Should the anomaly be much less pronounced, because thermal recoil forces decelerate the spacecraft, the range of $r_{G,e}$ in **Figure 3** could accommodate smaller values of a_t as well.

3.3 Sun-Earth distance increase

A secular increase of the mean Sun-Earth distance with a rate of (15 ± 4) m per century had been reported using many planetary observations between 1971 and 2003 [45]. Neither the influence of cosmic expansion nor a time-dependent gravitational constant seems to provide an explanation [62].

As our impact model summarized in Section 2.4 leads to a secular mass increase according to Eq. (30) of all massive bodies fuelled by a decrease in energy of the background flux of gravitons, it allowed us to formulate a quantitative understanding of the effect within the parameter range of the model [63].

The value of the astronomical unit is defined by the International Astronomical Union (IAU) and the Bureau International des Poids et Mesure [64] as 1 ua = $1.495978707 \times 10^{11}$ m (exact). The mean Sun-Earth distance r_E is known with a standard uncertainty of (3 to 6) m [65–67].

Considering this uncertainty, the measurement of a change rate of

$$\frac{\Delta r_E}{\Delta t} = \frac{(15 \pm 4)\ \text{m}}{3.156 \times 10^9\ \text{s}} = (4.8 \pm 1.3)\ \text{nm}\ \text{s}^{-1} \tag{81}$$

is difficult but feasible as relative determination. A circular orbit approximation had been considered, because the mean value of r_E is of interest:

$$r_E = \frac{G_N M_\odot}{v_E^2} = \frac{\mu_\odot}{v_E^2}. \tag{82}$$

This follows from equating the gravitational attraction, cf. Eq. (1), and the centrifugal force with v_E, the tangential orbital velocity of the Earth, where the heliocentric gravitational constant is $\mu_\odot = 1.32712440042 \times 10^{20}$ m^3 s^{-2} (IAU) and the mass of the Sun $M_\odot = 1.98842 \times 10^{30}$ kg.

We now consider Eq. (82) not only for t_0 but also at $t = t_0 + \Delta t$ assuming constant G_N as well as constant v_E. The latter assumption is justified by the fact that any uniformly moving particle does not experience a deceleration. It implies an increase of the momentum together with the mass accumulation of the Earth. The apparent violation of the momentum conversation principle can be resolved by considering the accompanying momentum changes of the graviton distribution. A detailed discussion of this aspect is given in Section 3 of [16].

From Eqs. (30) and (82), it follows

$$r_\mathrm{E}(t) = r_\mathrm{E} + \Delta r_\mathrm{E} \approx \frac{G_\mathrm{N}}{v_\mathrm{E}^2} M_\odot (1 + A\,\Delta t) \qquad (83)$$

and

$$\frac{\Delta r_\mathrm{E}}{\Delta t} \approx r_\mathrm{E} A. \qquad (84)$$

With the help of Eqs. (31) and (81), the electron mass radius can now be calculated. The result is

$$r_{\mathrm{G},e} = \left(r_\mathrm{E} \frac{\Delta t}{\Delta r_\mathrm{E}}\, 1.014 \times 10^{-49}\ \mathrm{m}^2\ \mathrm{s}^{-1} \right)^{-1/2} = \left(1.8^{+0.4}_{-0.2} \right)\ \mathrm{fm}, \qquad (85)$$

close to the classical electron radius

$$r_e = \alpha^2 a_0 = 2.82\ \mathrm{fm}. \qquad (86)$$

The relative accumulation rate deduced from the observations of r_E finally becomes $A = A_{ua} \approx 3.2 \times 10^{-20}\ \mathrm{s}^{-1}$ (see **Figure 3**).

3.4 Secular perihelion advances in the solar system

Multiple applications of the interaction process described in Section 2.4 can produce gravitons with reduction parameters greater than Y in large mass conglomerations—within the Sun in this section. The proportionality of the linear term in the binomial theorem with the exponent n in

$$(1 - Y)^n \approx 1 - n\,Y \quad \text{for}\ Y \ll 1 \qquad (87)$$

suggests that a linear superposition of the effects of multiple interactions will be a good approximation, if n is not too large. Energy reductions according to Eq. (18) are therefore not lost, as claimed by Drude [21], but they are redistributed to other emission locations within the Sun. This has two consequences: (1) the total energy reduction is still dependent on the solar mass, and (2) since emissions from matter closer to the surface of the Sun in the direction of an orbiting object is more likely to escape into space than gravitons from other locations, the effective gravitational centre should be displaced from the centre of the Sun towards that object.

Using published data on the secular perihelion advances of the inner planets Mercury, Venus, Earth and Mars of the solar system and the asteroid Icarus, we found that the effective gravitational centre is displaced from the centre of the Sun by approximately $\rho = 4400$ m [68]. Since an analytical derivation of this value from the mass distribution of the Sun was beyond the scope of the study, future investigations need to show that the modified process with directed secondary graviton emission can quantitatively account for such a displacement.

3.5 Planetary flyby anomalies

3.5.1 Earth flybys

Several Earth flyby manoeuvres indicated anomalous accelerations and decelerations and led to many investigations without reaching a solution of the problem

(see recent reviews by Anderson et al. [69] and Nieto and Anderson [70]). Since there is general agreement that the anomaly is only significant near perigee, we discuss here the seven passages at altitudes below 2000 km listed in Table 1 of Acedo [71]. Three of them (Galileo I, NEAR and Rosetta) we have studied in [72] assuming the gravitational impact model of Section 2.4 and multiple interactions. As in Section 3.4, the multiple interactions result in a deviation ρ of the effective gravitational centre from the geometric centre. We obtained for Galileo, NEAR and Rosetta $\rho \approx 1.3$ m, 3.9 m and 0.5 m, respectively. The study had been conducted assuming a spherically symmetric emission of liberated gravitons mentioned in Section 2.4.

With the assumption of an *antiparallel* emission, we have repeated the analysis and found $\rho \approx 2$ m for all spacecraft, provided the origin of ρ is shifted by approximately -0.6 m in the direction of the perigee of Galileo I, $+1.9$ m for NEAR and -1.5 m for Rosetta. Moreover, it was possible to model the decelerations of Galileo II on 8 December 1992 with a shift of -3.4 m, of Cassini on 18 August 1999 with -2.7 m and the null result for Juno on 9 October 2013 with -2 m.

An origin offset of $+3.4$ m opposite to the Cassini perigee could to a first approximation achieve all apparent shifts taking the geographic coordinates of the various flybys into account. A detailed study would have to consider in addition the Earth gravitational model.

3.5.2 Juno Jupiter flybys

Juno was inserted into an elliptical orbit around Jupiter on 4 July 2016 with an orbital period of 53.5 days. Acedo et al. [74] studied the first and the third orbit with a periapsis of "4200 km over the planet top clouds". "A significant radial component was found and this decays with the distance to the center of Jupiter as expected from an unknown physical interaction … . The anomaly shows an asymmetry among the incoming and outgoing branches of the trajectory … ". The radial component is shown in their **Figure 6** in the time interval $t = (-180$ to $+180)$ min around perijove for the first and third Juno flyby. The peak anomalous outward accelerations shown are in both cases: $\delta a = 7$ mm s^{-2} at $t \approx -15$ min and $\delta a = 6$ mm s^{-2} at $t \approx +17$ min.

We applied the multiple-interaction concept of the previous Sections 3.4 and 3.5.1 in [75] and found that offsets of $\rho \approx (8$ to $27)$ km of the gravitational from the geometric centre are required to model the acceleration in **Figure 7**, which is in good agreement with the observations during the Juno Jupiter flybys. The variation of ρ could be modelled by an ellipsoidal displacement of the gravitational centre offset in the direction of a flyby position near $t = -10$ min.

3.6 Rotation velocities of spiral galaxies

The rotation velocities of spiral galaxies are difficult to reconcile with the Keplerian motions, if only the gravitational effects of the visible matter are taken into account, cf. [76, 77]. Dark matter had been proposed by Oort [78] and Zwicky [79] in order to understand several velocity anomalies in galaxies and clusters of galaxies. A Modification of the Newtonian Dynamics (MOND) has been introduced by Milgrom [80] that assumes a modified gravitational interaction at low acceleration levels.

The impact model of gravitation in Section 2.4 is applied to the radial acceleration of disk galaxies [81]. The flat velocity curves of NGC 7814, NGC 6503 and M 33 are obtained without the need to postulate any dark matter contribution. The concept explained below provides a physical process that relates the fit parameter of
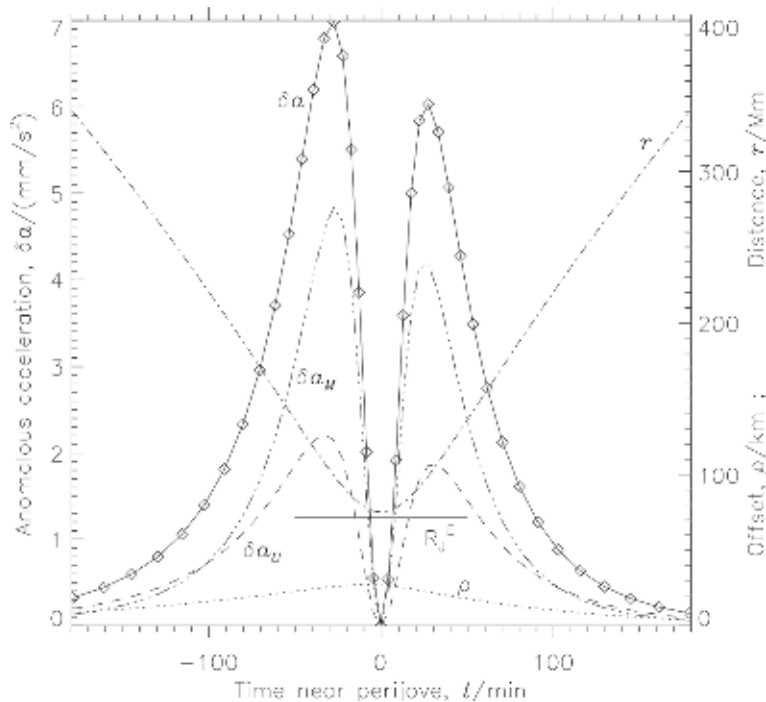
Figure 7.
*Anomalous radial outward acceleration δa experienced by Juno near the perijove at time t = 0 (solid curve with diamond signs). It is composed of δa$_U$ calculated from the adjusted potential and δa$_M$ calculated from the adjusted centrifugal energy (see effective potential energy equation 14 of [73]). A multi-interaction process has been assumed within the mass 1.89858×10^{27} kg of Jupiter. It causes an offset ρ of the effective pivotal point of the gravitational attraction from the geometric centre of Jupiter (dotted curve). Also shown are the equatorial radius of Jupiter R$_J^E$ (solid bar) and the radial distance r of Juno from the centre (dash-dot curve) (**Figure 7** of [75]).*

the acceleration scale defined by McGaugh et al. [82] to the mean-free path length of gravitons in the disks of galaxies. It may also provide an explanation for MOND.

McGaugh [83] has observed a fine balance between baryonic and dark mass in spiral galaxies that may point to new physics for DM or a modification of gravity. Fraternali et al. [84] have also concluded that either the baryons dominate the DM or the DM is closely coupled with the luminous component. Salucci and Turini [85] have suggested that there is a profound interconnection between the dark and the stellar components in galaxies.

The large baryonic masses in galaxies will cause multiple interactions of gravitons with matter if their propagation direction is within the disk. For each interaction the energy loss of the gravitons is assumed to be YT_G (for details see Section 2.3 of [16]). The important point is that the multiple interactions occur only in the galactic plane and not for inclined directions. An interaction model is designed indicating that an amplification factor of approximately two can be achieved by six successive interactions. An amplification occurs for four or more interactions. The process works, of course, along each diameter of the disk and leads to a two-dimensional distribution of reduced gravitons.

The multiple interactions do not increase the total reduction of graviton energy, because the number of interactions is determined by the (baryonic) mass of the gravitational centre according to [16]. A galaxy with enhanced gravitational acceleration in two dimensions defined by the galactic plane will, therefore, have a reduced acceleration in directions inclined to this plane.

3.7 Light deflection and Shapiro delay

The deflection of light near gravitational centres is of fundamental importance. For a beam passing close to the Sun, Soldner [86] and Einstein [87] obtained a deflection angle of 0.87″ under the assumption that radiation would be affected in the same way as matter. *Twice* this value was then derived in the framework of the GTR [2][4] and later by Schiff [88] using the equivalence principle and STR. The high value was confirmed during the total solar eclipse in 1919 for the first time [89]. This and later observations have been summarized by Mikhailov [90] and combined to a mean value of approximately 2″.

The deflection of light has also been considered in the context of the gravitational impact model summarized in Section 2.4. As a secular mass increase of matter was a consequence of this model, the question arises on how the interaction of gravitons with photons can be understood, since the photon mass is in all likelihood zero.[5] An initial attempt at solving that problem has been made in [91], where we assumed that a photon stimulates an interaction with a rate equal to its frequency $\nu = E_\nu / h$. It is summarized here under the assumption of an *antiparallel* re-emission, both for massive particles and photons.

A physical process will then be outlined that provides information on the gravitational potential U at the site of a photon emission [95]. This aspect had not been covered in our earlier paper on the gravitational redshift [96].

Interactions between massive bodies have been treated in [16] with an absorption rate of *half* the intrinsic de Broglie frequency of a mass, because *two* virtual gravitons have to be emitted for one interaction. The momentum transfer to a photon will thus be twice as high as to a massive body with a mass equivalent to E_ν / c_0^2.

We then apply the momentum conservation principle to photon-graviton pairs in the same way as to photons [73] and can write after a reflection of $\boldsymbol{p}_{\mathrm{G}}$

$$\boldsymbol{p}_\nu + \boldsymbol{p}_{\mathrm{G}} = \boldsymbol{p}_\nu + 2\,\boldsymbol{p}_{\mathrm{G}} - \boldsymbol{p}_{\mathrm{G}} = \boldsymbol{p}_\nu^* - \boldsymbol{p}_{\mathrm{G}} \qquad (88)$$

with $|\boldsymbol{p}_{\mathrm{G}}| = p_{\mathrm{G}} = T_{\mathrm{G}}/c_0$.

We assume, applying Eq. (88) with $p_{\mathrm{G}} \ll p_\nu = |\boldsymbol{p}_\nu|$, that under the influence of a gravitational centre relevant interactions occur on opposite sides of a photon with p_{G} and $p_{\mathrm{G}}(1 - Y)$ transferring a net momentum of $2Y p_{\mathrm{G}}$. Note, in this context, that the Doppler effect can only operate for interactions of photons with massive bodies [97, 98]. Consequently, there will be no energy change of the photon, because both gravitons are reflected with constant energies under these conditions, and we can write for a pair of interactions:

$$E_\nu = |\boldsymbol{p}_\nu|c = |\boldsymbol{p}_\nu + 2Y\boldsymbol{p}_{\mathrm{G}}|c' = |\boldsymbol{p}_\nu|c' = E_\nu', \qquad (89)$$

where $\boldsymbol{p}_\nu'$ is the photon momentum after the events. If $\boldsymbol{p}_\nu$ and a component of $2Y\boldsymbol{p}_{\mathrm{G}}$ are pointing in the same direction, it is $c' < c$, the speed is reduced; an antiparallel direction leads to $c' > c$. Note that this could, however, not result in

---

[4] It is of interest in the context of this paper that Einstein employed Huygens' principle in his calculation of the deflection.

[5] A zero mass of photons follows from the STR and a speed of light in vacuum c_0 constant for all frequencies. Einstein [52] used "Lichtquant" for a quantum of electromagnetic radiation; the term "photon" was introduced by Lewis [15]. With various methods the photon mass could be constrained to $m_\nu < 10^{-49}$ kg [92, 93] or even to $m_\nu < 6.3 \times 10^{-53}$ kg [94].

$c' > c_0$, because $c = c_0$ can only be attained in a region with an isotropic distribution of gravitons with a momentum of p_G, i.e. with a gravitational potential $U_0 = 0$.

The momentum $\boldsymbol{p}_\nu$ of a photon radially approaching a gravitational centre will be treated in line with Eq. (6) of [17] for massive bodies, however, with twice the rate of interaction. Since we know from observations that the deflection of light near the Sun is very small, the momentum variation caused by the weak and static gravitational interaction is also very small. The momentum change rate of the photon can then be approximated by

$$\frac{\delta \boldsymbol{p}_\nu}{\Delta t} \approx 2 G_N M_\odot \frac{\hat{r}}{r^2} \frac{p_\nu}{c_0}, \tag{90}$$

where $r = |\boldsymbol{r}|$ is the distance of the photon from the centre, and the position vector of the photon is $r\hat{r}$ with a unit vector $\hat{r}$. The small deflection angle also allows an approximation of the actual path by a straight line along an x axis: $x \approx c_0 t$. The normalized momentum variation along the trajectory then is

$$\frac{\delta p_\nu}{p_\nu} \cos \vartheta \approx \frac{2 G_N M_\odot}{c_0} \frac{x}{r^3} \Delta t. \tag{91}$$

The corresponding component perpendicular to the trajectory is

$$\frac{\delta p_\nu}{p_\nu} \sin \vartheta \approx \frac{2 G_N M_\odot}{c_0} \frac{R}{r^3} \Delta t, \tag{92}$$

where R is the impact parameter of the trajectory. Integration of Eq. (91) over t from $-\infty$ to x/c_0 (for details see [17]) yields

$$\frac{\left[\Delta \boldsymbol{p}_\nu(r)\right]_x}{p_\nu} \approx \frac{2 G_N M_\odot}{c_0^2 r} = \frac{2 G_N M_\odot}{c_0^2 \sqrt{R^2 + x^2}}. \tag{93}$$

If we apply Eq. (89) to a photon approaching the Sun along the x axis starting from infinity with $E_\nu = p_\nu c_0$, and considering that the y component in Eq. (91) is much smaller than the x component in Eq. (92) for $x \gg R$, the photon speed $c(r)$ as a function of r can be determined from

$$p_\nu c_0 \approx \left\{ p_\nu + \left[\Delta \boldsymbol{p}_\nu(r)\right]_x \right\} c(r). \tag{94}$$

Division by p_ν then gives with Eq. (93)

$$\frac{1}{[n_G(r)]_x} = \frac{c(r)}{c_0} \approx 1 - \frac{2 G_N M_\odot}{c_0^2 r} = 1 + \frac{2 U(r)}{c_0^2} \tag{95}$$

as a good approximation of the inverse gravitational index of refraction along the x axis. The same index has been obtained albeit with different arguments, e.g. in [99, 100]. The resulting speed of light is in agreement with evaluations by Schiff [88], for a radial propagation[6] in a central gravitational field, and Okun [101] —calculated on the basis of the standard Schwarzschild metric. A decrease of the speed of light near the Sun, consistent with Eq. (95), is not only supported by the

---

[6] Einstein [108] states explicitly that the speed at a certain location is not dependent on the direction of the propagation.

predicted and subsequently observed Shapiro delay [102–107] but also indirectly by the deflection of light [89].

The deflection of light by gravitational centres according to the GTR [2] and its observational detection by Dyson et al. [89] leave no doubt that a photon is deflected by a factor of two more than the expected relative to a corresponding massive particle. Since in our concept the interaction rate between photons and gravitons is twice as high as for massive particles of the same total energy, the reflection of a graviton from a photon with a momentum of $(1 - Y)p_G$ must also be *antiparallel* to the incoming one, i.e. a momentum of $-2Yp_G$ will be transferred. Otherwise the correct deflection angle for photons cannot be obtained. This modified interaction process has one further important advantage: the reflected graviton can interact with the deflecting gravitational centre and transfers $2Yp_G$—through the process outlined in the paragraph just before Eq. (48)—in compliance with the momentum conservation principle. In the old scheme, the violation of this principle had no observational consequences, because of the extremely large masses of relevant gravitational centres, but the adherence to both the momentum and energy conservation principles is very encouraging and clearly favours the new concept.

Basically the same arguments are relevant for the longitudinal interaction between photons and gravitons. The momentum transfer per interaction will be doubled, but the gravitational absorption coefficient will be reduced by a factor of two. Together with an increased graviton density, all quantities and results are the same as before. However, a detailed analysis shows that the momentum conservation principle is now also adhered to.

3.8 Gravitational redshift

The gravitational potential U at a distance r from a spherical body with mass M is constraint in the weak-field approximation for nonrelativistic cases by

$$-1 \ll \frac{U}{c_0^2} = -\frac{G_N M}{c_0^2 \, r} \leq 0 \qquad (96)$$

cf. [73]. A definition of a reference potential in line with this formulation is $U_\infty = 0$ for $r = \infty$.

The study of the gravitational redshift, predicted for solar radiation by Einstein [109], is still an important subject in modern physics and astrophysics [95, 96, 110–114]. This can be exemplified by two conflicting statements. Wolf et al. [10] write: "The clock frequency is sensitive to the gravitational potential U and not to the local gravity field $g = \nabla U$". Whereas it is claimed by Müller et al. [11]: "We first note that no experiment is sensitive to the absolute potential U".

Support for the first alternative can be found in many publications [49, 88, 95, 96, 109, 115–117], but it is, indeed, not obvious how an atom can locally sense the gravitational potential U. Experiments on Earth, in space and in the Sun-Earth system, cf. [118–123], however, have quantitatively confirmed in the static weak field approximation a relative frequency shift of

$$\frac{\nu - \nu_0}{\nu_0} = \frac{\Delta \nu}{\nu_0} \approx \frac{\Delta U}{c_0^2} = \frac{U - U_0}{c_0^2}, \qquad (97)$$

where ν_0 is the frequency of the radiation emitted by a certain transition at U_0 and ν is the observed frequency there, if the emission caused by the same transition had occurred at a potential U.

Since Einstein discussed the gravitational redshift and published conflicting statements regarding this effect in [2, 87, 109], the confusion could still not be cleared up consistently, cf., e.g. [124, 125]. In most of his publications Einstein defined clocks as atomic clocks. Initially he assumed that the oscillation of an atom corresponding to a spectral line might be an intra-atomic process, the frequency of which would be determined by the atom alone. Scott [126] also felt that the equivalence principle and the notion of an ideal clock running independently of acceleration suggest that such clocks are unaffected by gravity. Einstein [2] later concluded that clocks would slow down near gravitational centres, thus causing a redshift.

The question whether the gravitational redshift is caused by the emission process (case a) or during the transmission phase (case b) is nevertheless still a matter of recent debates. Proponents are, e.g. of (a) Schiff [88], Okun et al. [116], Møller [127], Cranshaw et al. [128] and Ohanian [129], and of (b) Hay et al. [130], Straumann [131], Randall [132] and Will [133]. It is surprising that the same team of experimenters albeit with different first authors published different views in [128, 130] on the process of the Pound-Rebka-Experiment.

Pound and Snider [120] and Pound [134] pointed out that this experiment could not distinguish between the two options, because the invariance of the velocity of the radiation had not been demonstrated.

Einstein [13] emphasized that for an elementary emission process, not only the energy exchange but also the momentum transfer is of importance; see also [12, 46, 97]. Taking these considerations into account, we formulated a photon emission process at a gravitational potential U assuming that:

1. The atom cannot sense the potential U, in line with the original proposal by Einstein [87, 109], and initially emits the same energy ΔE_0 at $U < 0$ and $U_0 = 0$.

2. It also cannot directly sense the speed of light at the location with a potential U. The initial momentum thus is $p_0 = \Delta E_0 / c_0$.

3. As the local speed of light is, however, $c(U) \neq c_0$, a photon having an energy of ΔE_0 and a momentum p_0 is not able to propagate. The necessary adjustments of the photon energy and momentum as well as the corresponding atomic quantities then lead in the interaction region to a redshift consistent with $h\nu = \Delta E_0 \left(1 + U/c_0^2\right)$ and observations [96].

As outlined in Section 3.7, there is general agreement in the literature that the local speed of light is

$$c(U) \approx c_0 \left(1 + \frac{2U}{c_0^2}\right) \tag{98}$$

in line with Eq. (95) in Section 3.7. It has, however, to be noted that the speed $c(U)$ was obtained for a photon propagating from U_0 to U, and, therefore, the physical process which controls the speed of newly emitted photons at a gravitational potential U is not yet established.

An attempt to do that will be made by assuming an aether model. Before we suggest a specific aether model, a few statements on the aether concept in general should be mentioned. Following Michelson and Morley [135] famous experiment, Einstein [51, 109] concluded that the concept of a light aether as carrier of the electric and magnetic forces is not consistent with the STR. In response to critical remarks by Wiechert [136], cf. Schröder [137] for Wiechert's support of the aether,

von Laue [138] wrote that the existence of an aether is not a physical, but a philosophical problem, but later differentiated between the physical world and its mathematical formulation [139]: a four-dimensional "world" is only a valuable mathematical trick; a deeper insight, which some people want to see behind it, is not involved.

In contrast to his earlier statements, Einstein said at the end of a speech in Leiden that according to the GTR, a space without aether cannot be conceived [140] and even more detailed thus one could instead of talking about "aether" as well discuss the "physical properties of space". In theoretical physics we cannot do without aether, i.e. a continuum endowed with physical properties [141]. Michelson et al. [142] confessed at a meeting in Pasadena in the presence of H.A. Lorentz that he clings a little to the aether, and Dirac [143] wrote in a letter to *Nature* that there are good reasons for postulating an aether.

In [17] we proposed an impact model for the electrostatic force based on massless dipoles. The vacuum is thought to be permeated by these dipoles that are, in the absence of electromagnetic or gravitational disturbances, oriented and directed randomly propagating along their dipole axis with a speed of c_0. There is little or no interaction among them. We suggest to identify the dipole distribution postulated in Section 2.5 with an aether. Einstein's aether mentioned above may, however, be more related to the gravitational interactions, cf. [144]. In this case, we have to consider the graviton distribution as another component of the aether.

We now assume that an individual dipole interacts with gravitons in the same way as photons in Eq. (89), i.e. according to

$$T_{\mathrm{D}} = |\boldsymbol{p}_{\mathbf{D}}|c = |\boldsymbol{p}_{\mathbf{D}} + 2Y\boldsymbol{p}_{\mathbf{G}}|c' = |\boldsymbol{p}'_{\mathbf{D}}|c' = T'_{\mathrm{D}}, \qquad (99)$$

where T_{D} and $\boldsymbol{p}_{\mathbf{D}}$ refer to the energy and momentum of a dipole. The condition $p_{\mathrm{D}} \gg p_{\mathrm{G}}$, cf. Eq. (88), is fulfilled in the range from $Y \approx 10^{-22}$ to 10^{-15} for all $r_{\mathrm{e}} \leq 2.82$ fm (see Section 2.5 and **Figure 3**).

We can then modify Eqs. (90)–(94) by changing ν to D and find that Eqs. (95) and (98) are also valid for dipoles with a speed of c_0 for $U_0 = 0$.

Considering that many suggestions have been made to describe photons as solitons, e.g. in [145–150], we also propose that a photon is a soliton propagating in the dipole aether with a speed of $c(U)$, cf. Eq. (98), controlled by the dipoles moving in the direction of propagation of the photon. The dipole distribution thus determines the gravitational index of refraction, cf. Eq. (95), and consequently the speed of light $c(U)$ at the potential U. This solves the problem formulated in relation to Eq. (98) and might be relevant for other phenomena, such as gravitational lensing and the cosmological redshift, cf., e.g. [151]. Should the speculation in Section 2.5.2 be taken seriously that the dipole distribution corresponds to DM, it has to be much more evenly distributed than previously thought [152]. The light deflection would then be caused by gravitationally induced index of refraction variations.

4. Discussion and conclusions

With Newton's law of gravitation as starting point, the ideas presented in Section 2.4 allow an understanding of far-reaching gravitational force between massive particles as local interactions of hypothetical massless gravitons travelling with the speed of light in vacuum. The gravitational attraction leads to a general mass accretion of massive particles with time, fuelled by a decrease of the graviton energy density in space. The physical processes during the conversion of gravitational potential energy into kinetic energy have been described for two bodies with

masses m_A and m_b, and the source of the potential energy could be identified in Section 3.1.1. In order to avoid conflicts with energy and momentum conservation, we had to modify a detail of the interaction process in Eq. (26), i.e. assume an *antiparallel* emission of the secondary graviton with respect to the incoming one.

Multiple interactions of gravitons leading to shifts of the effective gravitational centre of a massive body from the "centre of gravity" are treated in Sections 3.4–3.6 taking the modified concept into account. The interaction of gravitons with photons in Section 3.7 had to be modified as well, but the modification did not change the results, with the exception that now, both the energy and momentum conservation principles are fulfilled.

Our main aim in Section 3.8 was to identify a physical process that leads to a speed $c(U)$ of photons controlled by the gravitational potential U. This could be achieved by postulating an aether model with moving dipoles, in which a gravitational index of refraction $n_G(U) = c_0/c(U)$ regulates the emission and propagation of photons as required by energy and momentum conservation principles. The emission process thus follows Steps (1) to (3) in Section 3.8, where the local speed of light is given by the gravitational index of refraction n. In this sense, the statement that an atom cannot detect the potential U by Müller et al. [11] is correct; the local gravity field g, however, is not controlling the emission process.

A photon will be emitted by an atom with appropriate energy and momentum values, because the local speed of light requires an adjustment of the momentum. This occurs in the interaction region between the atom and its environment as outlined in Step 3.

In the framework of a recently proposed electrostatic impact model in [17], the physical processes related to the variation of the electrostatic potential energy of two charged bodies have been described, and the "source region" of the potential energy in such a system could be identified and is summarized in Section 3.1.2.

Sotiriou et al. [125] made a statement in the context of gravitational theories in "A no-progress report": "[…] it is not only the mathematical formalism associated with a theory that is important, but the theory must also include a set of rules to interpret physically the mathematical laws". With this goal in mind, we have presented our ideas on the gravitational and electrostatic interactions.

Acknowledgements

Author details

Klaus Wilhelm[1†] and Bhola N. Dwivedi[2*†]

1 Max-Planck-Institut für Sonnensystemforschung (MPS), Göttingen, Germany

2 Department of Physics, Indian Institute of Technology (Banaras Hindu University), Varanasi, India

*Address all correspondence to: bnd.app@iitbhu.ac.in

† These authors contributed equally.

IntechOpen

References

[1] Mohr PJ, Newell DB, Taylor BN. CODATA recommended values of the fundamental physical constants: 2014. Reviews of Modern Physics. 2016;**88**: 035009

[2] Einstein A. Die Grundlage der allgemeinen Relativitätstheorie. Annalen der Physik (Leipzig). 1916;**354**: 769-822

[3] Planck M. Zur Theorie der Wärmestrahlung. Annalen der Physik (Leipzig). 1909;**336**:758-768

[4] Wheeler JA, Feynman RP. Classical electrodynamics in terms of direct interparticle action. Reviews of Modern Physics. 1949;**21**(3):425-433

[5] Schwarzschild K. Zur Elektrodynamik. II. Die elementare elektrodynamische Kraft. Nachrichten von der Gesellschaft der Wissenschaften zu Göttingen, Mathematisch-Physikalische Klasse. 1903;**3**:132-141

[6] Lange M. The most famous equation. Journal of Philosophy. 2001;**98**:219-238

[7] von Laue M. Das Relativitätsprinzip. Braunschweig: Friedr. Vieweg & Sohn; 1911

[8] Penrose R. The Road to Reality: A Complete Guide to the Laws of the Universe. New York: Alfred A. Knopf; 2006

[9] Carlip S. Kinetic energy and the equivalence principle. American Journal of Physics. 1998;**66**:409-413

[10] Wolf P, Blanchet L, Bordé CJ, Reynaud S, Salomon C, Cohen-Tannoudji C. Atom gravimeters and gravitational redshift. Nature. 2010;**467**:E1

[11] Müller H, Peters A, Chu S. Müller, Peters & Chu reply. Nature. 2010; **467**:E2

[12] Poincaré H. La théorie de Lorentz et le principe de réaction. Archives Néerlandaises des Sciences Exactes et Naturelles. 1900;**5**:252-278

[13] Einstein A. Zur Quantentheorie der Strahlung. Physikalische Zeitschrift. 1917;**XVIII**:121-128

[14] Compton AH. A quantum theory of the scattering of X-rays by light elements. Physical Review. 1923;**21**: 483-502

[15] Lewis GN. The conservation of photons. Nature. 1926;**118**:874-875

[16] Wilhelm K, Wilhelm H, Dwivedi BN. An impact model of Newton's law of gravitation. Astrophysics and Space Science. 2013; **343**:135-144

[17] Wilhelm K, Dwivedi BN, Wilhelm H. An impact model of the electrostatic force: Coulomb's law revisited. arXiv1403.1489v5. 2014 [Accessed: 26 October 2019]

[18] Fatio de Duilleir N. De la cause de la pesanteur. (Ed. Karl Bopp). Notes and Records of the Royal Society of London. 1949;**6**:125-160

[19] Bopp K. Fatio de Duillier: De la cause de la pesanteur. Schriften der Straßburger Wissenschaftlichen Gesellschaft Heidelberg. 1929;**10**:19-66

[20] Zehe H. Die Gravitationstheorie des Nicolas Fatio de Duillier. Archive for History of Exact Sciences. 1983;**28**:1-23

[21] Drude P. Ueber Fernewirkungen. Annalen der Physik (Leipzig). 1897; **268**(12):I-XLIX

[22] Weinberg S. Photons and gravitons in S-matrix theory: Derivation of charge conservation and equality of

gravitational and inertial mass. Physical Review. 1964;**135**:B1049-B1056

[23] Jackson JD. Classical Electrodynamics. 3rd ed. New York, Chichester, Weinheim, Brisbane, Singapore, Toronto: John Wiley & Sons, Inc; 1999

[24] Jackson JD. Klassische Elektrodynamik. 4. Auflage ed. Berlin, New York: Walter de Gruyter; 2006

[25] Newell DB, Cabiati F, Fischer J, Fujii K, Karshenboim SG, Margolis HS, et al. The CODATA 2017 values of h, e, k, and N_A for the revision of the SI. Metrologia. 2018;**55**:L13-L16

[26] Weizsäcker CFV. Ausstrahlung bei Stößen sehr schneller Elektronen. Zeitschrift für Physik. 1934;**88**:612-625

[27] Yukawa H. On the interaction of elementary particles I. Proceedings of the Physico-Mathematical Society of Japan 3rd Series. 1935;**17**:48-57

[28] Nimtz G, Stahlhofen AA. Universal tunneling time for all fields. Annalen der Physik (Berlin). 2008;**17**:374-379

[29] Mandelstam LI, Tamm IE. The uncertainty relation between energy and time in non-relativistic quantum mechanics. Journal of Physics (USSR). 1945;**9**:249-254

[30] Aharonov Y, Bohm D. Time in the quantum theory and the uncertainty relation for time and energy. Physical Review. 1961;**122**:1649-1658

[31] Hilgevoord J. The uncertainty principle for energy and time. II. American Journal of Physics. 1998; **66**(5):396-402

[32] Bohr N. Discussions with Einstein on epistemological problems in atomic physics. In: Albert Einstein: Philosopher-Scientist. Cambridge: Cambridge University Press; 1949

[33] Low FE, Mende PF. A note on the tunneling time problem. Annals of Physics (N.Y.). 1991;**210**:380-387

[34] Stahlhofen AA, Nimtz G. Evanescent modes are virtual photons. Europhysics Letters. 2006;**76**:189-195

[35] de Broglie L. Ondes et quanta. Comptes Rendus. 1923;**177**:507-510

[36] Schrödinger E. Über die kräftefreie Bewegung in der relativistischen Quantenmechanik. Sitzungsberichte der Preussischen Akademie der Wissenschaften. Physikalisch-Mathematische Klasse. 1930:418-431

[37] Schrödinger E. Zur Quantendynamik des Elektrons, Sitzungsberichte der Preussischen Akademie der Wissenschaften. Physikalisch-Mathematische Klasse. 1931:63-72

[38] Huang K. On the zitterbewegung of the Dirac electron. American Journal of Physics. 1952;**20**:479-484

[39] Hestenes D. The Zitterbewegung interpretation of quantum mechanics. Foundations of Physics. 1990;**20**: 1213-1232

[40] Einstein A. Ist die Trägheit eines Körpers von seinem Energieinhalt abhängig? Annalen der Physik (Leipzig). 1905;**323**:639-641

[41] Fahr H-J, Heyl M. Cosmic vacuum energy decay and creation of cosmic matter. Naturwissenschaften. 2007;**94**: 709-724

[42] Fahr H-J, Siewert M. Local spacetime dynamics, the Einstein-Straus vacuole and the Pioneer anomaly: A new access to these problems. Zeitschrift für Naturforschung. 2007;**62a**:117-126

[43] Fahr H-J. Universum ohne Urknall. Kosmologie in der Kontroverse.

Spektrum Akademischer Verlag: Berlin, Heidelberg, Oxford; 1995

[44] Beck C, Mackey MC. Could dark energy be measured in the lab? Physics Letters B. 2005;**605**:295-300

[45] Krasinsky GA, Brumberg VA. Secular increase of astronomical unit from analysis of the major planet motions, and its interpretation. Celestial Mechanics and Dynamical Astronomy. 2004;**90**:267-288

[46] Abraham M. Prinzipien der Dynamik des Elektrons. Annalen der Physik (Leipzig). 1902;**315**:105-179

[47] Wilhelm K, Dwivedi BN. On the potential energy in a gravitationally bound two-body system. New Astronomy. 2015;**34**:250-252

[48] Brillouin L. The actual mass of potential energy, a correction to classical relativity. Proceedings of the National Academy of Sciences. 1965;**53**:475-482

[49] von Laue M. Zur Theorie der Rotverschiebung der Spektrallinien an der Sonne. Zeitschrift für Physik. 1920; **3**(5):389-395

[50] Wilhelm K, Dwivedi BN. On the potential energy in a gravitationally bound two-body system with arbitrary mass distribution. arXiv:1502.05662v2. 2015 [Accessed: 26 October 2019]

[51] Einstein A. Zur Elektrodynamik bewegter Körper. Annalen der Physik (Leipzig). 1905;**322**:891-921

[52] Einstein A. Über einen die Erzeugung und Verwandlung des Lichtes betreffenden heuristischen Gesichtspunkt. Annalen der Physik (Leipzig). 1905;**322**:132-148

[53] Okun LB. Mass versus relativistic and rest masses. American Journal of Physics. 2009;**77**:430-431

[54] Hund F. Theoretische Physik. Band 2, 3. Auflage. Stuttgart: B.G. Teubner Verlagsgesellschaft; 1957

[55] Wilhelm K, Dwivedi BN. On the potential energy in an electrostatically bound two-body system. arXiv: 1501.05615. 2014 [Accessed: 30 October 2019]

[56] Anderson JD, Laing PA, Lau EL, Liu AS, Nieto MM, Turyshev SG. Indication, from Pioneer 10/11, Galileo, and Ulysses data, of an apparent anomalous, weak, long-range acceleration. Physical Review Letters. 1998;**81**:2858-2861

[57] Turyshev SG, Toth VT, Kellogg LR, Lau EL, Lee KJ. A study of the Pioneer anomaly: New data and objectives for new investigation. International Journal of Modern Physics D. 2006;**15**(01):1-55

[58] Iorio L. Can the pioneer anomaly be of gravitational origin? A phenomenological answer. Foundations of Physics. 2007;**37**:897-918

[59] Anderson JD, Laing PA, Lau EL, Liu AS, Nieto MM, Turyshev SG. Study of the anomalous acceleration of Pioneer 10 and 11. Physical Review D. 2002;**65**: 082004

[60] Turyshev SG, Toth VT, Kinsella G, Lee S-C, Lok SM, Ellis J. Support for the thermal origin of the Pioneer anomaly. Physical Review Letters. 2012;**108**: 241101

[61] Wilhelm K, Dwivedi BN. An explanation of the pioneer anomaly in the framework of a gravitational impact model. Astrophysics and Space Sciences Transactions. 2011;**7**:487-494

[62] Lämmerzahl C, Preuss O, Dittus H. Is the physics within the solar system really understood? In: Dittus H, Lämmerzahl C, Turyshev SG, editors. Lasers, Clocks and Drag-free Control: Exploration of Relativistic Gravity in

Space. Vol. 349. Astrophysics and Space Science Library; 2008. pp. 75-101

[63] Wilhelm K, Dwivedi BN. Increase of the mean Sun-Earth distance caused by a secular mass accumulation. Astrophysics and Space Science. 2013; **347**:41-45

[64] Bureau International des Poids et Mesures, Le Système International d'Unités (SI), 8e éd. Sèvres: BIPM; 2014

[65] Pitjeva EV, Standish EM. Proposals for the masses of the three largest asteroids, the Moon-Earth mass ratio and the astronomical unit. Celestial Mechanics and Dynamical Astronomy. 2009;**103**:365-372

[66] Anderson JD, Nieto MM. Astrometric solar-system anomalies. Relativity in fundamental astronomy: Dynamics, reference frames, and data analysis. Proceedings of the International Astronomical Union, IAU Symposium. 2010;**261**:189-197

[67] Harmanec P, Prša A. The call to adopt a nominal set of astrophysical parameters and constants to improve the accuracy of fundamental physical properties of stars. PASP. 2011;**123**: 976-980

[68] Wilhelm K, Dwivedi BN. Secular perihelion advances of the inner planets and asteroid Icarus. New Astronomy. 2014;**31**:51-55

[69] Anderson JD, Campbell JK, Ekelund JE, Ellis J, Jordan JF. Anomalous orbital-energy changes observed during spacecraft flybys of Earth. Physical Review Letters. 2008; **100**:091102

[70] Nieto MM, Anderson JD. Earth flyby anomalies. Physics Today. 2009; **62**:76-77

[71] Acedo L. The flyby anomaly: A multivariate analysis approach.

Astrophysics and Space Science. 2017; **362**:42

[72] Wilhelm K, Dwivedi BN. Anomalous Earth flybys of spacecraft. Astrophysics and Space Science. 2015; **358**:18

[73] Landau LD, Lifshitz EM. Course of Theoretical Physics. Vol. 1. Mechanics. 3rd ed. Oxford, New York, Toronto, Sydney, Paris, Frankfurt: Pergamon Press; 1976

[74] Acedo L, Piqueras P, Moraño JA. A possible flyby anomaly for Juno at Jupiter. Advances in Space Research. 2018;**61**:2697-2706

[75] Wilhelm K, Dwivedi BN. Impact models of gravitational and electrostatic forces: Potential energies, atomic clocks, gravitational anomalies and redshift. arXiv: 1804.04010. 2018 [Accessed: 30 October 2019]

[76] Rubin VC. Dark matter in spiral galaxies. Scientific American. 1983;**248**: 96-106

[77] Rubin VC. Dark matter in the Universe. Highlights of Astronomy. 1986;**7**:27-38

[78] Oort JH. The force exerted by the stellar system in the direction perpendicular to the galactic plane and some related problems. Bulletin of the Astronomical Institutes of the Netherlands. 1932;**6**:249-287

[79] Zwicky F. Die Rotverschiebung von extragalaktischen Nebeln. Helvetica Physica Acta. 1933;**6**:110-127

[80] Milgrom M. A modification of the Newtonian dynamics as a possible alternative to the hidden mass hypothesis. Astrophysical Journal. 1983; **270**:365-370

[81] Wilhelm K, Dwivedi BN. A physical process of the radial acceleration of disc

galaxies. Monthly Notices of the Royal Astronomical Society. 2018;**474**: 4723-4729

[82] McGaugh SS, Lelli F, Schombert JM. Radial acceleration relation in rotationally supported galaxies. Physical Review Letters. 2016;**117**:201101

[83] McGaugh SS. Balance of dark and luminous mass in rotating galaxies. Physical Review Letters. 2005;**95**:171302

[84] Fraternali F, Sancisi R, Kamphuis P. A tale of two galaxies: Light and mass in NGC 891 and NGC 7814. Astronomy & Astrophysics. 2011;**531**:A64

[85] Salucci P, Turini N Evidences for collisional dark matter in galaxies? arXiv: 1707.01059. 2017 [Accessed: 26 October 2019]

[86] Soldner J. Ueber die Ablenkung eines Lichtstrals von seiner geradlinigen Bewegung durch die Attraktion eines Weltkörpers, an welchem er nahe vorbei geht. Berliner Astronomisches Jahrbuch. 1804;**1804**:161-172

[87] Einstein A. Über den Einfluß der Schwerkraft auf die Ausbreitung des Lichtes. Annalen der Physik (Leipzig). 1911;**340**:898-908

[88] Schiff LI. On experimental tests of the general theory of relativity. American Journal of Physics. 1960;**28**: 340-343

[89] Dyson FW, Eddington AS, Davidson C. A determination of the deflection of light by the Sun's gravitational field, from observations made at the total eclipse of May 29, 1919. Philosophical Transactions of the Royal Society of London A. 1920;**220**: 291-333

[90] Mikhailov AA. The deflection of light by the gravitational field of the Sun. Monthly Notices of the Royal Astronomical Society. 1959;**119**:593-608

[91] Wilhelm K, Dwivedi BN. Gravity, massive particles, photons and Shapiro delay. Astrophysics and Space Science. 2013;**343**:145-151

[92] Goldhaber AS, Nieto MM. Terrestrial and extraterrestrial limits on the photon mass. Reviews of Modern Physics. 1971;**43**:277-296

[93] Amsler C, Doser M, Antonelli M, et al. Review of particle physics. Physics Letters B. 2008;**667**:1-1340

[94] Yang Y-P, Zhang B. Tight constraint on photon mass from pulsar spindown. Astrophysical Journal. 2017;**842**:23

[95] Wilhelm K, Dwivedi BN. Gravitational redshift and the vacuum index of refraction. Astrophysics and Space Science. 2019;**364**(2)id.26

[96] Wilhelm K, Dwivedi BN. On the gravitational redshift. New Astronomy. 2014;**31**:8-13

[97] Fermi E. Quantum theory of radiation. Reviews of Modern Physics. 1932;**4**:87-132

[98] Sommerfeld A. Optik. Verlag Harri Deutsch: Thun, Frankfurt/Main; 1978

[99] Boonserm P, Cattoen C, Faber T, Visser M, Weinfurtner S. Effective refractive index tensor for weak-field gravity. Classical and Quantum Gravity. 2005;**22**:1905-1916

[100] Ye X-H, Lin Q. Gravitational lensing analysed by the graded refractive index of a vacuum. Journal of Optics A: Pure and Applied Optics. 2008;**10**(7):075001

[101] Okun LB. Photons and static gravity. Modern Physics Letters A. 2000;**15**:1941-1947

[102] Shapiro II. Fourth test of general relativity. Physical Review Letters. 1964;**13**:789-791

[103] Reasenberg RD, Shapiro II, MacNeil PE, Goldstein RB, Breidenthal JC, Brenkle JP, et al. Viking relativity experiment: Verification of signal retardation by solar gravity. Astrophysical Journal. 1979;**234**:L219-L221

[104] Shapiro II, Ash ME, Ingalls RP, Smith WB, Campbell DB, Dyce RB, et al. Fourth test of general relativity: New radar result. Physical Review Letters. 1971;**26**:1132-1135

[105] Kramer M, Stairs IH, Manchester RN, et al. Tests of general relativity from timing the double pulsar. Science. 2006;**314**:97-102

[106] Ballmer S, Márka S, Shawhan P. Feasibility of measuring the Shapiro time delay over meter-scaled distances. Classical and Quantum Gravity. 2010;**27**:185018-185011

[107] Kutschera M, Zajiczek W. Shapiro effect for relativistic particles—Testing general relativity in a new window. Acta Physica Polonica B. 2010;**41**:1237-1246

[108] Einstein A. Lichtgeschwindigkeit und Statik des Gravitationsfeldes. Annalen der Physik (Leipzig). 1912;**343**:355-369

[109] Einstein A. Über das Relativitätsprinzip und die aus demselben gezogenen Folgerungen. Jahrbuch der Radioaktivität und Elektronik. 1907;**1908**(4):411-462

[110] Kollatschny W. AGN black hole mass derived from the gravitational redshift in optical lines

[111] Negi PS. An upper bound on the energy of a gravitationally redshifted electron-positron annihilation line from the Crab pulsar. Astronomy & Astrophysics. 2005;**431**:673-677

[112] Lämmerzahl C. What determines the nature of gravity? A phenomenological approach. Space Science Reviews. 2009;**148**:501-522

[113] Pasquini L, Melo C, Chavero C, Dravins D, Ludwig H-G, Bonifacio P, et al. Gravitational redshifts in main-sequence and giant stars. Astronomy & Astrophysics. 2011;**526**:A127

[114] Turyshev SG. Testing fundamental gravitation in space. Nuclear Physics B (Proceedings Supplement). 2013;**243**:197-202

[115] Will CM. Gravitational red-shift measurements as tests of nonmetric theories of gravity. Physical Review D. 1974;**10**:2330-2337

[116] Okun LB, Selivanov KG, Telegdi VL. On the interpretation of the redshift in a static gravitational field. American Journal of Physics. 2000;**68**:115-119

[117] Sinha S, Samuel J. Atom interferometry and the gravitational redshift. Classical and Quantum Gravity. 2011;**28**:145018-1-145018-8

[118] Pound RV, Rebka GA. Gravitational red-shift in nuclear resonance. Physical Review Letters. 1959;**3**:439-441

[119] Krause IY, Lüders G. Experimentelle Prüfung der Relativitätstheorie mit Kernresonanzabsorption. Naturwissenschaften. 1961;**48**:34-36

[120] Pound RV, Snider JL. Effect of gravity on gamma radiation. Physical Review. 1965;**140**:788-803

[121] Vessot RFC, Levine MW, Mattison EM, Blomberg EL, Hoffman TE, Nystrom GU, et al. Test of relativistic gravitation with a space-borne hydrogen maser. Physical Review Letters. 1980;**45**:2081-2084

[122] LoPresto JC, Schrader C, Pierce AK. Solar gravitational redshift from the

infrared oxygen triplet. Astrophysical Journal. 1991;**376**:757-760

[123] Takeda Y, Ueno S. Detection of gravitational redshift on the solar disk by using iodine-cell technique. Solar Physics. 2012;**281**:551-575

[124] Mannheim PD. Alternatives to dark matter and dark energy. Progress in Particle and Nuclear Physics. 2006; **56**:340-445

[125] Sotiriou TP, Liberati S, Faraoni V. Theory of gravitation theories: A no-progress report. International Journal of Modern Physics D. 2008;**17**:399-423

[126] Scott RB. Teaching the gravitational redshift: Lessons from the history and philosophy of physics. Journal of Physics: Conference Series. 2015;**600**:012055

[127] Møller C. On the possibility of terrestrial tests of the general theory of relativity. Nuovo Cimento. 1957;**6**: 381-398

[128] Cranshaw TE, Schiffer JP, Whitehead AB. Measurement of the gravitational red shift using the Mössbauer effect in Fe^{57}. Physical Review Letters. 1960;**4**:163-164

[129] Ohanian HC. Gravitation and Spacetime. New York: W.W. Norton; 1976

[130] Hay HJ, Schiffer JP, Cranshaw TE, Egelstaff PA. Measurement of the red shift in an accelerated system using the Mössbauer effect in Fe^{57}. Physical Review Letters. 1960;**4**:165-166

[131] Straumann N. General Relativity with Applications to Astrophysics. Berlin, Heidelberg, New York: Springer-Verlag; 2004

[132] Randall L. Verborgene Universen. 4. Auflage. Frankfurt/Main: S. Fischer Verlag GmbH; 2006

[133] Will CM. The confrontation between general relativity and experiment. Living Reviews in Relativity. 2014;**17**(4):1-117 [Accessed: 27 October 2019]

[134] Pound RV. Weighing photons. Classical and Quantum Gravity. 2000; **17**:2303-2311

[135] Michelson AA, Morley EW. On the relative motion of the Earth and of the luminiferous ether. Sidereal Messenger. 1887;**6**:306-310

[136] Wiechert E. Relativitätsprinzip und Äther. Physikalische Zeitschrift. 1911;**12**: 689-707, 737-758

[137] Schröder W. Ein Beitrag zur frühen Diskussion um den Äther und die Einsteinsche Relativitätstheorie. Annalen der Physik. 1990;**502**:475-489

[138] von Laue M. Zwei Einwände gegen die Relativitätstheorie und ihre Widerlegung. Physikalische Zeitschrift. 1912;**XIII**:118-120

[139] von Laue M. Geschichte der Physik. 4. erweiterte. Auflage. Ullstein Taschenbücher-Verlag: Frankfurt/Main; 1959

[140] Einstein A. Äther und Relativitätstheorie, Rede gehalten am 5. Mai 1920 an der Reichs-Universität zu Leiden. Berlin: Verlag von Julius Springer; 1920

[141] Einstein A. Über den Äther. Verhandlungen der Schweizerischen Naturforschenden. Gesellschaft. 1924; **105**:85-93

[142] Michelson AA, Lorentz HA, Miller DC, Kennedy RJ, Hedrick ER, Epstein PS. Conference on the Michelson-Morley experiment held at Mount Wilson, February, 1927. Astrophysical Journal. 1928;**68**:341-402

[143] Dirac PAM. Is there an æther? Nature. 1951;**168**:906-907

[144] Granek G. Einstein's ether: F. Why did Einstein come back to the ether? Apeiron. 2001;**8**:19-28

[145] Dirac PAM. The quantum theory of the emission and absorption of radiation. Proceedings of the Royal Society of London. Series A. 1927;**114**: 243-265

[146] Vigier JP. Explicit mathematical construction of relativistic nonlinear de Broglie waves described by three-dimensional (wave and electromagnetic) solitons "piloted" (controlled) by corresponding solutions of associated linear Klein-Gordon and Schrödinger equations. Foundations of Physics. 1991;**21**:125-148

[147] Kamenov P, Slavov B. The photon as a soliton. Foundations of Physics Letters. 1998;**11**:325-342

[148] Meulenberg A. The photonic soliton. SPIE Conference Proceedings. 2013;**8832**:88320M

[149] Bersons I. Soliton model of the photon. Latvian Journal of Physics and Technical Sciences. 2013;**50**:60-67

[150] Bertotti B, Iess L, Tortora P. A test of general relativity using radio links with the Cassini spacecraft. New Astronomy. 2003;**425**:374-376

[151] Ellis RS. Gravitational lensing: A unique probe of dark matter and dark energy. Philosophical Transactions of The Royal Society A: Mathematical, Physical and Engineering Sciences. 2010;**368**:967-987

[152] Hildebrandt H, Viola M, Heymans C, Joudaki S, Kuijken K, the KIDS collaboration. KiDS-450: Cosmological parameter constraints from tomographic weak gravitational lensing. Monthly Notices of the Royal Astronomical Society. 2017;**465**: 1454-1498

Section 3

Computational Musings

Generic Computing-Assisted Geometric Search for Human Design and Origins

Ayodele Abiola Periola

Abstract

Scientific space research aims to investigate human origins and provide explanation on how life originated on the earth. This has led to the emergence of theories such as the Panspermia theory. The Panspermia theory opines that life originated from extra-terrestrial sources. However, the Panspermia theory does not consider the influence of cognition and intelligence in microorganisms that are thought to seed life on the earth. However, it is feasible to consider intelligent microorganisms as determining the life-forms that can arise from different cell aggregations. This chapter considers that the pre-determination of the geometry of this feasible life-forms that takes place in Mars's meteorites. The discussion in this chapter proposes the Mars geometric Panspermia theory which is hinged on this perspective. The chapter presents the conceptual perspective for the Mars geometric Panspermia theory. It also presents network architecture and a data acquisition strategy suitable for capital constrained organizations. The capital constrained organizations are space organizations in developing countries. The low cost acquisition strategy proposes the use of open source software and hardware for components used in Mars exploration missions. In addition, the chapter proposes rover data sharing to enable capital constrained space organizations to execute their science objectives in Mars's space missions.

Keywords: human origins, computing search, light, design, computing resources

1. Introduction

The quest to understand human origins is a significant factor that propels the conduct of scientific research in space. This quest is been sustained by advances in space exploration technology. Advances in space exploration technology have made it possible to increase human understanding of the origins of the universe with improved ability to understand events such as the Big Bang. The Big Bang is considered to be the epoch that led to the beginning of the universe [1–3]. The emergence of the Big Bang theory has led to the necessity of conducting a search to find supporting evidence.

Besides, the quest to understand the evolution of the universe; there is also an interest in understanding human evolution. The concept of evolution has been considered to play a crucial role in the emergence of modern humans. Humans and the universe share a common trait in their emergence and continued existence. This

common trait is seen in the role that light plays in the role of the evolution of the universe and humans. The role of light is less appreciated in the evolution of humans than in the universe. This is because of the significant effort and the duration that has been invested in studying the role of light photons in the universe. The role of photons in a scientific study of the universe can be seen in domains such as optical astronomy [4]. Photons also play an important role in humans as seen in the existence of bio-photons [5–7]. Therefore, light has played an important role in human evolution too.

The notion created by the concept of the Big Bang as being the first event in the universe is that the universe first emerged and that humans appeared and evolved at a later epoch. The implication of this notion is that the existence of the universe is thought to precede human appearance and continued evolution. This does not consider the perspective that human evolution can have an extra-terrestrial influence. However, the alternative perspective presented in the Panspermia theory considers that human evolution has an extra-terrestrial influence. The incorporation of an extra-terrestrial influence on human evolution implies that evolutionary actions influencing the emergence of the universe and humans could have evolved at the same epoch. Such a perspective is supported by the Panspermia theory.

The Panspermia theory presented is of the opinion that life was seeded in outer space [8–11]. Though, there is an argument against the Panspermia theory [12], the theory should not be discarded. This is because of the possibility of the extinction of biological life in outer space making these challenging to observe in comparison to the ability to directly observe life-forms on the earth.

The discussion here proposes that the aggregation of life-forms leaves a geometric trace in outer-space. This perspective differs from the theory underlying the Panspermia theory that has motivated astrobiology research. The discussion in this chapter considers that the observation of life forms can be done from two lenses. These lenses are those of geometry traces associated with life-forms and that of biology. The consideration of the geometry traces associated with life-forms provides an opportunity to design a paradigm suitable for investigating the validity of the Panspermia theory from the geometrical perspective. The novel perspective being presented proposes that geometry traces associated with life-forms are present in the extra-terrestrial environment. These traces constitute the evidence of life originating from outer-space as advocated in the Panspermia theory.

The contribution of this chapter is twofold. The first contribution is that the chapter presents the Mars geometrical Panspermia theory as an alternative paradigm for investigating the emergence of humans. The Mars geometrical Panspermia theory advocates that geometrical traces emerging from different aggregation patterns of life forms are present in the meteorites on Mars. The aggregation is considered feasible because Mars can support simple life forms such as Bacteria.

The chapter's second contribution is the design of low cost network architecture for conducting Mars exploration missions aimed at verifying the Mars geometrical Panspermia theory. The low cost network is intended for use by space organizations in developing nations. These space organizations being considered are those with limited capital and limited space engineering capacities.

The remainder of this chapter is organized as follows. Section 2 discusses the background and existing work. Section 3 presents a mathematical framework describing the Martian geometric Panspermia theory. Section 4 describes the proposed Mars based geometric Panspermia theory. Section 5 focuses on the proposed low cost network architecture. Section 6 concludes the chapter.

2. Background and existing work

Mars has been considered as a suitable location that can be studied to increase human knowledge on the existence of extra-terrestrial life [13]. This is because Mars shows patterns of planetary evolution and climate change. Mars exploration is also appealing because Mars is accessible to Spacecraft launched from earth. Several research groups have been established aiming to engage in Mars exploration missions. Two research groups in this regard are the Mars Exploration Program Analysis Group (MEPAG) and the outer planet assessment group (OPAG).

Johnson et al. [14] discuss MEPAG's Mars exploration initiative. It is recognised that a successful Mars exploration campaign requires the development of technology across multi-disciplinary domains. The required technical capabilities comprise: (1) Mars surface access at different altitude and elevations, (2) Mars environment characterisation, (3) life detection and (4) age dating. Environment characterisation requires the dynamic evaluation of chemical and isotopic compositions at various locations on Mars. The realization of these tasks in a Mars exploration mission requires the design and launch of instrumentation on Mars rovers.

Mars exploration missions aim to analyse Mars's environment and probe its composition. The composition of Mars can be found in two types of records [13]. These are the chemical record and physical record. Each record targets the detection of a different type of bio-signature. The physical record refers to the analysis of the weather and climate in the environment of the planet Mars. The chemical record refers to organic compounds that enable the support of biological mechanisms in terrestrial life. In addition, deployed Mars exploration vehicles search for an evidence of a life supporting climate.

The detection of elements belonging to the bio-signature in either physical or chemical record requires the use of appropriate instrumentation. Suitable instrumentation is also required to obtain information from a Mars exploration mission. The choice of instrumentation technology is determined by the science case.

The discussion in [14] focuses on the components of a Mars exploration campaign. It presents a hierarchy of the objectives enabling the realization of the science goal for a Mars exploration mission. Though the role of advanced instrumentation is recognised; algorithms, theories and perspectives that can motivate the design of advanced instrumentation have not been presented.

The choice of instrumentation is also influenced by the sample return expected from a Mars exploration mission. Mars missions can be classified as Mars return sample missions and non-Mars return sample missions. The Mars return sample mission aims to deploy Mars vehicles that take samples from Mars and brings them to earth for further analysis. The sample(s) is the deliverable in the Mars return sample missions. Non-Mars sample return missions are those in which the deployed Mars vehicle aims to execute analysis on Mars and obtain results. The results are relayed to the earth via an integrated telecommunications system for further analysis.

The discussion in [13, 14] describes the objectives of the MEPAG in 2009. It is important to consider how changes in science case influence the instrumentation and the goals of Mars exploration missions. This is because of changing interests in the outer space exploration and how technology advancement influence Mars exploration missions. A change that has occurred in Mars exploration is an increase in the number of space agencies seeking to participate in Mars exploration missions [15]. Another change arises due to technological advancements leading to the use of small satellites in Mars exploration missions. The emergence of small satellites has

led to their use in Mars exploration missions. In this case, small satellite is dependent on the science case definition.

The outcomes of a space exploration for a defined science case can be classified into four categories [16]. These outcomes would be that the location or body in outer space is inhabitable, probably habitable, habitable and inhabited [16]. A motive to categorize any location as being described by any of these four outcomes is dependent on the science case and the instruments aboard the exploration vehicle. This can be seen in the case of the Europa Lander project aimed at surveying the Jovian moon, Europa [16]. The Europa Lander aims to determine the habitability of Europa and investigate its surface properties and dynamics. The instrumentation enabling the acquisition of Europa's samples aboard the Europa Lander are the sample ingestion port, and the context remote sensing instrument package.

The discussion in [17] extends [13–16] by raising the question of the utility that can be derived from Martian samples obtained in Mars sample return missions. The use of randomly acquired samples from Mars is insufficient to answer the queries as regards the origin of life on Mars and other locations such as the Jovian moon, Europa. The use of sample heterogeneity is thereby proposed. Sample heterogeneity refers to the acquisition of samples from different locations on Mars or in Europa. The incorporation of sample heterogeneity enables the acquisition of Mars samples from different locations on Mars. These samples are returned to earth for future analysis. The transport of samples from Mars to earth is done in such a manner that the contamination of earth by these Martian samples is prevented. The assurance that Mars samples pose no contamination risk to earth is handled by the space agency coordinating the Mars exploration missions. The National Aeronautics and Space Administration (NASA) is an example of a space agency that can play this role.

The study in [17] aims to study Mars's environment in the view of the M-2020 mission. The intended study is with the following aims. The first aim is analysing the geological processes (with emphasis on determining the role of water). The second is evaluating the biological history of Mars. The third is determining Mars's evolutionary timeline. The fourth is determining relations between components in Mars's geological system. The fifth is to acquire samples enabling the reconstruction of the processes that have influenced the Martian dynamo. The sixth is quantifying human risks associated with Mars exploration.

The discussion in [13–16] shows that bio-signatures are important for the conduct of outer space missions searching for evidence of extra-terrestrial life. The search and successful detection of bio-signatures are important for Mars exploration missions [13–15] and the Europa Lander project [16]. The category of bio-signature being sought influences the composition of the deployed instrument payload. The approach in [13–19] assumes that a planet or outer space location where the evidence of life is being sought must have bio-signature(s). Therefore, the search for extra-terrestrial life in the environment of outer space is hinged on the existence of the bio-signature.

However, bio-signature existence in outer space locations is threatened because space exploration vehicles can be contaminated with microbes. This contamination can take place on earth prior to launch. The resulting contamination can cause the deployed instrumentation payload to detect earth originating microbes or microorganisms in outer space. This leads to a wrong conclusion as regards the detection of extra-terrestrial life. In addition, such planetary contamination could render a given location or body in outer space infeasible for searching for extra-terrestrial life. Therefore, planets should be protected against microbial contamination. This concern has led to the emergence of planetary protection.

Bio-signature preservation is important for the success of detecting extra-terrestrial life in Mars exploration missions. The detection of bio-signatures can be used to determine the absence or presence of life on Mars in Mars exploration missions [20]. Hays et al. in [20] note that the presence of bio-signatures and their subsequent detection is important for the success of Mars exploration missions. It is also important to ensure that Mars missions preserve existing bio-signatures that can be found on Mars.

The preservation and improved understanding of bio-signature can be achieved by using Analog terrestrial Mars environments. Hays et al. [20] recognize the usefulness and suitability of Analog terrestrial Mars environments. Analog terrestrial Mars environments enable the conduct of low cost investigation for the presence of life on Mars. The use of analog terrestrial Mars environments enables scientists to understand relations between different bio-signatures. This is important in determining the cues to be searched for in Mars exploration missions such that planetary contamination is prevented.

Moreover, the use of analog terrestrial Mars environment enables developing nations to participate in Mars exploration studies. In this role, analog terrestrial Mars environment can be used as low cost alternative prior to actual outer space exploration. This helps developing nations in making better decisions as regards achieving planetary protection. However, this has not been explored in [20].

The potential bio-signatures that can be detected in a Mars exploration mission are dependent on the defined science case. Six classes of bio-signatures have been identified by the Mars 2020 science definition team [20]. These are organic molecules, minerals, macro structures, chemistry and isotopes. The detection of any potential bio-signature in a given class enables the realization of the objectives of an outer space project investigating the occurrence of extra-terrestrial life.

The critical role that bio-signatures play in Mars exploration missions makes it important that bio-signatures are protected from threats to their continued existence. This concern is recognised in [20, 21]. The need to protect bio-signatures has led to the need to design planetary protection strategies to protect Mars from bio-signature contamination. It is recognized that Mars environment provides some native protection to prevent the total erasure of bio-signature, i.e., bio-signature contamination.

The protection capability of planetary protection strategies can be enhanced by enacting policies matched with technological developments. These technological developments ensure bio-signature preservation. Inter-planetary protection is needed in two roles. These are the forward prevention role and the backward prevention role. In the forward protection role, planetary preservation and contamination preservation ensures that microbes are not taken from earth into Mars. The backward preservation role is important for Mars sample return missions. It ensures that samples being brought from Mars are not contaminated on their way to the location where further analysis will be carried out [10].

The forward protection role can be realized by sterilizing Mars exploration vehicles. Sterilization of Mars exploration vehicles ensures that the search for extra-terrestrial life is not compromised by earth originating microbes [22]. Sterilization also ensures that disease causing microbes are not brought to the earth by Mars exploration vehicles in Mars sample return missions.

However, planetary protection strategies are rarely ideal and a 100% protection is not readily achieved. In addition, planetary protection procedures are expensive and influenced by the science case associated with a Mars exploration campaign [22]. The non-ideal performance implies that the chance of detecting pristine bio-signatures might be slightly diminished. Therefore, the non-ideal performance of planetary protection via sterilization constitutes a source of interference to

bio-signature detection. The effect of interference as observed here also affects the conduct of radio astronomy in the form of radio interference. This has received attention [23, 24]. The interference challenge posed by non-ideal sterilization can be addressed by finding another marker that can signify the presence or occurrence of life in Mars. This is important to ensure the realization of Mars exploration mission.

3. Mars geometrical Panspermia theory: concept and analysis

The discussion in this section presents the human evolutionary perspective and origins of the universe as being considered in the proposed Mars geometrical Panspermia theory. The discussion in this section is divided into two parts. The first part presents the underlying concept in the proposed Mars geometrical Panspermia theory. This part considers geometry as being associated with the activities of organics describing the aggregates of cell components. The geometry associated with activities leading to the aggregates of cells is considered as the bio-signature of interest. The second part presents the mathematical framework that describes the model of the proposed Mars geometrical Panspermia theory.

3.1 Underlying concept: Mars geometrical Panspermia theory

The Mars geometry Panspermia theory is of the perspective that the emergence of life was a multi-stage process. This multi-stage process ends in the aggregation of life forms leading to the emergence of first humans. In addition, the multi-stage process is considered a procedure in both lithopanspermia and radiopanspermia and other forms of life transfer mechanisms considered in the Panspermia perspective.

The current perspective being considered in the concept of Panspermia is to search for microorganisms such as Bacteria in locations in spatial objects such as comets and meteorites [25]. For example, Wickramansinghe et al. [25] point out evidence that bacteria similar to terrestrial bacteria can be found in the stratosphere and low earth orbit at the international space station. The discussion opines that more actions leading to the emergence of life besides that of bacteria take place in space. The set of actions in this context have a cognitive component and provide the first form of intelligence. The implied intelligence influences the multi-stage process during which the aggregation of life forms take place.

The intelligent pre-determination of the aggregation pattern of life-forms. This aggregation does not occur on earth but leaves a trace behind in the universe. These traces are considered by the proposed Mars geometry Panspermia theory to exist on Mars meteorites. The multi-stage process is considered to be intelligent. The invoking of an intelligent process does not contravene the principles of scientific reasoning and logic. In this case, the invoking of intelligence constitutes the hypothesis for the research being presented.

Given that intelligence is present as argued; such intelligence must have influenced the process and pattern of initial life-form aggregation. The initial aggregation pattern presents a base for the principles of evolution to act in the organism or life-form at a later epoch. A notion of such intelligence can be found in [26]. The consideration of the intelligence in this chapter is intended to make a contribution to the domain of general intelligence and space science research. General intelligence in this context includes biologically inspired artificial intelligence. The concept of the presence of intelligent design requires a test procedure to establish its existence. Such a procedure would help to validate the Panspermia theory.

3.2 Mathematical framework: Martian geometric Panspermia theory

The discussion here presents a mathematical model for describing the model of the universe as presented in the proposed Martian geometric Panspermia theory. The mathematical model considers the universe as comprising multiple locations, life conveying locations, life conveying material or mechanisms (or other life forms), life supporting locations, and life recording locations.

Life supporting locations are those locations where the conditions exist to support the presence of extra-terrestrial life. Let ς, ζ and $\ddot{Y}$ denote the set of (i) Life conveying locations, (ii) Life conveying mechanisms aided by micro-organisms and (iii) Life recording locations in the universe respectively.

Life conveying locations in this context refer to locations on Mars where meteorites to be ejected at a later epoch are located. Life conveying mechanisms describe the dynamics and processes ensuring the movement of ejected meteorites from Mars to earth. This is realizable while maintaining micro-organism composition in ejected meteorites. Life recording locations are those locations where the proof of the existence of extra-terrestrial life can be found.

$$\varsigma = \{\varsigma_1, \varsigma_2, \varsigma_3, ..., \varsigma_A\} \tag{1}$$

$$\zeta = \{\zeta_1, \zeta_2, \zeta_3, ..., \zeta_B\} \tag{2}$$

$$\ddot{Y} = \{\ddot{Y}_1, \ddot{Y}_2, \ddot{Y}_3, ..., \ddot{Y}_F\} \tag{3}$$

Life can be conveyed from location ς_a; $\varsigma_a \epsilon \varsigma$ to locations ς_{a+1}; $\varsigma_{a+1} \epsilon \varsigma$, ς_{a+4}; $\varsigma_{a+4} \epsilon \varsigma$ and ς_{a+7}; $\varsigma_{a+7} \epsilon \varsigma$ via life conveying material ζ_b; $\zeta_b \epsilon \zeta$ and ζ_{b+1}; $\zeta_{b+1} \epsilon \zeta$. For the purposes here, the locations ς_{a+1}, ς_{a+4} and ς_{a+7} ς_{a+2}; $\varsigma_{a+2} \epsilon \varsigma$, ς_{a+3}; $\varsigma_{a+3} \epsilon \varsigma$, ς_{a+5}; $\varsigma_{a+5} \epsilon \varsigma$ and ς_{a+6}; $\varsigma_{a+6} \epsilon \varsigma$ are life supporting locations. The location ς_a is called the root location.

The locations $\ddot{Y}_f$; $\ddot{Y}_f \epsilon \ddot{Y}$; $\ddot{Y}_{f+1}$; $\ddot{Y}_{f+1} \epsilon \ddot{Y}$; $\ddot{Y}_{f+2}$; $\ddot{Y}_{f+2} \epsilon \ddot{Y}$ act as life recording locations in the universe. They contain evidence of the action of life transfer process mechanisms by different micro-organisms. The action of life transfer by different micro-organisms is considered intelligent. Such a notion is supported by the evidence of intelligent behaviour in bacteria [27–29].

The notion that bacteria and microorganisms exhibit intelligent behaviour has received considerable interest [27–29]. The intelligent behaviour exhibited by microorganisms has been thought to evolve in response to surviving in their host environment. Intelligence requires the ability to act on information obtained from the environment. The capability to demonstrate intelligent behaviour implies that microorganisms can respond to environmental conditions from a base of stored information [27]. Therefore, it is feasible to think that microorganisms are capable of storing information.

It is inefficient for microorganisms to store all information relating to the processes in which they are engaged if all of such information is not required to develop survival strategies. An important piece of information that is considered not to be stored by the microorganism is those related to the pre-determination of geometrical forms of cell aggregation patterns. The storage of the information on the pre-determined geometrical forms is considered to increase micro-organism information overhead. Hence, it is not stored so that the microorganism can have high information storage and processing efficiency.

A scenario showing the relations between life recording locations, live conveying mechanisms and the earth is presented in **Figure 1**.
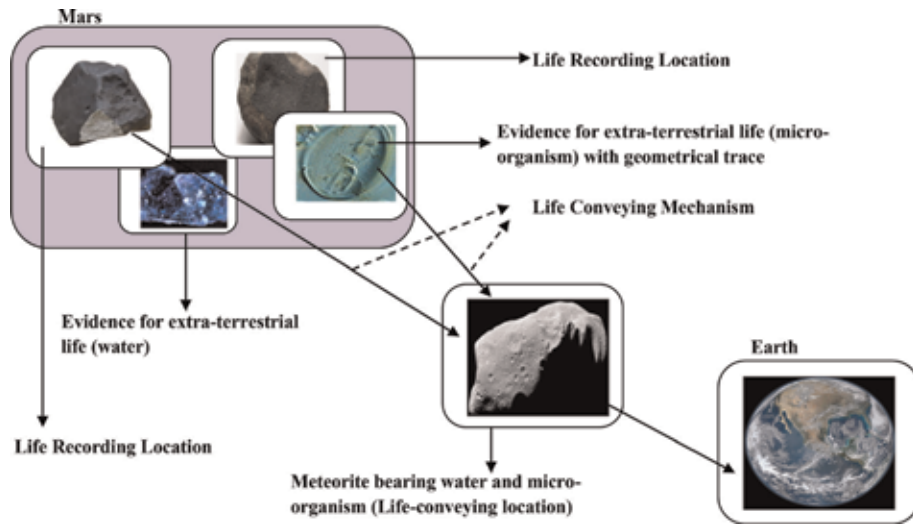
Figure 1.
Relations between life recording locations, life conveying mechanisms, Mars and earth as proposed in the Mars geometrical Panspermia theory.

4. Proposed Mars geometric Panspermia theory: verification

The Mars geometry Panspermia theory being proposed opines that geometric form pre-determination precedes the appearance of life-forms on earth. The geometric form pre-determination process is considered to leave behind traces in the planet Mars. The usage of the term pre-determination is intended to depict the execution of action(s) related to geometric form pre-determination at an epoch prior to the appearance of earthly life. The earlier epoch being implied here occurs on the planet Mars. The pre-determination process is considered to leave traces in Mars and specifically in Mars's meteorites. These traces are in the Mars's meteorites and can be discovered by the process of scanning Mars.

In the proposed Mars meteorite scanning, Mars's meteorites are considered to deliver the functionality of life conveying locations and that of the life recording locations. This is because Mars's meteorites have been found on the earth while other meteorites remain on the planet Mars. Meteorites from Mars have been found to have traces of life from Mars's environment as seen in [30].

Worth et al. in [31] opines that Mars's meteorites play an important role in lithopanspermia. They point out that some Martian meteorites have been suspected to have organic bio-markers. In [31], rock exchange between planets is theorized and considered to play an important role in inter-planetary life seeding and transfer. However, the discussion focuses on the rock (meteorite) transfer process as being responsible for the propagation of life throughout the universe. It does not consider the underlying process that has motivated the emergence of the different life forms that can be found on Mars's meteorites. This is because [31] have focused on the transfer mechanisms and details of the rock transfer process such as transfer rates.

Steffen et al. [32] share the same perspective with Worth et al. [31] and consider that life conveying biological material may have been exchanged between planets. The planets being considered exist in a multi-habitable system. Steffen et al. [32] recognise that the consideration of a multi-habitable system has implications on the propagation of life within the solar system and also outside the solar system. The

focus in [32] is on analysing the ejection mechanics and dynamics associated with exchanging life conveying biological material between planets.

The research focus on the Panspermia theory as seen in [31, 32] considers that life is propagated throughout the universe (within the solar system and outside the solar system). The focus has been on analysing the dynamics and investigating the relations between planets to enable life transfer to the earth. Mars has been widely considered as a planet from which life was seeded to the earth [10, 31–35]. The discussion in this chapter opines that the microbes and micro-organisms involved in the Panspermia life transfer process engage in different computational tasks. The execution of these computational tasks is considered feasible because earth based microorganisms such bacteria have been observed to engage in computational behaviour. This has led to the emergence of research in bacteria computing [36, 37].

In the discussion here, the Panspermia theory is considered to include the computational activities executed by microorganisms on meteorites sited in Mars. The evidence of such computation occurring on Martian meteorites is observed by Mars rovers and transmitted to the earth via a communication network.

Mars's meteorites play an important role in the Panspermia theory. They provide an environment enabling the interaction of microorganisms with astro-materials. Therefore, the meteorites can be considered as life recording locations. The ability of meteorites to move from Mars to earth motivates their consideration as life conveying locations. In the proposed Martian scanning, meteorites that are life recording locations are based on Mars. These meteorites are scanned within the Martian environment. The results from the scanning process are used to verify the proposed Martian geometric Panspermia theory.

In the proposed Mars geometric Panspermia theory, the geometry associated with life-form aggregation is considered to be determined via a native microorganism optimization computation procedure. The optimization procedure aims to determine the geometry of different life-form aggregations. The geometry being implied is described in the two dimensional and three dimensional representations of different life-forms. The dimension of the geometry being considered is in the range of nanometers to millimeters.

The Mars scanning procedure is executed using Mars rovers and Mars based transceivers. The Mars rover hosts data storage payload that hosts multi-spectral, multi-angular and high resolution images of different life-form aggregation.

In addition, the Mars rovers hosts payload that can detect geometry of life forms with pre-defined dimensions. In this case, the dimension lies in the range of nanometers to millimeters. The Mars based transceiver transmits the detected results (from the Mars exploration mission) to earth via a communication network. The communication network receives results from the Mars rovers via the Mars based transceivers and sends it to an earth station. The scanning procedure is executed in a distributed manner. The geometrical forms are obtained in two dimensional and three dimensional representations. The geometrical forms are transmitted to an earth station via a communication network. Each Mars rover is pre-loaded with geometrical forms of different life-form aggregations that can be found in earth based life forms.

Let θ_1 and θ_2 denote the set of geometrical forms on images in the Martian rover and geometry of aggregates of different life-forms in Mars's meteorite respectively. A match is considered to occur if $(\theta_1 \cap \theta_2) \neq \varnothing$. The verification of the proposed theory takes place in the following steps:

1. **Initial cell aggregation image generation**—This stage enables the generation of high resolution images of different aggregates of different life forms. The

process takes place on earth and allows the two dimensional and three dimensional representations of cell aggregates to be uploaded on the Mars's rovers intended for launch. The images obtained are stored and processed prior to being uploaded to the Mars's rover intended for launch from earth to Mars.

2. **High resolution image distribution**—This stage enables the generated two dimensional and three dimensional images to be uploaded on Mars's rovers intended for launch. The images to be uploaded to each Mars based rover will be influenced by the objectives of the Mars exploration mission. The exploration mission is focused on detecting geometrical patterns of aggregates of different life forms. The stage of high resolution image distribution is executed prior to the launch of rovers to Mars.

3. **Computational stage**—The computation requiring the execution of the image comparison takes place aboard the Mars based rover. The image comparison algorithm aims to verify if the condition $(\theta_1 \cap \theta_2) \neq \varnothing$ or $(\theta_1 \cap \theta_2) = \varnothing$ holds true. The proposed Mars geometric Panspermia theory is verified to hold true if $(\theta_1 \cap \theta_2) \neq \varnothing$. In this case, the Mars rover stores the outputs of the image compression procedure for the concerned Mars based meteorite and geometry of life form. The outputs of the image compression process are the (i) Binary comparison indicator, (ii) Mars's meteorite ID and (iii) Stored geometric form ID. The binary comparison indicator has a value of zero if $(\theta_1 \cap \theta_2) = \varnothing$ and a value of one if $(\theta_1 \cap \theta_2) \neq \varnothing$. The Mars's meteorite ID is the name that is commonly used to refer to Mars's meteorite. The geometric form ID is a numeric index that is assigned to a high resolution image being uploaded to the Mars rover.

4. **Computational algorithm update stage**—The computational algorithm update stage enables the image processing algorithm on the Mars based rover to be updated. This is necessary to continuously improve the result of the scanning process and prevent technology obsolescence. The update is executed by transmitting algorithms for improved image comparison and comparison results processing. The transmission that enables the execution of the update is received by the data storage payload which is connected to the Mars based transceiver. The Mars based transceiver receives the update information from communication satellites that receive the forwarded data from earth orbiting communication satellites which communicate with the earth station.

The relations between the stages of initial cell aggregation generation, high resolution image distribution, computational stage and computational algorithm update stage is shown in **Figure 2**. The scenario in **Figure 2** shows the process of executing the stages involved in the Mars geometrical search procedure. The cell aggregation generation procedure is executed on earth by acquiring high definition images of life-form aggregates in an earth based database. These high definition images are transferred from the database to the open source ground station entity. The open source ground station transmits the images and the geometrical outline information to the Mars based storage payload (with integrated transceiver). The images are transmitted from the storage payload with integrated transceiver to the Mars based rover via an upload process. The process scanning meteorites on Mars begins after uploading to the Mars based rover.

A bidirectional link exists between the Mars based rover and the storage payload with transceiver. The existence of the bidirectional link also enables the computational results from the Mars based rover to be sent to the storage payload with
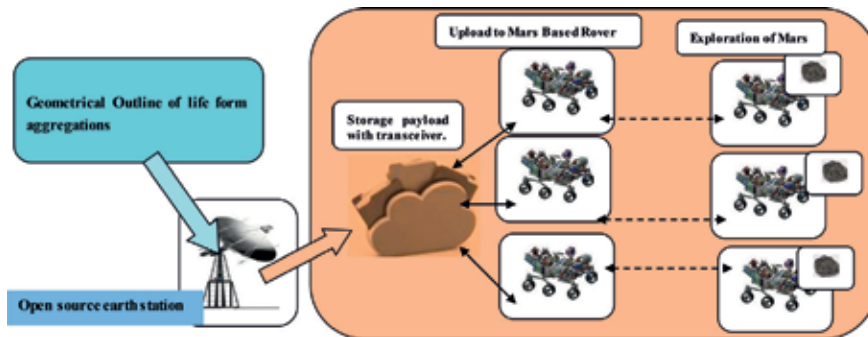
Figure 2.
Relations between the earth entities and the Martian entities in the proposed Martian geometrical search.

integrated transceiver. The existence of a bidirectional link between the storage payload with integrated transceiver and the open source earth station also allows the computational results to be accessible to the capital constrained space organization.

The computational algorithm used to execute the operation in $(\theta_1 \cap \theta_2)$ is an artificial neural network.

The artificial neural network is developed on the earth prior to launching the Mars based rover. It is trained with the high resolution images of different geometric forms for different cell aggregates, i.e., tissues and organs. This encodes the geometry of the high resolution images in the artificial neural network. The developed artificial neural network is installed on the data storage payload before launch. The artificial neural network is trained to receive geometrical forms from Mars meteorites as input. The predicted output of the artificial neural network is the value of the binary comparison indicator.

5. Network architecture

The successful execution of the computational procedure and transmission of computational result requires the availability of supporting network architecture. The design of network architecture should consider the preferences and resources available to the concerned space organization.

In this chapter, space organizations are considered in two categories. The first kind of space organization is that of a developed and technologically advanced nation. Examples of such space organizations are the National Aeronautics and Space Administration (NASA) and the European Space Agency (ESA). These space agencies have access to significant amount of resources to conduct interplanetary space missions. The first kind of space organization has resources to undertake Mars exploration missions aimed at verifying the proposed Mars geometrical Panspermia theory.

The second kind of space organization is that of a developing nation. Space organizations in this category do not have access to significant amount of resources required to conduct interplanetary space missions. However, this does not necessarily hold true for space agencies in the second category. The scarcity of resources in developing nations limits their ability to realize Mars communication networks. The network architecture being proposed is intended for use by space agencies in the second category.

The proposed network architecture comprises two entities. These are the ground based entity and the space based entity. In the proposed network, communications

is bidirectional. The downlink communications involves the transmission of information from Mars to earth. The uplink communication involves the transmission of information from earth to Mars.

The ground based entity comprises components such as earth stations, data processing and computing sub-entity (DPCE), communication payload re-configuration sub-entity (CPCE). The earth stations relay information to a Mars based data storage payload. The Mars based data storage payload hosts updated information on high definition two dimensional and three dimensional images of life-form aggregates. The high definition images show the geometry of the concerned life-form aggregates. The Mars based data storage payload receives information from a Mars orbiter.

The DPCE is a ground based entity owned by the space organization in a developing country. It aggregates the high resolution images of cell aggregates from different sources. In addition, it hosts the high resolution images of cell-aggregates. The content of the DPCE is dependent on the science mission of Mars exploration. In the case where geometrical forms of humans are being sought, the DPCE's contents are high resolution images of cell aggregates of humans. The DPCE's contents are transferred to the Mars based data storage payload via a network of ground stations or communication satellites.

The CPCE enables the configuration of the communication payload that links the DPCE to the Mars based data storage payload. It co-ordinates and monitors the process of data transfer between the Mars based data storage payload, Martian rovers and the DPCE. The DPCE communicates with the Mars based data storage payload via open source ground stations.

The use of open source ground stations is suitable for capital constrained space organizations in developing countries. In the proposed model, space organization seeking to execute Mars exploration missions can make use of open source ground stations with expansive global coverage. This approach is feasible due to the development of open source software [38] and open source hardware [39–41].

However, the use of open source hardware and software approach has not been widely considered in developing components for Martian missions in developing nations. The use of open source paradigm is beginning to gain recognition for space exploration and satellite applications. Examples of open source initiatives for developing satellites are Kubos [42], NASA Virtual ADAPT [43, 44], and the open satellite project [45]. The examples in [42–45] have focused on development of open source satellite software. In this regard, space exploration and technology has adopted the open source software development approach. The open source approach has also been considered for developing satellite hardware. The UPSat initiative is an example of a case where open source approach has been used for satellite hardware development [46, 47]. This initiative is sponsored by the Libre space foundation [48]. The Libre space foundation aims to create open source space technologies for future space applications. The organization is also playing a leading role in the development of open source satellite earth stations in its satellite networked open ground station (SATNOGs) initiative. The SATNOGs initiative intends to make the development of the ground and space segments of a satellite network open to the public. It comprises crowdsourced satellites whose information is held in a database [49].

The space organization with insufficient capital and in a developing country can access the type of database in [48] to determine if it can communicate with a Mars based transceiver. The output of this procedure is a ground station or multiple ground stations that can be used to communicate with the Mars based transceiver. This communication can be used to realize Mars rover data sharing between technologically advanced and non-technologically advanced nations.
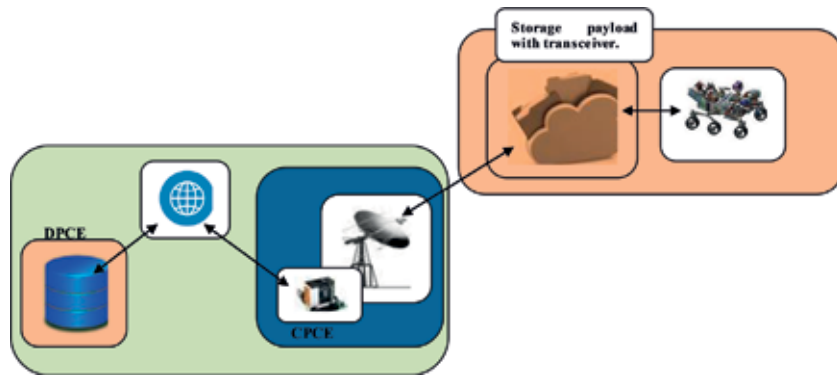
Figure 3.
Relations between earth based and Mars based entities involved in the Martian geometrical search paradigm.

The network architecture showing the role of the DPCE, CPCE and Martian based transceivers is shown in **Figure 3**. The scenario in **Figure 3** shows the case where a capital constrained space organization with one DPCE having access to one earth station from the open source ground station network.

In the network architecture shown in **Figure 3**, the DPCE communicates with the CPCE (an SDR) via an internet call. The internet call enables the transfer of images and geometrical forms from the DPCE to the CPCE. The CPCE has reconfigurable and temporal data storage capability. The CPCE enables the earth station to transmit the data to the Mars based storage payload with integrated transceiver.

The network architecture can be implemented by a single nation or either multiple nations. The concerned nations are those with capital constrained space organizations. The use of open source ground stations for a given time to transmit data to Mars. The capital constrained space organizations make use of the open source ground station antenna for a given time. The scenario presented in **Figure 3** assumes that the capital constrained space organization is able to afford the design, production and launch of the Martian rovers.

However, the costs of designing and launching a rover to Mars can easily approach tens of billions of dollars thereby overwhelming the economic capability of developing countries. For example, the cost of developing Curiosity approaches USD 2.5 billion. The cost of launching multiple rovers increases beyond the financial capability of developing nations. Nevertheless, capital constrained space organizations need to be able to investigate the Martian geometrical Panspermia theory.

The discussion here proposes the concept of Martian rover data sharing. In Martian rover data sharing, the data obtained by a Martian rover owned by a technologically advanced nation is shared with capital constrained space organization. The sharing is done without disrupting the scientific objective of the technologically advanced nation. The sharing is unaffected by power limitations because the concerned Mars rover is nuclear powered.

6. Conclusion

The discussion in this chapter presents a new perspective in investigating human origins. The new perspective is called the Mars geometry Panspermia theory. However, the new perspective opines that the emergence of human life was preceded by pre-determining the geometry of different life forms aggregate. The evidence for

this intelligent task exists as a geometrical record on Mars's meteorites. The chapter also proposes a low cost network architecture that aims to verify the Mars geometry Panspermia theory. The proposed architecture searches Mars's meteorites for geometric patterns of different life-forms aggregations. It also incorporates Mars rover data sharing enabling space organizations in developing nations to access the acquired data and also investigate the Mars geometrical Panspermia theory.

Author details

Ayodele Abiola Periola
Department of Electrical, Electronics and Computer Engineering, Bells University of Technology, Nigeria

*Address all correspondence to: periola@hotmail.com

IntechOpen

References

[1] Kragh H. Cosmology and the origin of the universe: Historical and conceptual perspectives [Online]. 2017. Available from: https://arxiv.org/ftp/arxiv/papers/1706/1706.00726.pdf [Accessed: 05 February 2019]

[2] Elizalde E. "All that matter ... in one Big Bang ...," & other cosmological singularities [Online]. 2018. Available from: https://arxiv.org/pdf/1801.09550.pdf [Accessed: 05 February 2019]

[3] Schlaufman KC, Thompson IB, Casey AR. An ultra metal-poor star near the hydrogen-burning limit. The Astrophysical Journal. Nov 10, 2018;**867**(98):1-14

[4] Omar A, Kumar B, Gopinathan M, Sagar R. Scientific capabilities and advantages of the 3.6 meter optical telescope at Devasthal, Uttarakhand. Current Science. 2017;**113**(4):682-685

[5] Wang Z, Wang N, Li Z, Xiao F, Dai J. Human high intelligence is involved in spectral redshift of biophotonic activities in the brain. Proceedings of the National Academy of Sciences. 2016;**113**(31):8753-8758

[6] Rahnama M, Bokkon I, Tuszynski J, Cifra M, Sardar P, Salari V. Emission of biophotons and neural activity of the brain. Available from: https://arxiv.org/vc/arxiv/papers/1012/1012.3371v1.pdf [Accessed: 05 February 2019.

[7] Zarkeshian P, Kumar S, Tuszynski J, Barclay P, Simon C. Are there optical communication channels in the brain? [Online]. 2017. Available from: https://arxiv.org/pdf/1708.08887.pdf arXiv:1708.08887v1 [physics.bio-ph]

[8] Steele EJ, Gorczynski RM, Tokoro G, Wickramaninghe DT, Wickramansinghe NC. Hoyle-Wickramasinghe Panspermia is far more than a hypothesis features of

mature cell biology in astrophysical phenomena [Online]. Nov 25, 2018. Available from: http://viXra.org/abs/1811.0221, http://vixra.org/pdf/1811.0221v2.pdf [Accessed: 05 February 2019]

[9] Williams M. The Milky Way could be spreading life from star to star. Oct 15, 2018. Available form: https://phys.org/news/2018-10-milky-life-star.html

[10] Lingam M, Loeb A. Enhanced interplanetary Panspermia in the TRAPPIST-1 system. Proceedings of the National Academy of Sciences. 2017;**114**(26):6689-6693

[11] Georgiev D. The phylum Tardigrada and the Panspermia theory? Can the Tardigrades be live capsules carrying a variety of DNA sequences inside as food particles, endosymbiotic organisms and parasites? International Journal of Pure and Applied Zoology. 2016;**4**(4):292-293

[12] Giulio M. Biological evidence against the Panspermia theory. Journal of Theoretical Biology. 2010;**266**(4):569-572

[13] Mustard JF. Why Mars remains a compelling target for planetary exploration. Sep 15, 2009. Available from: https://mepag.jpl.nasa.gov/reports/decadal/JohnFMustarda.pdf [Accessed: 15 Sep 2009]

[14] Johnson JR, Hoehler T, Westall F, Withers P, Plescia J, Hamilton V, et al. Summary of the Mars science goals, objectives, investigations, and priorities—MEPAG science goals, objectives, investigations, and priorities: 2009. 2009

[15] Johnson JR. Report to planetary science advisory committee. Feb 23, 2018. Available from: https://smd-prod.s3.amazonaws.com/science-red/

s3fs-public/atoms/files/0-AGs-MEPAG%20Report%20to%20PAC%2002-2018_v02%3DTAGGED.pdf [Accessed: 23 February 2018]

[16] Outer Planet Assessment Group. Findings of the Outer Planets Assessment Group (OPAG) from the meeting in Atlanta, hosted by Georgia Tech, on February 22-23, 2017. [Online]. Feb 22-23, 2017. Available from: https://www.lpi.usra.edu/opag/meetings/feb2017/findings.pdf

[17] International MSR Objectives and Samples Team (iMOST), Beaty DW, Grady MM, MCSween HY, Sefton-Nash E, Carrier BL, et al. The potential science and engineering value of samples delivered to earth by Mars sample return. Meteoritics & Planetary Science. 2019;**54**(3):667-671

[18] Rummel JD, Beaty DW, Jones MA, Bakermans C, Barlow NG, Boston PJ, et al. A new analysis of Mars "special regions": Findings of the second MEPAG special regions science analysis group (SR-SAG2). Astrobiology. 2014;**14**(11):887-968

[19] Cabriol NA. The coevolution of life and environment on Mars: An ecosystem perspective on the robotic exploration of biosignatures. Astrobiology. 2018;**18**(1)

[20] Hays LE, Graham HV, Des Marais DJ, Hausrath EM, Horgan B, McCollom TM, et al. Biosignature preservation and detection in Mars analog environments. Astrobiology. 2017;**17**(4):363-400

[21] Belz A, Cutts J, Barengoltz J, Beaty D, Beauchamp P, Buxbaum K, et al. Planetary Protection and Contamination Control Technologies for Future Space Science Missions. NASA Jet Propulsion Laboratory, Solar System Exploration Directorate, JPL D—31974. 2005. Technical Report, Original Issue June 2005, pp. 1-76

[22] Woo M. Better sequencing tech may help keep planets clean. Proceedings of the National Academy of Sciences of the United States of America. 2018;**115**(11):2542-2544

[23] Periola AA, Falowo OE. Intelligent cognitive radio models for enhancing future radio astronomy observations. Advances in Astronomy, Hindawi. 2016;**2016**:1-15. Article ID 5408403. DOI: 10.1155/2016/5408403

[24] Periola AA, Falowo OE. Interference protection of radio astronomy services using cognitive radio spectrum sharing models. In: European Conference on Networks and Communications; Paris, France. 2015. pp. 86-90

[25] Wickramansinghe NC, Wickramaninghe DT, Steele EJ. Comets, Enceladus and Panspermia. Astrophysics and Space Science. 2018;**363**(244):1-7

[26] Korthof G, Fred Hoyle's The Intelligent Universe—A summary & review. Available from: http://wasdarwinwrong.com/kortho47.html. March 5, 2006

[27] Westerhoff HV, Brooks AN, Simeonidis E, Contreras RG, He F, Boogerd FC, et al. Macromolecular networks and intelligence in microorganisms. Frontiers in Microbiology. 2014;**5**:1-17. Article 379

[28] Majumdar S, Pal S. Information transmission in microbial and fungal communication: From classical to quantum. Journal of Cell Communication and Signaling. 2018;**12**:491-502

[29] Lyon P. The cognitive cell: Bacterial behavior reconsidered. Frontiers in Microbiology. 2015;**6**:1-18. Article 264

[30] Tait AW, Gagen EJ, Wilson SA, Tomkins AG, Southam G. Microbial

populations of stony meteorites: Substrate controls on first colonizers. Frontiers in Microbiology. 2017;**8**:1-14. Article 1227

[31] Worth RJ, Sigurdsson S, House CH. Seeding life on the moons of the outer planets via lithopanspermia. Astrobiology. 2013;**13**(12):1155-1165

[32] Steffen JH, Li G. Dynamical considerations for life in multi habitable planetary systems. The Astrophysical Journal. 2016;**816**(2):1-10

[33] Veras D, Armstrong DJ, Blake JA, Marcos JFG, Jackson AP, Schaeffer H. Dynamical and biological Panspermia constraints within multi-planet exosystems. Astrobiology. 2018;**18**(9): 1-17. DOI: 10.1089/ast.2017.1786

[34] Wickramasinghe C. Astrobiology and Panspermia—Life from space. February 2009 © 2009 The Biochemical Society. 2009; pp. 40-44

[35] Nicholson WL. Ancient micronauts: Interplanetary transport of microbes by cosmic impacts. Trends in Microbiology. 2009;**17**(6):243-250

[36] Waltz E. Biocomputer and memory built inside living bacteria. IEEE Spectrum. 2017. Available from: https://spectrum.ieee.org/biomedical/devices/biocomputer-and-memory-built-inside-living-bacteria

[37] Kendon V, Sebald A, Stepney S. Heterotic computing: Exploiting hybrid computational devices. Philosophical Transactions A. 2015; **373**(2046):1-6

[38] Wilson ML, Tchantchaleishvili V. The importance of free and open source software and open standards in modern scientific publishing. Publication. 2013; **1**:49-55. DOI: 10.3390/publications1020049

[39] Open Compute Project. Contributions. Available from: https://www.opencompute.org/contributions

[40] Microsoft Azure. Hardware Innovation for the Cloud-Reimagining hyperscale, open-source hardware development that is shared across the industry. Available from: https://azure.microsoft.com/en-in/global-infrastructure/hardware-innovation/. 2019

[41] Sofar. Ocean Sensors and Drones Made Easy. Available from: https://www.sofarocean.com/

[42] Kubos. An Open source platform for satellites. Available from: https://github.com/kubos/kubos. 2019

[43] NASA. Virtual Adapt. Available from: https://github.com/nasa/VirtualADAPT. 2019

[44] Duley J. NASA. code.nasa.gov. Available from: https://code.nasa.gov/

[45] Opensatellite. Opensatellite.github.io. Available from: https://github.com/opensatellite. 2009

[46] UPSat. The first open source satellite : A QB50 cubesat by Libre Space Foundation & University of Patras. Available from: https://upsat.gr. 2016

[47] Github. Libre Space Foundation. Available from: https://github.com/librespacefoundation. 2019

[48] Libre Space Foundation. Claim Space, the Libre Way: Free and Accessible Space for all Creating Open Source space technologies. Available from: https://libre.space/

[49] SatNOGS. SatNOGS-Open Source global network of satellite ground-stations. Available from: https://satnogs.org/

Edited by Bryan Palaszewski

Over the last 80 years, dreamers, engineers, mission planners, and scientists have sought, defined, and created many methods of exploring the solar system. Robotic missions to nearly every type of solar system object have been conducted. The data from these missions has opened new vistas on the riches of the planets and the asteroids. Water and other materials that can help humans survive in space have been found in abundance. Human lunar missions have returned with hundreds of kilograms of rocky and dusty samples. These samples (regolith) has given us hope that humanity will one day colonize the Moon, Mars, and the moons of other planets. Many space agencies around the world have shared their information and created collaborations for the betterment of all. Interplanetary dreams are part of humanity's future, those dreams will create a future where humanity can begin to flourish throughout the planets. This book is a celebration of those dreams.

IntechOpen